# Dynamics of Nanoparticles in Complex Media

A Dissertation

Presented to

the Faculty of the Department of Chemical and Biomolecular Engineering

University of Houston

In Partial Fulfillment

of the Requirements for the Degree

Doctor of Philosophy

in Chemical Engineering

by

Firoozeh Babayekhorasani

December 2015

**Dynamics of Nanoparticles in Complex Media**

_____
Firoozeh Babayekhorasani

Approved:

_____
Chair of the Committee
Jacinta C. Conrad, Assistant Professor,
Chemical and Biomolecular Engineering

_____
Chair of the Committee
Ramanan Krishnamoorti, Professor,
Chemical and Biomolecular Engineering

Committee Members:

_____
Peter Vekilov, Professor,
Chemical and Biomolecular Engineering

_____
Megan Robertson, Assistant Professor,
Chemical and Biomolecular Engineering

_____
Ralph Metcalfe, Professor,
Mechanical Engineering

_____
Kalyana Babu Nakshatrala, Assistant Professor,
Civil and Environmental Engineering

_____
Suresh K. Khator, Associate Dean,
Cullen College of Engineering

_____
Michael P. Harold, Professor and Chair,
Chemical and Biomolecular Engineering

## Acknowledgements

First and foremost I would like to thank God for all the things he has given me and for bringing me to this point in my life. Next, I want to acknowledge my lovely parents, Mostafa and Fatemeh, and my siblings, Fereshteh, Alireza, and Mahdi for all the support they have given me. I deeply appreciate my husband, Dr. Meead Saberi, for his infinite love, encouragement, and support.

I am greatly thankful to my advisors and mentors Drs. Jacinta Conrad and Ramanan Krishnamooriti whom their invaluable advice, support, and encouragement made this work possible. I am also grateful to Dr. David Dunstan for his support while I was continuing my work at University of Melbourne. I would also like to thank Drs. Peter Vekilov, Megan Robertson, Ralph Metcalfe, Kalyana Babu Nakshatrala for reviewing my dissertation and serving in my committee.

I am full of gratitude to the supporting staff of the Department of Chemical and Bimolecular Engineering at University of Houston who have always been there for me. Thanks to Nicolette Solano, My-Dung Lieu, Patricia Cooks, Yolanda Thomas, and Pamela Moses.

Finally, I would like to thank all my friends and my lab fellows who have helped me in so many ways in my intercontinental PhD journey both at University of Houston and University of Melbourne. Without their support, I would not be able to finish this work. Thank you, Tayebeh, Hossein, Aida, Maryam, Hengameh, Farshid, Sara, Arian, Saeed, Mohammad, Yasser, Nell, Butch, Sally, Zahra, Laleh, Amin, Hosna, Elham, Haleh, Kai, Sumedha, Kim, Brian, Rahul, Jinsu, Andrea, Ryan, and Nayoung.

# Dynamics of Nanoparticles in Complex Media

An Abstract
of a
Dissertation
Presented to
the Faculty of the Department of Chemical and Biomolecular Engineering
University of Houston

In Partial Fulfillment
of the Requirements for the Degree
Doctor of Philosophy
in Chemical Engineering

by
Firoozeh Babayekhorasani
December 2015

## Abstract

Hindered mobility of nanoparticles in complex media is ubiquitous in drug delivery, in processing of polymer nanocomposites, and in extraction of hydrocarbons. These applications require nanoparticles suspended in non-Newtonian fluids to be controllably dispersed through complex porous media. In this dissertation, the role of non-Newtonian fluid characteristics on mobility of nanoparticles through complex media is studied.

First, the diffusive mobility of nanoparticles in solutions of a high-molecular weight polyelectrolyte, partially hydrolyzed polyacrylamide, is measured to determine the role of polymer concentration on the local dynamics of nanoparticles. Above the polymer overlap concentration, nanoparticle mobility exhibits subdiffusive behavior at short time scales. The dynamics approach Fickian diffusion at longer time scales and at all concentrations but deviate from predictions made from the bulk viscosity of the polymer solutions. These results indicate that particle dynamics are coupled to the polymer dynamics and highlight the importance of segmental motion of polymer chains on the long-time diffusivity of nanoparticles whose size is comparable to typical polymer length scales.

Second, the diffusive mobility of nanoparticles suspended in Newtonian and non-Newtonian solutions within porous media is studied to separate the effects of confinement mediated by macromolecules and by geometric obstacles on diffusion of nanoparticles. Diffusive mobility decreases as nanoparticles are increasingly hindered by spatial confinement due to hydrodynamic interactions with the porous medium. In non-

Newtonian solutions, temporary adsorption of particles onto the surface of glass beads due to depletion interactions further reduces the diffusive mobility of particles.

Finally, the effects of flow properties, fluid characteristics, and geometric confinement on dispersion of particles through mono and bidisperse porous media are studied. The long-time dispersion coefficients of nanoparticles in longitudinal and transverse direction scale linearly with Pe number across a range of solution flow rates and pore sizes, independent of the fluid rheology. This suggests that random mixing effectively averages out the velocity fluctuations so that the non-Newtonian fluid characteristics do not affect long-time dispersion. Moreover, average transport properties do not depend on distribution of pore size within the beds. Overall, this dissertation improves our essential understanding of hindering factors affecting dynamics of nanoparticles through complex media.

## Table of Contents

## List of Figures

## List of Tables

# Chapter 1

# 1.0 Introduction

## 1.1 Nanoparticle applications

Drug delivery, exploration and production of hydrocarbons, groundwater treatment, and nanocomposite processing are among the many applications involving transport of nanoparticles through random and heterogeneous porous media. Achieving maximum efficacy in these applications requires effective transport of nanoparticles suspended in non-Newtonian fluids through complex geometrically-structured media.

### 1.1.1 Cancer treatment and drug delivery

In drug delivery, Nanoparticles recognize distinct features of cancerous cell to selectively target these cells. The structure of cancerous cells is very disorganized, porous, and heterogeneous because of high growth factor of such cells.[1] Such abnormal structures, which is known as enhanced permeability and retention effect,[2–4] enables nanoparticles to permeate through large porous structure of tumors. Moreover, the fast growing feature of tumor cells requires that the cells uptake glucose to provide more energy, which decreases the pH of surrounding environment of the cells compared to normal cells. Targeted nanoparticles are designed to release chemotherapeutic agents in the acidic environment characteristic of tumors but not in physiological pH of the normal cells.[5–7] In contrast, conventional chemotherapy in cancer treatment is not targeted,

causing toxic effects on normal cells and reducing the effectiveness of the drugs on cancer cells.[8,9] These deleterious outcomes can be avoided by targeted drug delivery, in which nanoparticles are designed to effectively transport to selected tumor cells by tuning their size and surface chemistry. By tuning these properties, nanoparticles are able to circulate through the blood stream to reach and kill the cancerous cells without having harmful effects on normal cells.

### 1.1.2 Exploration and extraction of hydrocarbons

Nanoparticles can also be employed in exploration of new hydrocarbon reservoirs and in enhancing oil recovery from existing sources. Magnetic nanoparticles have been tested along with sweep or fracture fluids to improve the detection of hydrocarbon sources using external electromagnetic field.[10,11] Nanoparticles can also be applied to enhance oil recovery by improving the displacement of the oil with water by, for example, changing the wettability of the rock surface from oil-wet to water-wet,[12,13] reducing the surface tension of the rock surfaces, tuning the viscosity of the injected fluids,[12] or enhancing the density profile layering.[14,15] The effectiveness of applying nanoparticles in oil fields depends on their ability to remain dispersed in injected fluid, to travel a long distance to targeted locations, and to selectively attach to the desired positions within the reservoir.[16]

### 1.1.3 Groundwater and wastewater treatments

Groundwater and wastewater treatment is another important area in which nanoparticles can be beneficially applied to remove both organic and inorganic contaminants. The use of nano and microscale zero-valent iron particles, for example, leads to improvements in eliminating organic contaminants or in immobilizing hazardous ion metals in aqueous slurries.[17–20] The advantages of nanoscale particles in these applications arise from their small size: compared to millimeter-scale particles, nanoscale particles are more readily transported through porous structure and moreover react more rapidly with organic compounds because of their higher surface area. However, the lifetime of the nanoparticles is short as their reaction rate is high. Another challenge of using nano and micron size particles is to maintain their stability and prevent them from aggregation which affect their mobility through deep porous media.[19,21,22] understanding the effect of interactions of particles with complex fluid constituents and with nearby surfaces will help to improve transport of particle through such media.

### 1.1.4 Nanocomposites

Nanocomposites consist of nanoparticles that are added to a polymer matrix. Dispersed nanoparticles in the polymer matrix can improve mechanical, electrical, optical, and thermal properties of the nanocomposites.[23,24] Several types of nanoparticles can be used in the structure of nanocomposites, including nanospheres, nanorods, nanotubes, and nanosheets.[25] These different types of nanoparticles have distinct physical properties compared to microscale particles.[26] Moreover, they exhibit much larger

interfacial interactions with the host polymer because of their higher surface area.[27,28] Size,[23] shape, and spatial dispersion[25,28] of nanoparticles within the polymer matrix can significantly influence the physical properties of nanocomposites. Attaining the desired physical properties requires controlling the spatial location of the particles, which in turn is a challenge in flow-based processing routes.

## 1.2 Diffusive dynamics of nanoparticles in complex media

Mobility characteristics in crowded environments or confined media depend on spatial and dynamical heterogeneities within the environment.[29] Spatial structure, void accessibility, and connectivity of the confined media influence the diffusional behavior in such media.[29–31] For instance, diffusion of particles in large colloidal suspensions[32,33] and in entangled or unentangled matrices[34–40] is confined by rigid, semi-flexible, or flexible dynamical networks. The diffusional dynamics of particles that are hindered by these networks slow down and may become coupled with dynamics of surrounding media. Mobility of particles also depends on the relative size of the particles to the length scales of the void space.

Mobility is also confined in diffusion of nanoparticles in ordered[41–43] or disordered[44–46] porous media or diffusion of polymer chains close to the surface.[47–49] Studies on diffusion of nanoparticles in ordered porous media show that diffusional dynamics damp as the particles become more confined while remaining Fickian. Distribution of particle displacements, however, becomes non-Gaussian representing heterogeneities of the environment.

Diffusive mobility of nanoparticles can be measured using the ensemble-averaged mean squared displacement (MSD), given by $MSD = \langle (x_i(t+\Delta t) - x_i(t))^2 \rangle$, where $x_i(t)$ and $x_i(t+\Delta t)$ are the projection of the particle position along the $x$-axis at times $t$ and $t+\Delta t$, respectively.[50,51] The time dependence of the MSD can be used to distinguish normal from anomalous diffusion.[52] In Brownian or Fickian diffusion, the MSD grows linearly with the lag time Δt, i.e. $\langle \Delta x^2 \rangle = 2D\Delta t$, where D is the diffusion coefficient of the nanoparticles. By contrast, in anomalous diffusion the MSD grows nonlinearly with time, $\langle \Delta x^2 \rangle = 2D_\gamma \Delta t^\alpha / \Gamma(1+\gamma)$, where Γ(x) is the Gamma function. The exponent $\alpha$ satisfies $0 < \alpha < 1$ in the anomalous subdiffusive regime and $\alpha > 1$ in the anomalous superdiffusive regime.[51–54]

Anomalous subdiffusive behavior appears frequently in the context of macromolecules or particles moving in complex crowded environments.[55] Examples of anomalous diffusion include diffusion of nanoparticles in concentrated and entangled polymer solutions and polymer melts,[56] cell migration,[57] and proteins in cellular environments.[58] Subdiffusive behavior in crowded environments originates from interaction between the particles and obstacles, which interrupts the diffusive motion of particles.[55,59] Diffusion of nanoparticles in polymer solutions and melts has been widely investigated theoretically[34,36,60–65] and experimentally[66–72] for dilute to concentrated polymer solutions and for a wide range of relative particle size to polymer length scales. Considering hydrodynamic interactions between particles and polymer molecules,[60,73] models predict a stretched exponential dependence of microscopic diffusion coefficient on polymer concentration $D/D_0 = \exp(-\beta c^\nu)$.[67,69,70,74] In dilute polymer solutions;

polymer chains are assumed as hard spheres, when they smaller than particles. The hydrodynamics interaction between such hard spheres and particles controls diffusion of nanoparticles. In semi-dilute solution, at a length scale of polymer correlation length, hydrodynamic interactions are screened. The polymer mesh size or correlation length is a function of polymer concentration and for a good solvent is given by $\xi = R_g \left(\frac{\phi}{\phi*}\right)^{-0.76}$.[72] hydrodynamics models do not consider effect polymer relaxation times on particle dynamics. In a recently-developed scaling theory,[34] particle mobility in an entangled polymer solution depends on the relaxation time scales of polymer chains. The terminal diffusivity scales as a power law with particle size and polymer concentration. From this theory three distinct regimes are defined:

i. *Small particles* ($d < \xi$): the polymer matrix does not influence the mobility of particles. In this regime the diffusion coefficient of particles is determined by solvent viscosity using the Stokes-Einstein relation. The MSD is linearly proportional to time, which indicates Fickian motion, i.e. $\langle \Delta r^2(t) \rangle \simeq D_s t$ for $t > \tau_0$ and $D_s \simeq K_B T/(\eta_s d)$, where $K_B$ is the Boltzmann constant, $T$ is the absolute temperature, $\eta_s$ is the viscosity of the neat solvent and $\tau_0$ is the relaxation time of monomers in polymer chain.

ii. *Intermediate* particles ($\xi < d < a$): At short time scales $t < \tau_\xi$, the particle motion is diffusive and depends on solvent viscosity, where $\tau_\xi$ is the relaxation time of polymer chains with dimension $\xi$. At intermediate time scales $\tau_\xi < t < \tau_d$, fluctuations of the polymer chains affect the mobility of particles, where $\tau_d$ is the

relaxation time of polymer segment with the same size of particle; the particle motion is subdiffusive with the MSD growing sub-linearly with time. The diffusion coefficient of particles depends on effective polymer viscosity, which is the viscosity of the polymer sections with chain size of $\xi(t/\tau_\xi)^{1/4}$, $\eta_{\text{eff}}(t) \simeq \eta_s(t/\tau_\xi)^{1/2}$ and $D_{\text{eff}}(t) \simeq k_B T/(\eta_{\text{eff}}(t)d) \simeq D_s(t/\tau_\xi)^{-1/2}$. At long time scales t > $\tau_d$, the mobility of particles becomes diffusion again for time scale greater than $\tau_d$, when the subsection size of polymer chains is of the order of particle size, $\tau_d \simeq \tau_\xi(d/\xi)^4$, $\langle\Delta r^2(\text{t})\rangle \simeq D_t t$, and $D_t \simeq k_B T/(\eta_{\text{eff}}(\tau_d)d) \simeq k_B T\xi^2/(\eta_s d^3)$.

iii. *Large particles* (d > a): the motion of large particles, which are caged by entanglements, depends on the relaxation time of the entanglements. At short time scales, t < $\tau_e$, particle motion is similar to that of intermediate particles in the first two regimes, where $\tau_e \simeq \tau_\xi(d/\xi)^4$. The MSD depends on three length scales: polymer tube diameter *a*, polymer correlation length ξ, and particle diameter *d*, $\langle\Delta r^2(\text{t})\rangle \simeq a^2\xi/d$. At intermediate time scales $\tau_e$ < t < $\tau_{\text{rep}}$, entanglement strands of polymer chain form transient cages that trap the particles up to the reptation time ($\tau_{\text{rep}}$), so the mean square displacement is constant on these time scales $\langle\Delta r^2(\text{t})\rangle \simeq a^2\xi/d$. At time scales longer than reptation time t > $\tau_{\text{rep}}$, particle returns to diffusive motion and the MSD is linearly proportional to time. Diffusion coefficient depends on the bulk viscosity via Stokes-Einstein relation, $\langle\Delta r^2(\text{t})\rangle_{\text{rep}} \simeq k_B T/(\eta d)\, t \simeq (\frac{a^2\xi}{d})\, t/\tau_{\text{rep}}$, $D_{\text{rep}} \simeq k_B T/(\eta d) \simeq a^2\xi/(d\tau_{\text{rep}})$.

Further insight into the origin of dynamics of nanoparticles in complex media has been obtained from the distributions of particle displacements over time,[33,38,39,75–82] also known as the van Hove correlation function, $G_s(x, \Delta t) = 1/N\langle\sum_{i=1}^{N}\delta(x - |x_i(t) - x_i(0)|)\rangle$. Here $\langle\cdot\rangle$ is an ensemble average over N particles and $\delta(\cdot)$ is the Dirac delta function.[83] For particles diffusing in a viscous liquid, the distribution of displacements at all lag times is well-described by a Gaussian distribution ($G_s(x, \Delta t) \propto \exp\left(-\left(\frac{x}{2Dt}\right)^2\right)$). In dense hard sphere colloidal suspensions[75–79,82] and supercooled liquids[80,81] the distribution of displacements is non-Gaussian, indicating dynamical heterogeneity and cooperative dynamics in distinct populations of slow and fast particles.

## 1.3 Transport of nanoparticles through porous media

Natural porous media (Figure 1.1) often have disordered structure. Mobility of nanoparticles in disordered porous materials includes additional complexities arising from non-uniform and heterogeneous pore geometries.[43,46] Transport properties of particles depend on microstructure of the pores and are particularly important in chemical reactions in biological cells and in heterogeneous catalysis. In these systems, pore-scale geometries and accessibility of the void spaces are the critical parameters to control the kinetics of the reactions.[84,85] Understanding the pore-scale mechanisms controlling transport of the reactants enables these reactions to be specially controlled and tuned to achieved the desired products.

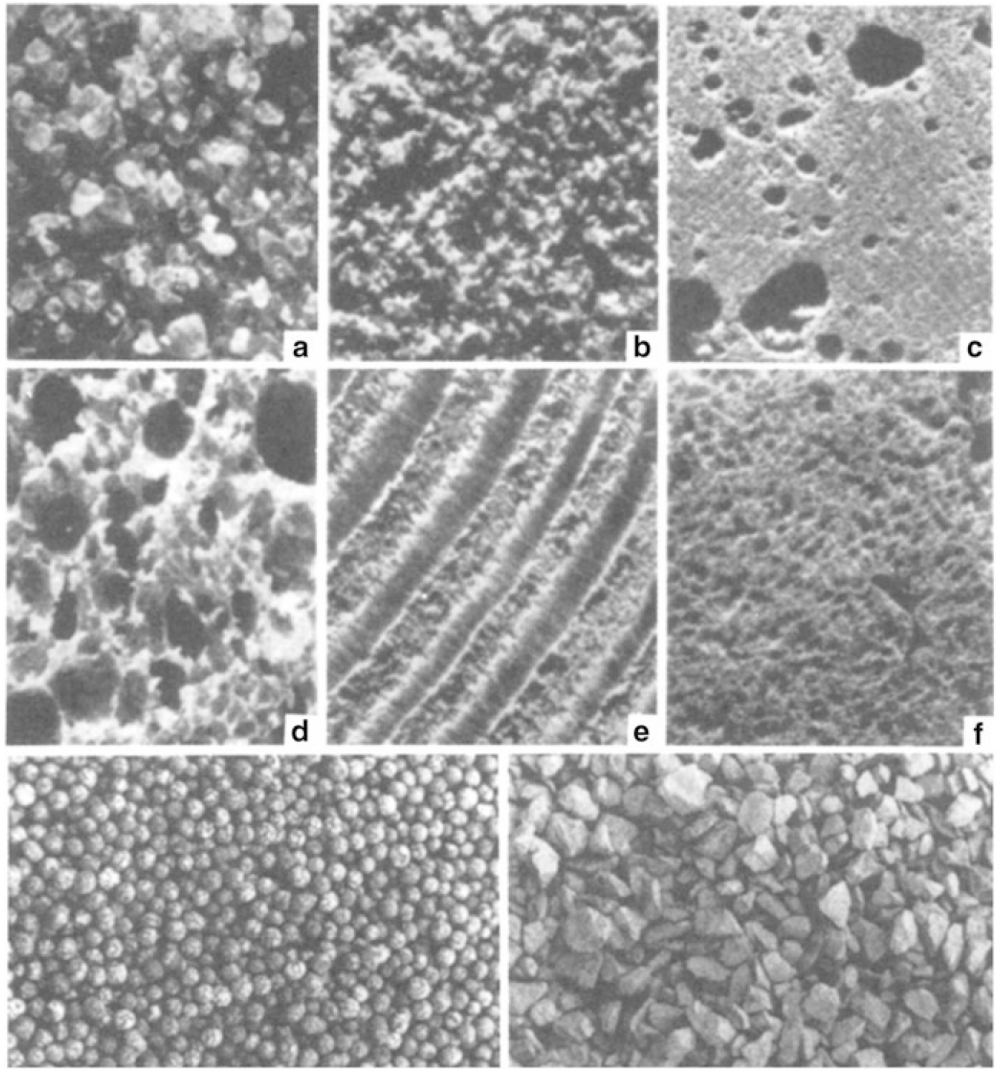


**Figure 1.1** Top rows show structure of several natural porous media: (a) beach sand, (b) sandstone, (c) limestone, (d) rye bread, (e) wood, and (f) human lung.[86] Bottom row shows structure of granular porous media made from Liapor® spheres with diameter of 0.5 cm (right) crushed limestone with diameter of 1 cm (left).[87]

At the pore scale, transport of Newtonian fluids through porous media at small Reynolds number $Re = \rho u_p l/\mu \ll 1$ is described by Darcy's law $-\nabla p = \frac{\mu u}{k}$, where $-\nabla p$ is the pressure gradient, $u$ is the Darcy velocity, $u_p$ is the pore-scale velocity, $\mu$ is the fluid dynamic viscosity, $k$ is the absolute permeability of the porous bed, $l$ is the length

scale characterizing the typical void size, and $\rho$ is the fluid mass density. Both numerical simulations[88–102] and experimental measurements using nuclear magnetic resonance[103–105] and optical methods[106–109] reveal that particle dispersion is anomalous and the velocity distribution is non-random in Newtonian solutions in porous media. Moreover, pore scale structure and degree of complexity of porous media affect velocity distribution and dispersion of particles.

Flow of non-Newtonian fluids in porous media on the other hand, includes additional complexity that arises from the interaction of coexisting shear and elongational flows with the converging-diverging pore structure.[110] Darcy's law is valid in non-Newtonian fluids when flow is adequately slow; this limit is associated with Deborah number $De = \lambda\gamma < 1$, where $\lambda$ is the relaxation time of non-Newtonian fluid and $\gamma$ is the characteristic shear rate. In this case, viscosity is replaced by effective viscosity $\mu^{eff}$, the shear-dependent viscosity of the non-Newtonian fluid.[111,112] At higher flow velocities, however, the pressure gradient increases non-linearly with flow velocity. This behavior is observed in polymer solutions with high $De$ number flowing through porous media or around confined cylinders due to elastic instability.[112–115] Flow-induced structure formation could also cause additional increase in pressure drop at high flow rate of polymer solutions, which can be attributed to blockage of the pores.[116,117] Recent studies using numerical simulation[118] and NMR measurements[119] on non-Newtonian fluids, however, show non-Newtonian characteristics such as yield stress and viscoelasticity are broken in porous media as pore structure becomes narrower. Here the complex structure

of the pores, which imposes flow deformation in all directions, is thought to be the reason for the breakage of non-Newtonian properties.

Models of pore scale behavior of transport of small solutes through porous media, however, do not sufficiently describe dynamical behavior of nanoparticles, specifically when pore size is comparable to particle size. Diffusional dynamics of nanoparticles in porous media are highly affected by hindered pore structures and molecular diffusion does not adequately describe diffusive behavior.[45,120] For example, the transverse dispersion of nanoparticles in periodic arrays of nanoposts[120] does not scale onto a velocity dependent master curve reflecting the dominant effect of confinement on transverse dispersion. This behavior is in sharp contrast with transverse dispersion of small solutes, which is superposed onto a master curve in such media.[104]

## 1.4 Problem Statement

Nanoparticles must effectively delivered to targeted locations for applications in drug delivery, enhanced oil recovery, nanocomposites, and ground water treatment. This goal, in turn, requires nanoparticles to remain dispersed during transport through non-Newtonian and complex media. The role of non-Newtonian characteristics on microscale dispersion of particles and macroscale mobility behavior, however, is not well understood. Moreover, the competing effects of spatial obstacles and dynamical macromolecules on confining the mobility of nanoparticle are not well studied.

## 1.5 Research Objectives

In this study, we investigate the role of confinements of geometrical obstacles and macromolecules on micro and macro scale mobility of nanoparticle through complex media. First we use fluorescence microscopy and single particle tracking to investigate diffusive dynamics of fluorescence polystyrene nanoparticles of diameter 400 nm in non-Newtonian hydrolyzed polyacrylamide (HPAM) solution. We find that diffusive mobility of nanoparticle is coupled to fluctuation of polymer dynamics at short time scales resulting sub-diffusive behavior. Polymer-particle dynamics decouple at a length scale comparable to particle size. Dynamics approach Fickian with effective diffusivity reflecting the local viscosity that affects particles diffusion. We then fabricate mono and bidisperse micro channels using glass particles with diameter of 5—30 μm to model disordered porous media with varying pore sizes and connectivity. We use confocal microscopy to visualize diffusive dynamics of nanoparticles suspended in Newtonian (glycerol/water mixture with concentration of 0 and 90 wt% of glycerol) μm and non-Newtonian (HPAM) solutions in the model porous media. We explore the role of non-Newtonian characteristics on diffusive mobility of nanoparticles in confined environment. We find that mobility of nanoparticles in polymer solution within porous media is controlled by two competing effects: hydrodynamics interaction arising from geometrical obstacles and depletion interaction resulting temporary adsorption of particles onto the surface of glass beads. Finally, we flow nanoparticles suspended in different fluids through porous media of varying characteristic pore sizes to examine the

effects of geometric confinement and fluid rheology on pore scale transport of nanoparticles in Newtonian and non-Newtonian solutions. We find that long time dispersion of nanoparticles in Newtonian and non-Newtonian solutions collapses onto a single master curve independent of fluid rheology. Results provide further insights into the confining parameters influencing diffusion and transport dynamics of nanoparticles through complex media.

## 1.6 Organization

This dissertation is organized as follows. Chapter 1 presents a literature review. Chapter 2 presents study of diffusive mobility of nanoparticles in hydrolyzed polyacrylamide (HPAM) solutions of varying concentration. The connection between micro and macro-scale dynamics of nanoparticles is also studied as the polymer concentration or the particle size are varied. Chapter 3 extends the investigation of nanoparticle mobility in complex fluids as porous media confine the nanoparticles. The dynamics of nanoparticles are quantified in Newtonian (water and glycerol/water solution) and non-Newtonian (HPAM) solutions to understand the role of confinement of by the porous structure and by the polymers on nanoparticle diffusion. Chapter 4 presents a study of nanoparticle transport in Newtonian and in non-Newtonian solutions through disordered porous media. The effects of solution viscoelasticity, flow properties, and pore size on transport dynamics of nanoparticles through random and mono-dispersed porous media with varying bead diameters of 5—30 μm are characterized using confocal microscopy and single particle tracking algorithm.[121] Chapter 5 extends the study of

transport of nanoparticles in Newtonian and non-Newtonian solutions through bidisperse porous media. The role of pore heterogeneity and connectivity is for the local and ensemble mobility of nanoparticles are explored in bidisperse porous media. Finally, Chapter 6 presents the major conclusions of this thesis and some directions for future research.

# Chapter 2

Note: The material in this chapter has been published in the journal *"Macromolecules"*.

Babaye Khorasani, F.; Poling-Skutvik, R.; Krishnamoorti, R.; Conrad, J. C. Mobility of Nanoparticles in Semidilute Polyelectrolyte Solutions. *Macromolecules* **2014**, *47*, 5328–5333.

## 2.0 Mobility of Nanoparticles in Semi-Dilute Polyelectrolyte Solutions

We measure the mobility of nanoparticles at low concentrations in non-Newtonian semi-dilute aqueous solutions of high-molecular-weight polyelectrolyte polymers. Using optical microscopy and particle tracking algorithms, we image and track hydrophilic polystyrene nanoparticles of diameter 400 nm moving in aqueous solutions of partially hydrolyzed polyacrylamide of molecular weight 8,000,000 Da and concentration of 0.042—4.2 g/L. The effective diffusivity of the nanoparticles in the semi-dilute polymer solutions, extracted from the long-time limit of the mean-squared displacement using the Stokes-Einstein relation, is greater than that calculated from the zero-shear-rate viscosity measured using bulk rheology. For concentrations $c > 0.42$ g/L, the mean-square displacements (MSD) of particles measured as a function of lag time revealed that the particle dynamics are subdiffusive at short time scales and are Fickian on long time scales. The timescale for the crossover from subdiffusive to Fickian dynamics increases

with increasing polymer concentration; moreover, it is longer than the relaxation time scale for polymer blobs and shorter than that for the chain. Our results suggest that the nanoparticle dynamics are coupled to those of the polymers on a length scale intermediate between the blob size and the end-to-end distance of the polymer.

## 2.1 Introduction

Understanding the mobility of nanoparticles in polymer solutions is required to optimize their transport properties for wide-ranging applications in enhanced oil recovery and polymer nanocomposites. For example, nanoparticles employed to increase oil recovery, through change in the wettability of rock surfaces or through profile control or conformance control, must be transported as components of a polymer-laden fluid to particular regions of the reservoir.[122–124] Similarly, attaining the optimal thermal, mechanical, electrical, and/or optical properties of polymer nanocomposites[25,125] requires excellent control over the distribution of nanoparticles during processing in polymer solutions or melts.[23,24] Likewise, conferring self-healing properties[126–130] to polymer nanocomposites requires mobile nanoparticles within a polymer matrix. In these examples, polymers within a solution or melt may hinder and confine the mobile nanoparticles. Despite these important practical applications, the fundamental mechanisms that influence nanoparticle mobility in polymer solutions remain poorly understood.

Particle mobility is best understood in the limit for larger submicron particles moving in a continuous medium. In a purely viscous solvent, submicron particles

undergo Brownian diffusion. Their one-dimensional ensemble-averaged mean-square displacement (MSD) $\left\langle \Delta x^2(\Delta t) \right\rangle = \left\langle \left( x(t+\Delta t) - x(t) \right)^2 \right\rangle$ scales linearly with the lag time, *i.e.*, $\left\langle \Delta x^2(\Delta t) \right\rangle = 2D\Delta t$. The diffusion coefficient $D$ is related to the viscosity $\eta$ of the background solvent through the Stokes-Einstein relation, $D = k_B T / 3\pi\eta d$, where $d$ is the diameter of the particle. Upon addition of polymer, the medium becomes viscoelastic rather than purely viscous and the motion of the particle probes both the elastic response as well as the viscous dissipation of the medium. In this scenario, the Stokes-Einstein relation for the diffusion coefficient is generalized to include a frequency-dependent viscosity, *i.e.* $D(s) = k_B T / 3\pi d s \tilde{\eta}(s)$ [Ref.[131]]. The generalized Stokes-Einstein relation (GSER) thus allows the complex viscosity to be extracted from the mean-squared displacements of tracer particles. Excellent agreement between macro- and micro-rheology, using micron-sized particles, has been reported for a wide variety of crosslinked and entangled polymer solutions.[132–142]

The validity of the GSER depends in part on a key underlying assumption, namely that the medium can be treated as a homogeneous continuum. When the size of the particle is much larger than typical length scales in the polymer solution (for example, the polymer radius of gyration in dilute solutions, the end-to-end distance in polyelectrolyte solutions, and the correlation length in semi-dilute solutions) this assumption is satisfied and particle diffusion is related to the macroscopic rheology through the GSER. When the size of nanoparticles is comparable to or smaller than length scales in the polymer solution, however, the medium cannot be treated a homogeneous continuum. Indeed, the

dynamics of nanoparticles in polymer solutions in this regime exhibit nontrivial and non-continuum dependencies on the characteristics of the polymer solution.[65,69,72,143–147] As one example, the diffusion coefficients of nm-scale particles in concentrated and entangled solutions are significantly *higher* than expected based on the bulk solution viscosity.[72,145,146] Both theoretical models and simulations[34,61,148,149] developed to explain these surprising results suggest that in concentrated solutions polymer entanglements play a critical role in controlling the nanoparticle dynamics. Polymer fluctuations on length scales ranging from individual chains[34] to the blob size[148] also impact nanoparticle dynamics. Even when the polymers are not entangled, however, they can act as mobile and compressible obstacles[150] through which the particles must diffuse.[151] This effect, termed macromolecular crowding,[152] can also lead to anomalous diffusion[153–159] through caging. Despite extensive work, how these competing mechanisms affect the motion of nanoparticles in polymer solutions remains poorly understood.

In this chapter, we investigate the mobility of nanoparticles in aqueous semidilute solutions of high molecular weight hydrolyzed polyacrylamide of concentration 0.042—4.2 g/L; the overlap concentration $c^*$, based on the intrinsic viscosity, is 0.16 g/L. The diameter of the nanoparticles (~400 nm) is smaller than the end-to-end distance of the polyelectrolyte polymers in dilute solution (~660 nm), significantly larger than the Kuhn segment length (~1 nm), and for the semi-dilute solutions larger than or comparable to the correlation length (~27-224 nm). We find that the mean-square displacement (MSD) is subdiffusive at short time scales for solutions of concentration $c > 0.42$ g/L and exhibits Fickian diffusion on longer time scales. The diffusion coefficient extracted from

the long-time slope of the MSD, however, is larger than that calculated from the macroscopic zero-shear-rate viscosity of the polymer solution measured using bulk rheology. This result suggests that the effective viscosity experienced by the nanoparticles is less than that measured in bulk rheology, as also previously found for nm-scale particles in polymer solutions.[69,145,146] Moreover, the experimental time scales for the crossover to Fickian dynamics are much longer than those predicted using models that couple the dynamics of the nanoparticles to those of polymer blobs.[34] Our results are consistent with caging of the nanoparticles by polymer segments: the crossover to diffusive dynamics appears upon relaxation of a polymer region of size intermediate between the blob size and the end-to-end distance, and the long-time diffusivity reflects the shear-thinning of the solution at the local deformation rate imparted by the nanoparticles.

## 2.2 Materials and Methods

### 2.2.1 Fabrication of glass sample chambers

The glass chamber was fabricated from two square cover slips of dimensions 22 mm × 22 mm and thickness of 0.19—0.23 mm (Fisherbrand cover glass) that were attached to a cover glass of dimensions 48 mm × 65 mm and thickness of 0.13-0.17 mm (Gold Seal cover glass) using a UV epoxy-based adhesive. The lateral distance between two cover glasses was approximately 20 mm. To form the chamber, a third small cover glass of dimensions 22 mm × 22 mm and thickness of 0.19-0.23 mm (Fisherbrand cover glass)

was affixed to the top of the small cover glasses and three sides of the chamber were sealed with UV epoxy.

### 2.2.2 Preparation of nanoparticle-polymer solutions

Fluoro-Max dyed red aqueous fluorescent polystyrene nanoparticles of diameter $d$ = 400 nm and microparticles of diameter $d$ = 2 μm were purchased at a concentration of 1 wt% from Thermo Fisher Scientific. These nanoparticles were stabilized in water by addition of trace amounts of surfactant. The density of the nanoparticles was 1.05 g/cm$^3$ at 25°C. The peak excitation and peak emission wavelengths for the fluorescence were 542 nm and 612 nm, respectively. Hydrolyzed polyacrylamide (HPAM) polymers of weight-averaged molecular weight ($M_w$) of 8,000,000 Da (FLOPAAM 3330) were obtained from SNF and used as received. The degree of hydrolysis was 25—30% as reported by the manufacturer.

### 2.2.3 Intrinsic viscosity

Solutions of various concentrations were prepared and then passed through a capillary viscometer to measure the solution viscosity. The capillary viscometer produced relatively large shear rates, estimated to be 297 s$^{-1}$. Although the solutions exhibit shear-thinning behavior, extrapolating to infinite dilution should still result in an accurate measurement of the intrinsic viscosity. Figure 2.1 shows the dependence of the solution viscosity on the concentration of HPAM. Normalizing this slope by the viscosity of the

solvent (0.89 mPa-s) gives the intrinsic viscosity of FLOPAAM 3330 to be 15.4 +/- 0.2 L/g, in accord with earlier experiments.[160,161]

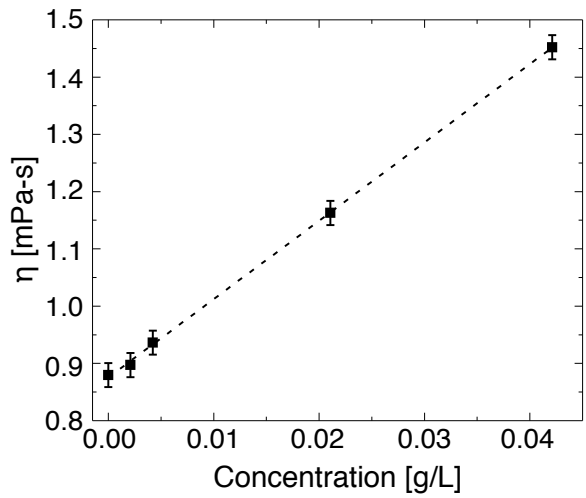


**Figure 2.1** Viscosity $\eta$ of FLOPAAM 3330 solutions at 25°C as measured in a capillary viscometer. The dashed line represents a linear fit with a slope of $13.7\ \mathrm{mPa \cdot s/(g/L)}$.

### 2.2.4 Overlap concentration

The Fox-Flory equation,[162] $[\eta] = \Phi r^3/M_w$, relates the intrinsic viscosity of a polymer solution to the mean-end-to-end distance $r^2$ and the polymer molecular weight $M_w$. The overlap concentration in a polymer solution defines the semi-dilute region and represents the concentration at which physical interactions between the polymer macromolecules begin to play a strong role. In this semi-dilute region, the polymer coils effectively begin to fill the entire volume of the solution. The critical concentration can be calculated assuming that the entire volume of solution is occupied by the polymer, i.e.,

$$c^* = \frac{M}{N_A v} = \frac{M}{N_A\left(\frac{4\pi}{3}R_g^3\right)}, \qquad 2\text{-}1$$

where $M$ represents the molecular weight of the polymer, $N_A$ is Avogadro's number, and $R_g$ is the radius of gyration.[163] This expression assumes that the polymer occupies the entire volume of the solution. Substituting in the Fox-Flory equation gives

$$c^* = \frac{6^{\frac{3}{2}}\Phi}{N_A 4\pi/3[\eta]} \approx \frac{2.5}{[\eta]}. \qquad 2\text{-}2$$

With an intrinsic viscosity of 15.4 L/g, the corresponding overlap concentration is 0.16 g/L. the resulting radius of gyration for FLOPAAM 3330 in dilute solutions is approximately 270 nm. For imaging, we prepared solutions at polymer concentrations ranging from 0.042—4.2 g/L, corresponding to 0.26—26$c^*$. The end-to-end distance in dilute solution $R_0 \approx 660$ nm was calculated using the Fox-Flory equation,[162] $[\eta] = \Phi R^3/M_w$, where $\Phi$ is the Flory constant, and the correlation length $\xi/R_0 \sim (c/c^*)^{-1/2}$ was estimated using a scaling relationship for polyelectrolytes.[164] Sample vials were cleaned with three organic solvents (toluene, tetrahydrofuran and acetone), rinsed with deionized water, and subsequently dried in a convection oven. Appropriate quantities of HPAM and deionized water were added to a cleaned vial to create a solution of known polymer concentration. The solution was then thoroughly mixed by tumbling on a roll mill for between two days and one week, depending on polymer concentration, until a uniformly homogeneous solution was obtained. Finally, nanoparticles were added to each homogenized solution at a concentration of 0.002 wt% for imaging experiments.

### 2.2.5 Imaging protocol

Each sample was confined in a thin glass chamber of thickness ~0.2 mm to prevent macroscopic motion. The chamber was filled with 100 μL of sample using a pipette and sealed using UV-curable epoxy. Samples were imaged using a Leica DM4000 inverted microscope equipped with a 100x lens with numerical aperture (NA) of 1.40. Two cameras with distinct ranges of video-capture frame rates were used to image the nanoparticles as they diffused in aqueous HPAM solutions. Movies were acquired at 32, 63, or 120 frames per second (fps) using a AOS Technologies AG camera (S-PRI) with a pixel size of 0.195 ± 0.002 μm, and 0.67, 1, 1.67 or 2.5 fps using an Olympus camera (DP21) with a pixel size of 0.1266 ± 0.0012 μm. We acquired multiple movies of each sample at different frame rates and thereby accessed the dynamics of the nanoparticles across a wide range of timescales (0.008—450 sec).

### 2.2.6 Particle-tracking

We used particle-tracking algorithms[165] to locate and track the nanoparticles in a time-series of fluorescence micrographs. Images from a time series were first de-noised using a bandpass filter to remove the background intensity. The centroids of all particles were then located with resolution of $\varepsilon$ = 40 nm (by refining the locations of the local maxima of intensity) and subsequently linked into trajectories. From the trajectories of the nanoparticles, we calculated the one-dimensional ensemble-averaged mean-squared displacement (MSD) of the particles $\left\langle \Delta x^2(\Delta t) \right\rangle$. Although we measured the dynamics

across a wide range of time scales, we reported here only those mean-squared displacements greater than $2\varepsilon^2$ that corresponded to displacements that could be resolved using the tracking technique.

### 2.2.7 Bulk rheological measurements

To measure the rheological properties of the semi-dilute polymer solutions we used a TA DHR rheometer equipped with a Couette geometry (cup diameter of 30.36 mm, bob diameter of 27.97 mm, bob length of 41.89 mm, and gap height of 4 mm). Samples were gently loaded into the instrument prior to measurements, and we ensured that no bubbles were present inside the sample after loading. We measured the frequency-dependent linear elastic ($G'(\omega)$) and viscous ($G''(\omega)$) moduli over the frequency range ω = 100 to 0.01 rad/sec. We carefully confirmed that our rheological measurements were reproducible and time-independent using the following protocol. At the highest frequencies (100—10 rad /sec) we applied the minimum strain that generated a torque exceeding the minimum detectable torque of the rheometer (0.1 μN-m). At each lower decade we doubled the strain and checked that the torque remained in the reliably measureable range of the instrument. We also verified that the sample remained in the linear viscoelastic regime at each decade. Finally, we confirmed that the mechanical properties of the sample remained constant over time by rerunning the highest frequencies (100—10 rad/sec) at the end of the experiment. From the frequency-

dependent moduli, we calculated the complex viscosity as $\eta^*(\omega) = \sqrt{G'^2(\omega) + G''^2(\omega)} / \omega$ and reported the complex viscosity as a function of the frequency.

Polymer solutions of concentration $c \leq 0.42$ g/L did not generate sufficient torque, and we were unable to characterize the full frequency-dependent viscosity for these solutions. Instead, we used two capillary viscometers (sizes 0B and 0C, Cannon 9721-R56 and 9721-R53) to measure the solution viscosity for polymer solutions with concentration $c \leq 0.042$ g/L. Prior to each experiment, the viscometers were rinsed with acetone and deionized water, dried in an oven at 130ºC for 15 minutes, and cooled by passing nitrogen through the viscometer. The effective shear rates were estimated as $\dot{\gamma} = 8V/D$, where $V$ was the average velocity of the solution moving through the viscometer and $D$ was its diameter, as 297 $s^{-1}$ (0B) and 233 $s^{-1}$ (0C).

### 2.2.8 Dynamic light scattering (DLS)

To determine whether the polymers irreversibly adhered to the particles, the hydrodynamic size of the particles as a function of polymer concentration was determined using dynamic light scattering. Dynamic light scattering data were collected on a Brookhaven Instruments goniometer (BI-200SM, Brookhaven Instruments Corporation) that was equipped with an avalanche photodiode detector (Brookhaven, BI-APD) and a digital correlator (Brookhaven, TurboCorr), which calculated the photon intensity autocorrelation function at different scattering angles for incident light of wavelength $\lambda$ = 637.6 nm (Mini-L30 laser source). Sample vials inserted into the DLS

sample holder were first rinsed with soapy water and cleaned with acetone and lens paper to minimize scattering due to contaminants or dirt. We prepared a series of particle-polymer mixtures at very dilute concentrations of polymer ($0.02c^*$, $0.2c^*$, $0.39c^*$, and $0.64c^*$) and at fixed particle concentration of $10^{-6}$ g/mL. We collected the scattered light at a fixed scattering angle $\theta$ for 30 s and repeated this measurement 10 times to obtain the average intensity-intensity correlation function $g^2(\tau, q) = \langle I(t+\tau)I(t)/I(t)\rangle^2$ at 200 delay times ranging between 2 μs and 6 s. We used the Siegert relation to obtain the first-order autocorrelation function from the intensity-intensity correlation function, $g^2(\tau, q) = 1 + \beta g^1(\tau, q)$; here $\beta$ is a correction factor that depends on the alignment and geometry of the laser beam in the scattering setup and is close to 1. Because the polymer solutions were dilute and the nanoparticles strongly scattered the incident light, the photon-photon correlation functions could be fit by a single exponential decay, *i.e.* $g^{1(q,\tau)} = \exp\left(-\frac{t}{\tau_q}\right)$, from which we extracted a wavevector-dependent relaxation time $\tau_q$. Finally, we calculated the diffusivity as $D_m = 1/\tau_q q^2$ and used the Stokes-Einstein relationship to obtain the hydrodynamic radius of the nanoparticles from $D_m$ as a function of polymer concentration. We performed DLS measurements at 4 different scattering angles (45°, 60°, 75°, and 90°, corresponding to scattering angles of 1.01, 1.32, 1.60, and 1.86 $\mu m^{-1}$, respectively) to sensitively assess the measurement error.

## 2.3 Results and Discussion

The mobility of the nanoparticles in the polymer solutions, as measured by particle tracking methods, qualitatively and quantitatively changed with increasing polymer concentration as shown in Figure 2.2. At low concentrations of polymer (0.042 g/L) the dynamics of the nanoparticles were nearly diffusive, as indicated by the linear fits to the mean-squared displacement (MSD) $\left\langle \Delta x^2(\Delta t) \right\rangle = 2D\Delta t$ over all time scales.

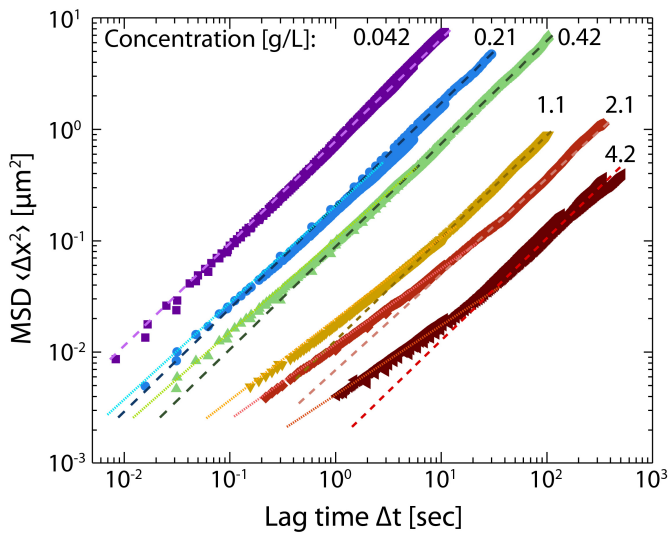


**Figure 2.2** Mean-squared displacement (MSD) as a function of lag time Δt for 400 nm diameter nanoparticles in aqueous solutions of solutions of hydrolyzed polyacrylamide of varying concentration c. Dashed lines indicate linear fits (power law exponent of one) at long time scales; dotted lines indicate power-law fits with varying exponent at short time scales.

When the polymer concentration was increased above 0.42 g/L, the slope of the MSD as a function of lag time at short times (on a log-log scale) was less than one, indicating the emergence of subdiffusive dynamics on short time scales. Subdiffusive exponents for nanoparticle mobility in neutral polymer solutions are often attributed to entanglements,[146] but entanglement effects in salt-free solutions of high molecular weight

polyelectrolytes typically do not appear until concentrations that are much larger than $c^*$ (estimated as >1000$c^*$ for a molecular weight of 8,000,000 [Ref.[166]]). The slope of the short-time MSD as a function of lag time decreased as the concentration of polymer was increased from ~0.8 at 0.42 g/L to ~0.4 at 4.2 g/L. On long time scales the dynamics of the nanoparticles were Fickian diffusive, as indicated by the linear dependence of the MSD on lag time for all samples (0.042—4.2 g/L). The time at which the dynamics exhibited the crossover to Fickian diffusive behavior increased from ~5 s at 0.42 g/L to ~30 s at 4.2 g/L. The distributions of particle displacements, however, remained Gaussian on all time scales (Figure 2.4—Figure 2.8). We concluded that on long time scales the nanoparticles diffused in an effective medium and extracted an effective long-time diffusion coefficient $D_{\mathrm{eff}}$ for each polymer concentration from the long-time slope of the MSD.

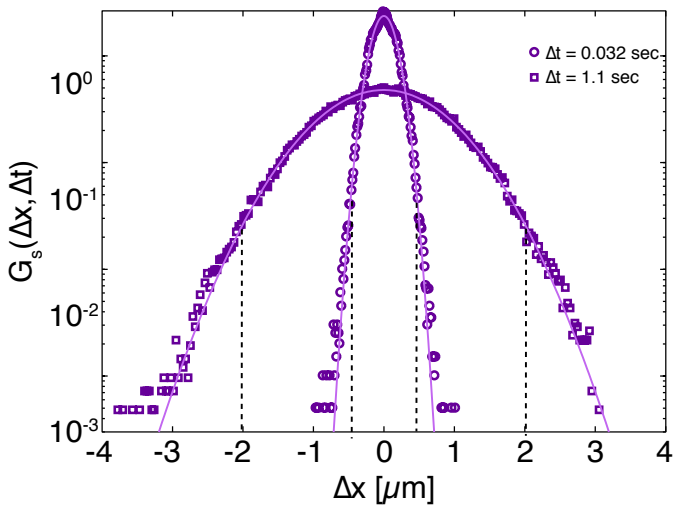


**Figure 2.3** Probability distribution of particle displacements as a function of displacement $\Delta x$ for 400 nm nanoparticles in a polymer solution with concentration 0.042 g/L. Solid lines indicate fits to Gaussian distributions fit to histogram bins containing at least 100 points, indicated by dashed vertical lines.

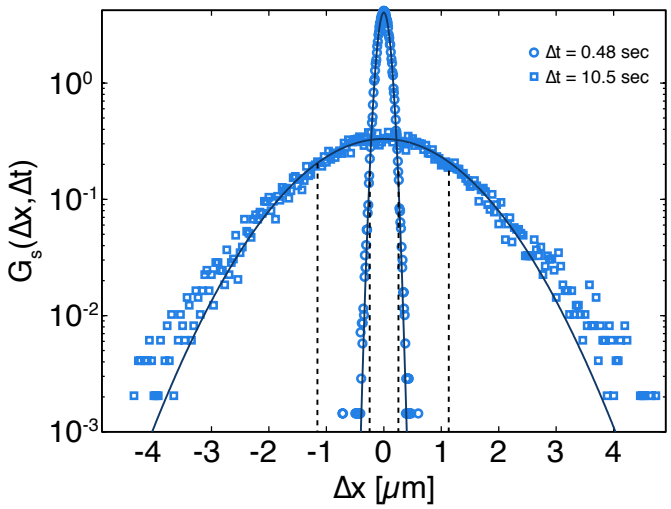


**Figure 2.4** Probability distribution of particle displacements as a function of displacement $\Delta x$ for 400 nm nanoparticles in a polymer solution with concentration 0.21 g/L. Solid lines indicate fits to Gaussian distributions fit to histogram bins containing at least 100 points, indicated by dashed vertical lines.

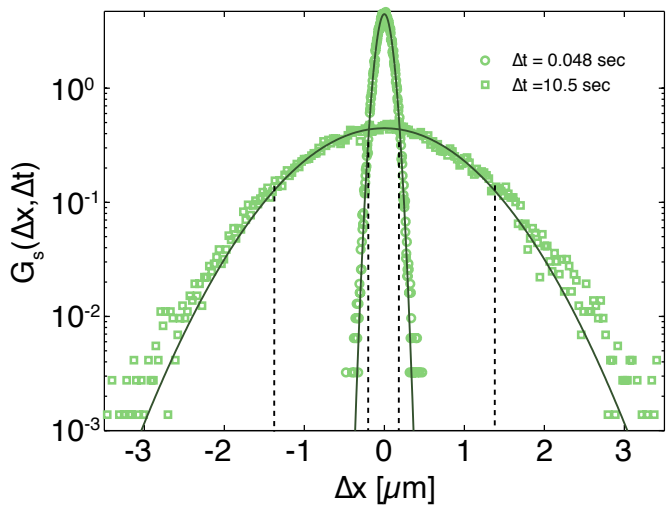


**Figure 2.5** Probability distribution of particle displacements as a function of displacement $\Delta x$ for 400 nm nanoparticles in a polymer solution with concentration 0.42 g/L. Solid lines indicate fits to Gaussian distributions fit to histogram bins containing at least 100 points, indicated by dashed vertical lines.

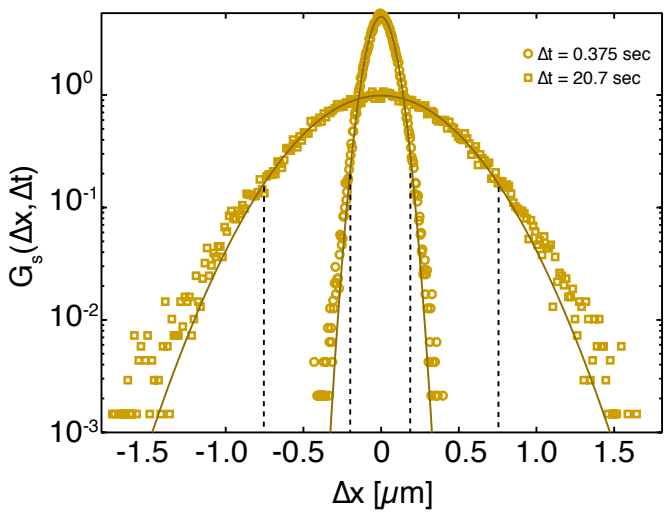


**Figure 2.6** Probability distribution of particle displacements as a function of displacement $\Delta x$ for 400 nm nanoparticles in a polymer solution with concentration 1.1 g/L. Solid lines indicate fits to Gaussian distributions fit to histogram bins containing at least 100 points, indicated by dashed vertical lines.

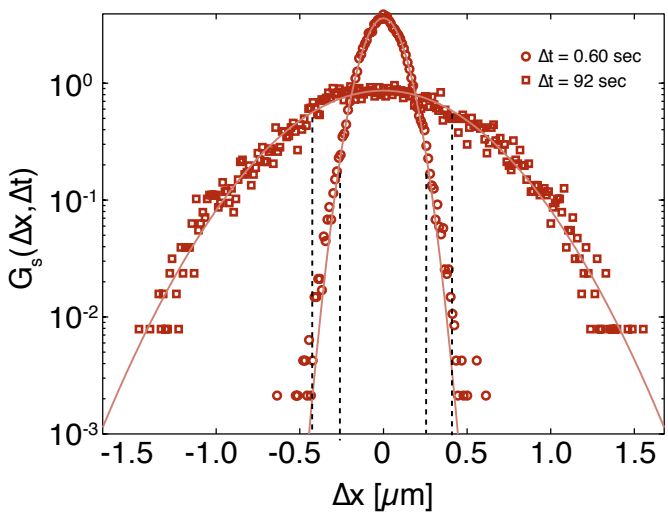


**Figure 2.7** Probability distribution of particle displacements as a function of displacement $\Delta x$ for 400 nm nanoparticles in a polymer solution with concentration 2.1 g/L. Solid lines indicate fits to Gaussian distributions fit to histogram bins containing at least 100 points, indicated by dashed vertical lines.

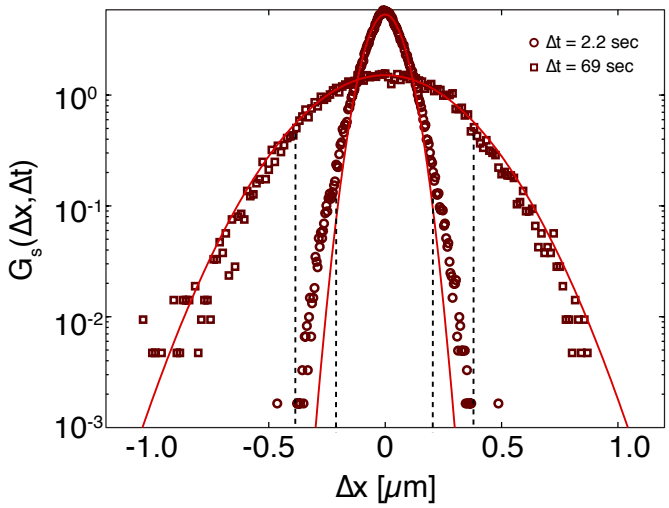


**Figure 2.8** Probability distribution of particle displacements as a function of displacement $\Delta x$ for 400 nm nanoparticles in a polymer solution with concentration 4.2 g/L. Solid lines indicate fits to Gaussian distributions fit to histogram bins containing at least 100 points, indicated by dashed vertical lines.

In homogeneous solutions, the diffusion coefficient of particles of diameter $d$ in a homogeneous solution is related to the solution viscosity using the Stokes-Einstein equation, $D = k_B T / 3\pi\eta d$, where $T$ is the temperature and $\eta$ is the viscosity of the solution. We thus compared the effective diffusivity $D_{\text{eff}}$, obtained from the long-time particle tracking data, with that calculated from Stokes-Einstein ($D_{SE}$), obtained from the measured bulk zero-shear rate viscosity and the known particle diameter. For polymer concentrations greater than 0.42 g/L we measured the bulk solution viscoelasticity using rheology. The bulk viscosity of the semi-dilute polymer solutions was strongly shear-thinning, as shown in Figure 2.9. At low shear rates the viscosity was nearly independent of shear-rate (*i.e.,* Newtonian). We thus extracted the low-shear-rate viscosity that characterized the bulk viscosity in a quiescent solution and thereby calculated $D_{SE}$. Polymer solutions with concentrations below 0.42 g/L did not generate sufficient torque

in the rheometer to allow measurements of the zero-shear-rate viscosity. Instead, we employed capillary viscometry to measure the solution viscosity at a finite shear rate and similarly calculated the effective diffusivity $D_{SE}$ at $c$ = 0.042 g/L.

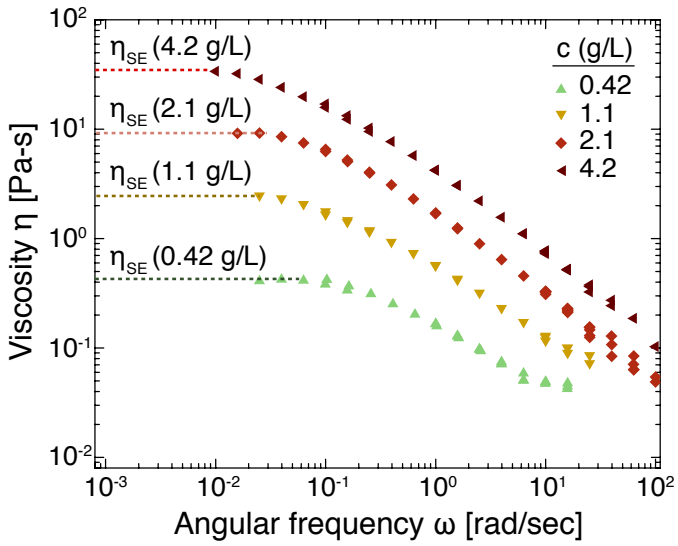


**Figure 2.9** Viscosity $\eta$ as a function of angular frequency $\omega$ for solutions of hydrolyzed polyacrylamide with varying concentration $c$ (in units of g/L). The dashed-lines indicate the values of the low-shear viscosity $\eta_{SE}$ extrapolated from the measured viscosity for each concentration.

We observed significant discrepancies between the microscopic $D_{\text{eff}}$ and macroscopic $D_{SE}$ for solutions of concentration $c \geq 0.42$ g/L, as shown in Figure 2.10. For polymer concentrations greater than 0.42 g/L we found that $D_{\text{eff}} > D_{SE}$, as was observed for much smaller nanoparticles in polymer solutions and melts.[72,145] The ratio $D_{\text{eff}}/D_{SE} \sim 10$ was approximately constant over the concentrations probed, similar to that obtained with smaller nanoparticles at comparable $d/R \sim 0.6$ in solutions of neutral polymers [Ref.[72]]. At lower polymer concentrations the discrepancy between $D_{\text{eff}}$ and $D_{SE}$ largely vanished. For a polymer concentration of 0.042 g/L we found that $D_{SE}$ was slightly larger than $D_{\text{eff}}$, which we attributed to shear-thinning of the polymer solution at the shear rate (233 $s^{-1}$) at which the viscosity was measured.

Figure 2.10 represents nanoparticle diffusivity $D_{eff}/D_s$ extracted from the long-time mean-squared displacements as a function of the normalized polymer concentration $c/c^*$ (open symbols). Solid symbols indicate the diffusivity calculated from experimental measurements of the bulk viscosity: squares use the zero-shear viscosity measured for solutions with $c/c^* \geq 2.6$ (corresponding to $c \geq 0.42$ g/L) and the star ($c/c^* = 0.26$, corresponding to $c = 0.042$ g/L) use the viscosity measured at a shear rate of 233 $s^{-1}$ using a capillary viscometer. The dashed and solid lines show fits to models by References 52 (for all data) and 35 (for $c/c^* > 1$ only), respectively.

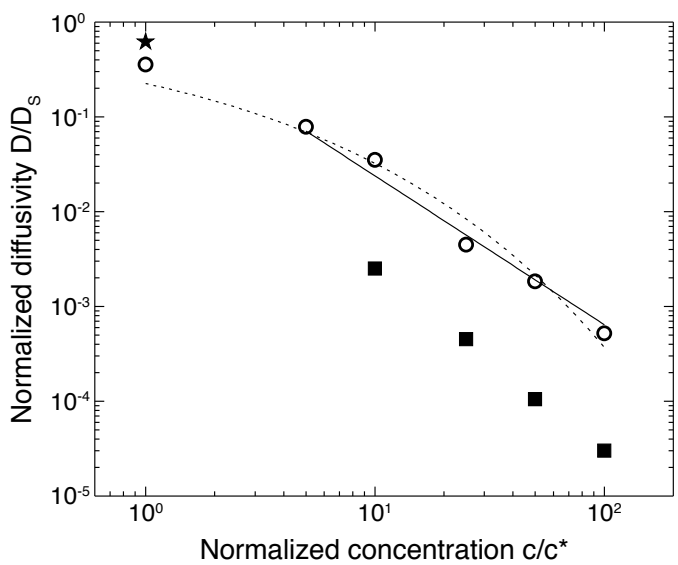


**Figure 2.10** Nanoparticle diffusivity $D_{eff}/D_s$ extracted from the long-time mean-squared displacements as a function of the normalized polymer concentration $c/c^*$ (open symbols). Solid symbols indicate the diffusivity calculated from experimental measurements of the bulk viscosity.

The discrepancy between $D_{\text{eff}}$ and $D_{SE}$ observed here for the 400 nm diameter nanoparticles, like that observed earlier for smaller nanoparticles,[72,145,146] suggests that the dynamics of nanoparticles of size comparable to the polymer coils do not probe the

bulk rheological properties of polymer solutions. Because particles whose size is much larger than characteristic length scales are known to probe the bulk rheology of polymer solutions,[132–136,139–142] we measured the mean-squared displacement (MSD) using surfactant-stabilized polystyrene microparticles of diameter 2 μm in a HPAM solution with a polymer concentration of 2.1 g/L. For these particles the ratio of the particle size to the end-to-end distance of the polymers was $d/R \sim 3$. For the larger particles the long time MSD dependence was again consistent with diffusive dynamics, as shown in Figure 2.11. Furthermore, the diffusivity extracted from the long-time slope of the microparticles was much closer to the low-shear-rate viscosity measured using bulk rheology; we attributed the factor of two difference in diffusivities (and hence in effective viscosities) to the relatively small $d/R \sim 3$ of the microparticles. This experiment indicated that bulk solution viscosity would be recovered as the size of the particles was increased.

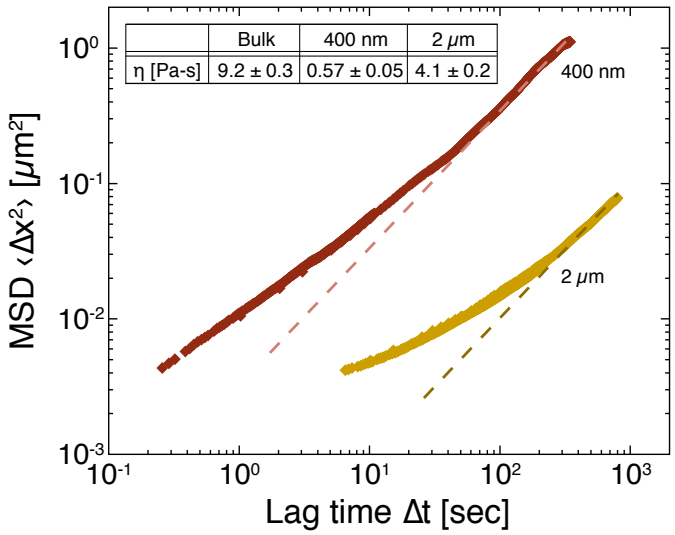


**Figure 2.11** Mean-squared displacement (MSD) as a function of time for particles of diameter 400 nm and 2 μm diffusing in a polymer solution with concentration 2.1 g/L. Inset table: viscosity η extracted from the low-shear-rate bulk rheology and from the long-time limit of the MSD for 400 nm and 2 μm particles.

From the microscopy studies, we summarize two key results for the diffusion of nanoparticles in high-molecular-weight polyelectrolyte solutions. First, for concentrations $c \geq 0.42$ g/L the nanoparticles exhibited subdiffusive dynamics on short time scales. Second, the dynamics of nanoparticles for all solutions were diffusive on long time scales, but the diffusivity extracted from the long-time slope of the MSD was over an order of magnitude larger than that calculated from the zero-shear-rate viscosity of the polymer solutions. We note that the concentration dependence of $D_{\text{eff}}$ alone does not provide insight into the mechanisms driving the dynamics: over the range of polymer concentrations probed in this study, both a stretched-exponential model, $D_{\text{eff}} \propto \exp(-c^{\nu})$ [Ref. [52]] and a scaling model, $D_{\text{eff}} \propto (c/c^{*})^{-1.52}$ [Ref. [35]] could describe the concentration dependence of $D_{\text{eff}}$, as shown by the fits in Figure 2.10.

We first considered several mechanisms for the origin of the subdiffusive dynamics at short times. The first potential mechanism is solution elasticity: micron-sized particles diffusing in entangled or crosslinked polymer solutions exhibit subdiffusive dynamics on short time scales that are coupled to the elasticity of the solution,[133,136] as described quantitatively using the generalized Stokes-Einstein equation.[131] One-point microrheology measurements for the linear elastic and viscous moduli, however, also deviated from the bulk values (Figure 2.12). Separately, we note that the polymer concentrations examined here are significantly smaller than those for which the effects of entanglements are observed for polyelectrolyte solutions. We thus contend that the

subdiffusive dynamics of the nanoparticles in semi-dilute polyelectrolyte solutions does not reflect the bulk rheological properties of the solution.

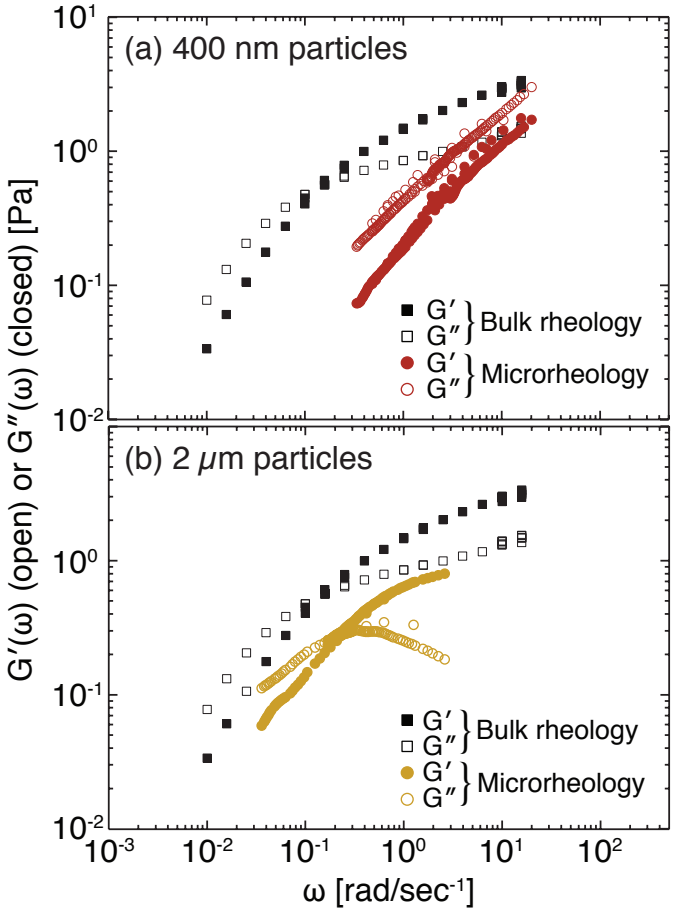


**Figure 2.12** Elastic (closed symbols) and viscous (open symbols) moduli as a function of frequency ω for a polymer solution with concentration 2.1 g/L. Squares: measured using bulk rheology. Circles: measured using one-point microrheology with 400 nm (a) and 2 μm (b) diameter particles.

We next considered the possibility that the polymers irreversibly adhered to the nanoparticles, as earlier experiments found that polymer sticking could lead to subdiffusive exponents of ~0.5 that reflected the Rouse-like dynamics of the polymers.[167,168] To test this idea, we formulated dilute solutions of polymer at concentrations ranging from 0.00084—0.027 g/L containing nanoparticles of 400 nm and

measured the hydrodynamic radius of the nanoparticles using dynamic light scattering. Within experimental error, the hydrodynamic radius of the particles was constant across the range of polymer concentrations probed (Figure 2.13), indicating that the polymers did not strongly interact with the nanoparticles.

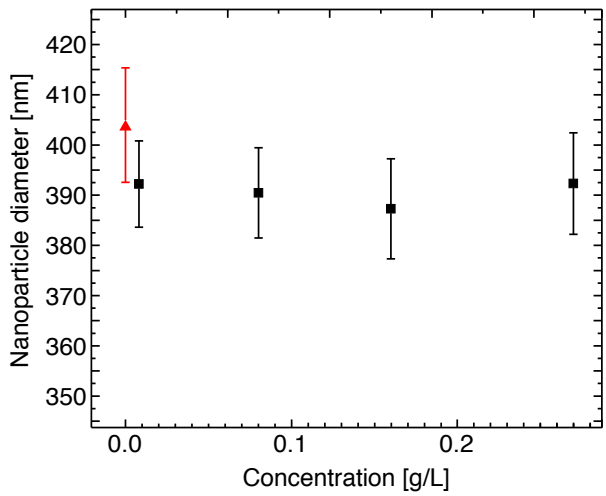


**Figure 2.13** Nanoparticle diameter as a function of polymer concentration c (in g/L) measured using dynamic light scattering. The red triangle indicates the measurement taken in water; the black squares indicate measurements taken in dilute polymer solutions.

Finally, we considered the possibility that the subdiffusive dynamics reflected coupling between particle and polymer dynamics. We tested this idea using the scaling model of Rubinstein and collaborators,[34] which predicts a crossover from subdiffusive to diffusive behavior for particles whose size falls between the correlation length (which we estimate for polyelectrolytes[164] as $\xi/R_0 \sim (c/c^*)^{-1/2}$) and the tube diameter; because our solutions are not entangled this intermediate regime is the relevant one for our experiments. The timescale for the crossover from subdiffusive to diffusive dynamics obtained from this model, $\tau_d \sim (\eta_s \xi^3/k_B T)\left(\frac{2a}{\xi}\right)^4 \sim \eta_s\,(2a)^4/(k_B T\,\xi)$, is much shorter

than the crossover time scale that we observed in experiments for all polymer concentrations (*e.g.* for $c$ = 2.1 g/L, $\tau_d$ ~ 0.041 s from the Rubinstein model and the experimental crossover occurs at ~19 s; estimated time scales for the crossover and for the blob size relaxation are given in Table 2.1). This comparison suggests that polymer dynamics at the blob and particle scales do not control the particle dynamics.

**Table 2.1** Correlation blob relaxation time $\tau_\xi$ and particle diameter relaxation time $\tau_d$, calculated from Cai *et al.*, *Macromolecules* **44**, 7853-7863 (2011); and experimental crossover time $\boldsymbol{\tau_c}$, extracted from the MSD measurements; and longest Rouse timescale $\tau_r$, extracted from the bulk rheology.

| $c/c^*$ | 6.7 | 17 | 33 | 67 |
|---|---|---|---|---|
| $\tau_\xi$ [s] | $5.9 \times 10^{-3}$ | $1.5 \times 10^{-3}$ | $5.2 \times 10^{-4}$ | $1.3 \times 10^{-4}$ |
| $\tau_d$ [s] | $1.8 \times 10^{-2}$ | $2.9 \times 10^{-2}$ | $4.1 \times 10^{-2}$ | $5.8 \times 10^{-2}$ |
| $\tau_c$ [s] | $5 \times 10^{0}$ | $1.1 \times 10^{1}$ | $1.9 \times 10^{1}$ | $2.7 \times 10^{1}$ |
| $\tau_r$ [s] | $8 \times 10^{0}$ | $1.5 \times 10^{1}$ | $3.1 \times 10^{1}$ | $6.2 \times 10^{1}$ |

Instead, we suggest a physical picture for subdiffusive motility in the semidilute regime that is motivated by comparisons to caged or crowded systems. In those systems, subdiffusive particle dynamics can indicate the presence of obstacles that locally cage the particle on short time scales; the transition from subdiffusive to diffusive motility occurs when this local cage relaxes and the particle escapes. In our semidilute solutions, the nanoparticles are caged by the large polymers. We suggest that the transition to diffusive mobility occurs when the cage formed by the polymers relaxes. This relaxation must occur over multiple blobs, because the transition to diffusive motility occurs on longer time scales than $\tau_d$. Similarly, this relaxation must occur on length scales smaller than the end-to-end distance, because the transition occurs on shorter timescales than the characteristic timescale for chain diffusion (*e.g.*, for $c$ = 2.1 g/L, the Rouse timescale is ~

31 seconds as estimated from Figure 2.2). These comparisons suggest that the length scale over which the local cage must relax is intermediate between the blob size and the end-to-end distance of the polymer. This length scale may be set by transient clustering[169] between polymer segments, which is thought to generate a slow relaxation in polymer solutions in less-good solvents whose concentration is intermediate between the overlap and entanglement concentrations.

This picture is also consistent with the faster-than-expected mobility of the nanoparticles in the polymer solutions. On long time scales the nanoparticles exhibit free diffusion, but in an effective medium of lower viscosity than the zero-shear-rate bulk viscosity. As before, we note that the faster-than-expected dynamics cannot reflect the viscoelasticity of the polymer solution or nanoparticle-polymer adhesion – indeed, these mechanisms would lead to *slower* mobility. Instead, the lower effective viscosity also reflects the coupling between nanoparticle and polymer dynamics[34] through local relaxation. The local rate at which the nanoparticles deform the polymer matrix is nonzero; because the polymer solutions are shear-thinning, the nanoparticles thus experience a viscosity that is lower than that at zero-shear-rate.

## 2.4 Conclusions

We measured the mobility of nanoparticles of diameter 400 nm in solutions of high-molecular weight hydrolyzed polyacrylamide of end-to-end distance 660 nm. For solutions in which the polymer concentration is greater than the overlap concentration, the dynamics changes from subdiffusive at short time scales to diffusive on long time

scales. The timescale at the crossover between these dynamics increases with polymer concentration. The effective diffusivity extracted from the long-time dynamics, however, is always greater than that calculated from the zero-shear-rate bulk viscosity. The lower-than-expected effective viscosities experienced by the nanoparticles (for $c > 0.42$ g/L) suggests that their dynamics are coupled to polymer fluctuations, as observed and predicted for smaller nanoparticles (~nm) that sample dynamics on the scale of polymer chain segments. Because the transition from subdiffusive to diffusive mobility occurs on time scales intermediate between the relaxation time scales for polymer blobs and for self-diffusion, we suggest that the length scale controlling the coupling of nanoparticle and polymer dynamics is intermediate between the blob size and the end-to-end distance. On short time scales the nanoparticles are caged by the polymers; on longer time scales this local cage relaxes to allow the nanoparticle to freely diffuse in an effective medium whose viscosity reflects the shear-thinning nature of the polymer solution.

This physical picture suggests an origin for both of the distinctive features of nanoparticle mobility in polyelectrolyte solutions observed here. An open question, however, is the physics that sets the size of the relaxing region that controls the crossover from subdiffusive to diffusive mobility. Similar measurements over a wide range of particle-to-polymer size ratios and particle-polymer interactions are needed to identify this critical length scale and are underway. We note that the static and dynamic behaviors of polyelectrolytes are somewhat more complex than those of polymers due to the presence of charges; in particular, the role of both solvent quality and counterion concentration may significantly affect the polymer dynamics and hence those of the

nanoparticles. Nonetheless, we expect these results to have interesting implications for nanoparticle diffusion in a wide range of polymer and polyelectrolyte solutions, including nanoparticle-based strategies to change the interfacial interactions in highly confined porous media to enhance oil recovery and processing strategies to fabricate advanced polymer nanocomposites.

# Chapter 3

Note: The material in this chapter is being submitted for publication.

## 3.0 Confined diffusive dynamics of nanoparticles suspended in Newtonian and non-Newtonian solutions within porous media

Diffusive dynamics of nanoparticles in porous media depend on pore size. We study diffusive mobility of 400 nm polystyrene nanoparticles in confined porous media using confocal microscopy. We use single particle tracking to measure mean squared displacements (MSD) and diffusion coefficient of nanoparticles suspended in Newtonian and non-Newtonian solutions. We observed that mobility of nanoparticles in porous media slows down as the average pore size decreases. Moreover, the distributions of particle displacements exhibit non-Gaussian behavior in both Newtonian and non-Newtonian solutions. Spatial heterogeneities of the porous media hinder the diffusive dynamics in both solutions, reflecting the role of hydrodynamic interactions on slowing the mobility. In non-Newtonian solutions, however, additional effect arising from depletion of polymer molecules in diffusion of particles near the confined surfaces results temporary adsorption of particles onto the surface of glass beads. Diffusive dynamics of nanoparticles in polymer solution is therefore controlled by two competing parameters: hydrodynamic interactions between particles and spatial obstacles and weak depletion interactions between particles and confining walls due to macromolecule depletion.

## 3.1 Introduction

Hindered mobility in confined media is of crucial importance in technological and scientific areas ranging from catalytic and biological reactions to membranes. As particles are increasingly confined, dynamics become slower and may even eventually become arrested. Such arrested dynamics typically control transport of particles in biological cells,[170–174] zeolites,[175] heterogeneous catalysts,[85,176,177] size exclusion chromatography,[178] membranes,[179] and nanocomposites.[23,25] Fundamental understanding of diffusion in many of these applications is further complicated by the presence of complex fluids containing polymers, surfactants, or micelles. As a result, understanding the effects of confinement on the dynamics of polymers is an important question.

In geometrically crowded environments, the mobility of nanoparticles depends on the spatial and dynamical heterogeneity of the environment.[29] For porous media, the spatial structure, void accessibility, and connectivity of the confined media influence diffusion.[29–31] As examples, the diffusion of smaller nanoparticles in large colloidal suspensions[32,33] and in entangled or unentangled polymer matrices[34–40] is hindered by dynamical networks that may be rigid, semi-flexible, or flexible. Mobility is also decreased when nanoparticles diffuse in ordered[41–43] or disordered[44–46] porous media or when polymer chains diffuse close to protonated[47,48] or patterned[49] surfaces. Mobility of nanoparticles depends on the relative size of the particles to the length scales of the void space. Generally, the diffusion of particles hindered by geometric confinement becomes slower as the confinement is increased. Although diffusion dynamics remain Fickian on

long time scales, the distributions of particle displacements become increasingly non-Gaussian, representing heterogeneities of the environment.

When the geometric medium itself can relax (for example, by diffusion of large colloidal bed particles[32,77,79,82] or by relaxation of an entangled polymer network[38,39,69,142,148,153,180–182]) the diffusional dynamics of nanoparticles can become coupled to the dynamics of the surrounding medium. Despite all the studies, competing effects of confinement by a rigid fixed network and by polymer chains on particle dynamics remain poorly understood.

Previous studies have mainly focused either on dynamical or spatial heterogeneities. In this chapter, we explore the simultaneous effects of spatial confinement from an arrested geometrical structure and from dynamic polymer molecules on the diffusive mobility of nanoparticles. We measure the diffusional dynamics of polystyrene nanoparticles of diameter of 400 nm in model porous media consisting of glass beads of diameter 5.4, 10, or 30 μm. To elucidate the role of non-Newtonian fluid characteristics in dynamics of nanoparticles in complex media, we use three different background solutions: Newtonian water, a Newtonian mixture of glycerol and water, and a non-Newtonian solution of semidilute hydrolyzed polyacrylamide. Nanoparticles are imaged using confocal microscopy and tracked over time; from their trajectories, we calculate the mean-square displacement. As the confinement length decreases, the dynamics of the nanoparticles become increasing slow and the distributions of particle displacements become increasingly non-Gaussian. For nanoparticle diffusion in HPAM, the distribution of particle displacements shows a distinct peak at zero, which reveals an immobile

population in displacements. We separately analyze the dynamics of mobile and immobile particles and show that, when the dynamics of transiently immobile nanoparticles are excluded, the diffusivities of mobile nanoparticles approach free diffusion. These results suggest that the slowing of diffusion arises because particles become partially immobilized in the beds due to temporary adsorption mediated by the polymer chains via depletion interactions.

## 3.2 Materials and methods

### 3.2.1 Preparation of nanoparticle dispersions in Newtonian and non-Newtonian solutions

Fluoro-Max dyed red aqueous fluorescent polystyrene nanoparticles of diameter $d_{NP}$ = 400 nm at concentration of 1 wt % were purchased from Thermo Fisher Scientific. Hydrolyzed polyacrylamide (HPAM) polymer of weight-averaged molecular weight (Mw) of 8,000,000 Da (FLOPAAM 3330) was provided by SNF. The degree of hydrolysis was 25-30% as reported by the manufacturer. An aqueous solution of HPAM in deionized water with concentration of $c_{HPAM}$ = 0.1 wt % was prepared. Rheological properties of the HPAM solution was measured using an ARES rheometer from Rheometric Scientific equipped with Couette geometry (inner diameter of 32 mm and outer diameter of 34 mm). We measured the elastic ($G'(\omega)$) and loss ($G''(\omega)$) moduli of the HPAM solution as a function of frequency (ω = 0.01-100 rad/sec) in the linear

viscoelastic regime, and calculated the complex viscosity as $\eta^*(\omega) = [G'^2(\omega) + G''^2(\omega)]^{1/2}/\omega$ (Figure 3.1).

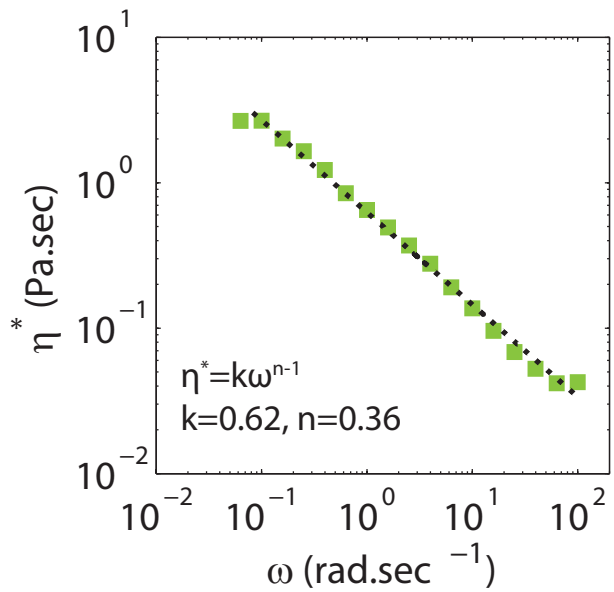


**Figure 3.1** Complex viscosity $\eta^*$ as a function of angular frequency $\omega$ of hydrolyzed polyacrylamide solution at concentration of 0.1 w/w%. Dashed line represent fit to a power law function.

We also prepared a glycerol/water mixture at a concentration of 90 wt % of glycerol (G90) to measure the diffusional dynamics at a comparable value of the local viscosity. Polystyrene nanoparticles were added to the HPAM solution, the G90 solution, and the deionized water at a concentration of $2 \times 10^{-3}$ wt %. The nanoparticle-solution dispersions were then tumbled on a roll mill for 6 – 24 hr to ensure that particles and solutions were uniformly dispersed.

### 3.2.2 Fabrication of porous media

We purchased square cross-section borosilicate capillary cells with inner side length of 0.7 mm, wall thickness of 0.14 mm, and length of 5 cm from VitroCom, and

borosilicate glass microspheres with diameter of 5.4 ± 0.3 μm and 10.0 ± 1.0 μm and soda lime glass microspheres with diameter of 30.1 ± 1.1 μm from Thermo-Scientific. We filled the square capillary with mono-dispersed glass particles to fabricate a 3D porous medium with length of 5 mm. We then lightly sintered the glass particles to permanently fix them in the squared channel. Table 3.1 briefly describes the sintering protocol for two different materials of glass beads.

**Table 3.1** Glass bead properties and sintering protocol for borosilicate and soda lime glass beads.

| Material | Annealing Point (°C) | Softening point (°C) | Sintering temperature (°C) | Sintering period (min) |
|---|---|---|---|---|
| Borosilicate | 560 | 821 | 810 | 5 |
| Soda Lime | 514 | 726 | 680 | 15 |

### 3.2.3 Characterization of pore and throat size of porous media

We visualized the bed structure by imbibing each bed with a solution of rhodamine-B (Wako Pure Chemical Industries, Ltd.) in a mixture of carbon disulfide (n = 1.63) and ethanol (n = 1.36). The amount of each mixture component was selected to match the refractive index of soda lime (n = 1.52) or borosilicate (n = 1.56) glass beads. Confocal micrographs of beds with bead diameters of 5.4 μm, 10 μm, and 30 μm reveal a connected pore network (Figure 3.2a–c). We acquired 25–30 2-D images at different locations in the beds and subsequently binarized them to identify pores and bed particles.

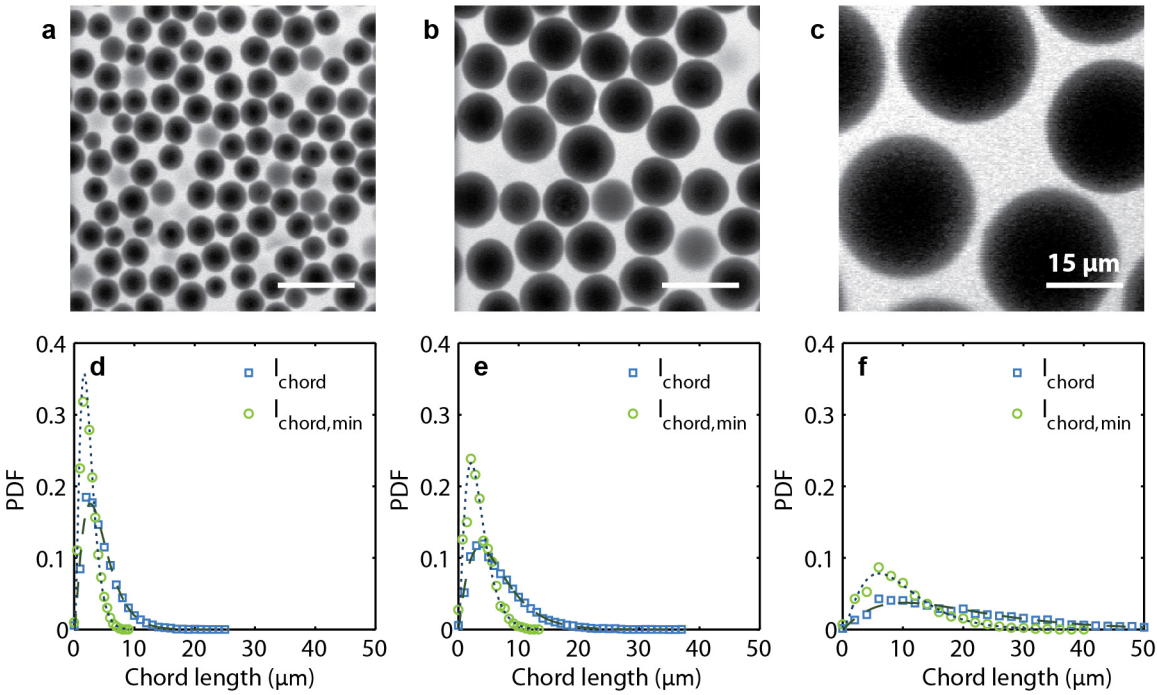


**Figure 3.2** Characterization of the porous media. (a–c) Confocal images of porous media with bead diameters of (a) 5.4 µm, (b) 10 µm, and (c) 30 µm. (d–f) Probability distributions of the chord length and the minimum chord length for porous media with bead diameters of (d) 5.4 µm, (e) 10 µm, and (f) 30 µm. Dashed lines represent fits to a Gamma distribution function (eq 3–1).

To characterize the bed structure, we measured the pore size and confinement length from the binarized confocal micrographs of the beds. First, 5,000 points were randomly selected inside the pore space in each binarized image. Eight vectors at each point were created with equal spacing in the angular direction and expanded in both negative and positive directions until they met the edges of the glass beads. The chord length was calculated as the sum values of negative and positive vectors for each point and angular direction. The pore size was taken to be the average chord length. The minimum chord length was also calculated as the minimum value of chord lengths at each point among all

the angular directions.[183] The confinement length was taken to be the average minimum chord length.

Figure 3.2d–f shows the probability distribution functions (PDFs) of the chord length and the minimum chord length in porous media with bead diameters of 5.4 μm, 10 μm, and 30 μm. The distributions are best fit to a gamma function,

$$G(\mathrm{l}_{\mathrm{chord}}) = \frac{1}{b^{a}\Gamma(a)} {l_{\mathrm{chord}}}^{a-1} \exp\left(-\frac{l_{\mathrm{chord}}}{b}\right), \qquad 3\text{–}1$$

where $l_{\mathrm{chord}}$ is the chord length, $G(l_{\mathrm{chord}})$ is the probability distribution of the chord length, and $a$ and $b$ are fitting parameters. Table 3.2 also shows the average porosity, pore size (chord length), and confinement length (minimum chord length) of the porous media with different bead diameters. The average bed porosity $\varphi$ is about 35% and is roughly constant across the different porous beds studied. The average pore size $d_{\mathrm{pore}}$ varies between 4.4 ± 0.8 and 14.7 ± 2.6 μm and the confinement length $l_c$ varies between 2.7 ± 0.7 and 8 ± 1.1 μm.

**Table 3.2** Average porosity, pore size (chord length), and confinement length (minimum chord length) of the porous media with bead diameters of 5.4 μm, 10 μm, and 30 μm. the error bar is the standard deviation of measurements at 25-30 locations.

| **Bead diameter (μm)** | **Porosity** | $d_{pore} = \langle \boldsymbol{l_{chord}} \rangle$ **(μm)** | $l_c = \langle \boldsymbol{l_{chord,min}} \rangle$ **(μm)** |
|---|---|---|---|
| 5.4 | 0.36 ± 0.07 | 4.4 ± 0.8 | 2.7 ± 0.7 |
| 10 | 0.34 ± 0.06 | 6.4 ± 1.1 | 3.7 ± 1.0 |
| 30 | 0.34 ± 0.06 | 14.7 ± 2.6 | 8.0 ± 1.1 |

### 3.2.4 Imaging of nanoparticles diffusing through porous media

We imaged the nanoparticles as they diffused in the different fluids using a SP8 Leica inverted confocal microscope equipped with a 40× immersion oil lens with numerical aperture (NA) of 1.30. We acquired movies at 2 and 10 frames per second (fps) for nanoparticles diffusing in HPAM and glycerol/water and at 10 and 40 fps for nanoparticles diffusing in water. The image pixel size was 0.284 μm/pix and the image size was 145.31 × 145.31 $\mu m^2$. We acquired twenty movies of each sample at different locations to increase the total number of observed particles. The total number of particles per sample varied between 100 – 1000.

### 3.2.5 Tracking of nanoparticles through porous media

A single-particle tracking algorithm[121] was applied to locate and track the nanoparticles over time with spatial resolution of $\varepsilon = 45$ nm. Particle trajectories were then used to calculate the time-dependent displacement and the ensemble-averaged mean-square displacement (MSD) of the particles. Mean-square displacements are reported only when the MSD exceeded $2\varepsilon^2$, which corresponded to the minimum displacement that could be resolved by the tracking algorithm. Particles that were completely immobile (defined as a maximum displacement of less than 2 pixels, or 0.56 μm) over the duration of the experiment were excluded from the data analysis.

## 3.3 Results and discussion

We use confocal microscopy to investigate the competing effects of geometrical confinement and solution viscoelasticity on diffusive mobility of 400 nm nanoparticles. First, we examined the effects of geometrical confinement within packed beds on particle mobility in Newtonian solutions. The MSD of nanoparticles in the glycerol/water mixture is Fickian diffusive at all accessible lag times and decreases as the particles are increasingly confined within the porous beds, as shown in Figure 3.3. Even on the longest time scales accessible in the experiment, the average particle displacements are significantly smaller than the average confinement length, reported in Table 3.3.

**Table 3.3** Diffusion time required for particles in the center of a pore to encounter the bead surfaces, calculated using the confinement length and the diffusion coefficient of particles in free solution.

| **Bead diameter (μm)** | $t_{\text{diff}} = l_c^{\,2}/2D_0$ **(sec)** | | |
|---|---|---|---|
| | **Water** | **G90** | **HPAM** |
| 5.4 | 3 | 353 | 1041 |
| 10 | 6 | 687 | 2028 |
| 30 | 30 | 3153 | 9303 |

This comparison suggests that a particle located near the center of a pore will not, on average, reach the edge of the pore; nonetheless, slowing of the MSD with increasing confinement suggests that the pore geometry affects the diffusive dynamics through hydrodynamic interactions.

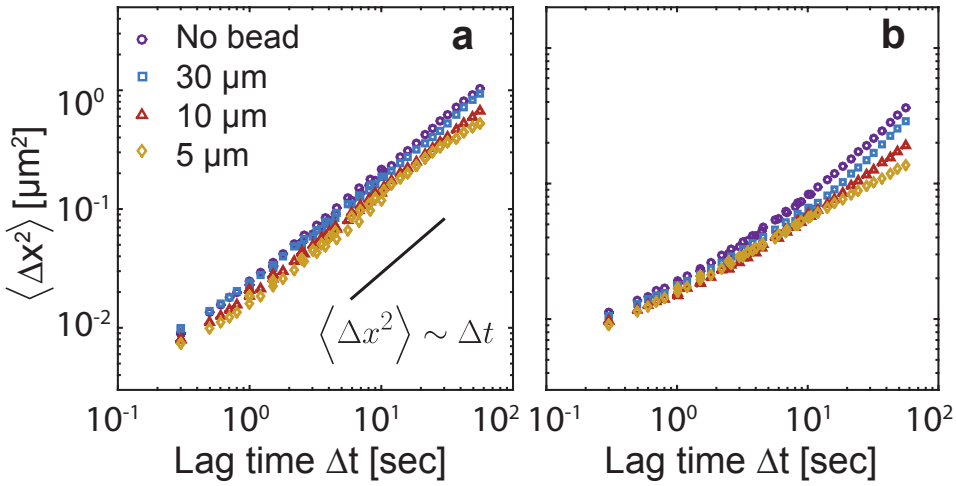


**Figure 3.3** Mean square displacement of nanoparticles as a function of lag time in (a) glycerol/water and (b) HPAM. Symbols represent different media: free diffusion in solution (purple circle), confined diffusion in porous media with bead diameter of 30 μm (blue square), 10 μm (red triangle), or 5 μm (yellow diamond).

By contrast, in the same porous medium nanoparticles in water exhibit subdiffusive mobility at long time scales or when the particles are highly confined (Figure 3.4). The transition to subdiffusive behavior occurs approximately when particle displacements are comparable with average confinement length (Table 3.3). These observations suggest that mobility of nanoparticles in Newtonian solutions that are confined by disordered static obstacles depends on the geometric structure of the pores through hydrodynamic interactions between particles and the surrounding media.

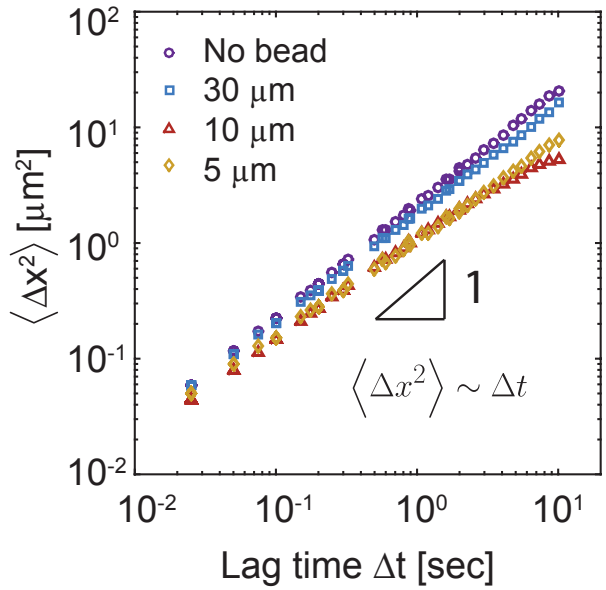


**Figure 3.4** Mean square displacement of nanoparticles as a function of lag time in water. Symbols represent different media: free diffusion in solution (purple circle), confined diffusion in porous media with bead diameter of 30 μm (blue square), 10 μm (red triangle), or 5 μm (yellow diamond).

In the non-Newtonian semidilute HPAM solution, nanoparticles exhibit subdiffusive dynamics on short time scales; this result is consistent with our previous studies.[35,184] The long-time dynamics, however, depend on the extent of confinement within the bed. As in Newtonian solutions, mobility decreases with increasing bed particle size (i.e., with increasing confinement). The long-time mobility in the least confined bed ($d_b$ = 30 μm) approaches Fickian dynamics as the lag time increases. In highly confined beds, however, the dynamics are not completely Fickian even at the longest time scales accessible in these experiments. In these crowded environments, the motion of nanoparticles is highly constrained and is controlled by coupling between dynamics of polymer chains and nanoparticles[184] as well as by geometric constraints imposed by stationary obstacles.

To quantify changes in particle dynamics as a function of geometrical confinement and the solution viscoelasticity, we calculate two parameters from the mean-square displacements. First, from the slope of the long-time MSD displacement, we calculate long time diffusivity $D$ using $\langle \Delta x^2(\Delta t) \rangle = 2D\Delta t$, where $\Delta x$ is the particle displacement at a lag time of $\Delta t$ and the brackets denote time and ensemble averages. Here the long time limit is defined as time scales that are at least one decade longer than the time scale characterizing the crossover from subdiffusive to diffusive dynamics in the HPAM solution, [$\tau_{crossover} \approx 4sec$, $\tau_{longtime} \approx 40sec$]. We normalize the effective long time diffusion coefficients of particles $D$ by the free diffusion coefficients in bulk solutions $D_0$ and examine how the mobility changes as a function of the dimensionless confinement length $\xi = d_{NP}/l_c$. The relative long-time diffusivity $D/D_0$ decreases with increasing confinement parameter but does not depend on fluid characteristics, as shown in Figure 3.5a; the collapse of the data supports the choice of the dimensionless length scale. Decreases in the long-time diffusivity with increasing confinement were earlier reported in structured[43] or unstructured[45,185] porous media. The decrease that we report here, however, [$D/D_0 \approx 0.5 - 0.65$ at $\xi \approx 0.15$], is more pronounced that in earlier experiments in structured porous media; there the diffusivity decreased by ~10% ($D/D_0 \approx 0.9$) at $\xi \approx 0.15$.[43]

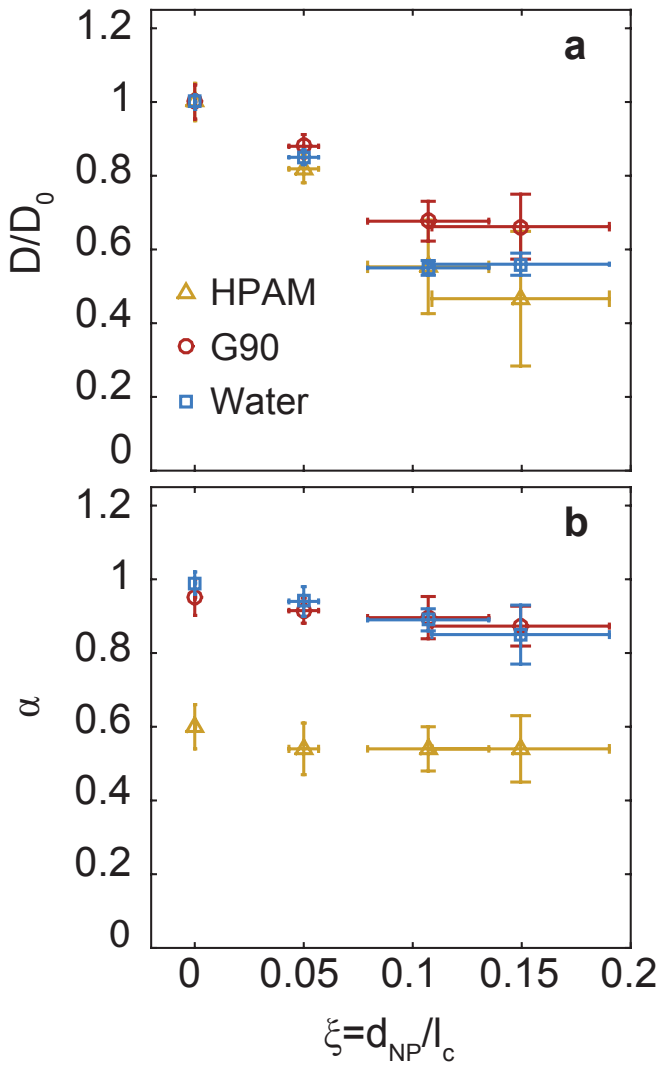


**Figure 3.5** (a) Normalized effective diffusivity and (b) subdiffusive exponent as a function of the normalized confinement length $\xi$ measured for nanoparticles diffusing in different solutions. Symbols represent nanoparticle diffusion in HPAM (gold triangle), glycerol/water (red circle), and water (blue square).

The relative diffusivity of tracer particles was also predicted $[D/D_0 \approx \frac{1}{\varphi}\frac{1+2(1-\varphi)-2\varphi\zeta_2}{\varphi-2\varphi\zeta_2}]$[186] to be slightly faster ($D/D_0 \approx 0.7$) in random packing of spheres with porosity of $\varphi \approx 0.37$ when hydrodynamic interactions were neglected,

where $\zeta_2$ is three-point microstructural parameter which determines properties of heterogeneities media .[185] To account for steric and hydrodynamic effects[187] on diffusivity, analytical models predict hindrance factor in unstructured porous media consisting of arrays of cylindrical[188,189] or slit[190] pores. These models assume that interactions between particles are negligible, that the background solution can be treated as a dilute continuum, and that the diffusion time is long enough for particles to diffuse throughout the the cross-section of the pore. The models make two different assumptions about the drag force: (i) in the centerline approximation,[191] the drag force is assumed to be constant over the cross-section and is taken to be the force at the center of the cylinder or slit; (ii) in cross-section averaging,[192] the drag force is taken to be a function of the particle distance from the wall. Table 3.4 summarizes the models ($\xi = d_{NP}/l_c$). For confinement parameters of $\xi = 0.15 - 0.05$ (corresponding to those in our experiments), the relative diffusivities predicted by different models on average range from $D/D_0 \approx 0.6 - 0.8$ for $\xi = 0.15 - 0.05$, which is in reasonable agreement with our results. Moreover, particles diffusing in a disordered polymeric structure with confinement lengths in the range of $\xi \approx 0.02 - 0.10$ and a porosity of $\varphi \approx 0.52$ exhibited relative diffusivities of $D/D_0 \approx 0.4 - 0.5$[45]. These comparisons suggest that hydrodynamic interactions as well as variations in pore arrangement and structure control the diffusive dynamics within disordered porous media.

**Table 3.4** predicted models for relative confined diffusivity in cylindrical and slit pores

| Pore type | Model | Category | Validity |
|---|---|---|---|
| Cylindrical | $D/D_0 = (1-\xi)^2(1 - 2.104\xi + 2.09\xi^3 - 0.95\xi^5)$[193,194] | Center line approximation | $\xi < 0.4$ |
| Cylindrical | $D/D_0 = 1 + \frac{9}{8}\xi \ln \xi - 1.539\xi + 1.2\xi^2 + O(\xi^2)$[195,196] | Cross-section averaging | $\xi \to 0$ |
| Cylindrical | $D/D_0 = 1 + \frac{9}{8}\xi \ln \xi - 1.539\xi + 0.528155\xi^2 + 1.915213\xi^3 - 2.81903\xi^4 + 0.270788\xi^5 + 1.10115\xi^6 + 0.435933\xi^7$[197,198] | Cross-section averaging | $0 \leq \xi \leq 0.95$ |
| Slit | $D/D_0 = (1-\xi)(1 - 1.004\xi + 0.418\xi^3 + 0.21\xi^4 - 0.169\xi^5 + O(\xi^6)$[191] | Center line approximation | $\xi < 0.5$ |
| Slit | $D/D_0 = 1 + \frac{9}{16}\xi \ln \xi - 1.9358\xi + 0.4285\xi^3 - 0.3192\xi^4 + 0.08428\xi^5$[199] | Cross-section averaging | $\xi < 0.33$ |

Second, from the scaling behavior of the MSD on short time scales, we calculate the short time subdiffusive exponent $\alpha$ from $\langle \Delta x^2(\Delta t) \rangle = \beta \Delta t^\alpha$. The subdiffusive exponent depends only weakly on the confinement parameter in both Newtonian and non-Newtonian solutions, as shown in Figure 3.5b. This observation indicates that short time mobility of nanoparticles is not affected by geometric confinement, as the particles on average do not encounter the fixed obstacles at very short times. The subdiffusive exponents in HPAM, however, are notably smaller than those measured in Newtonian solutions within the same porous medium. When the dynamics of particles and polymers

are fully coupled, the subdiffusive exponent is predicted to be 0.5 from the Rouse dynamics of the polymers;[34] in earlier measurements we found that subdiffusive exponent varies between 0.5 – 1 depending on polymer concentration and particle size, indicating intermediate coupling of particles dynamics to polymer fluctuations.[184]

To gain further insight into the processes controlling the confined dynamics of nanoparticles in the different solutions, we analyze the distribution of one-dimensional displacements $G_s(\Delta x, \Delta t)$ at several lag times for nanoparticles in varying solutions and varying pore sizes. In free diffusion, the distribution of particle displacements is Gaussian in both Newtonian (Figure 3.6a,b) and non-Newtonian HPAM solutions (Figure 3.6c,d). As the particles are increasingly confined within the pores, the diffusive mobility of nanoparticles increasingly deviates from Gaussian dynamics. The distributions of particle displacements cannot be described by a single function in the highly confined bed. Instead, we fit the distributions to sum of a Gaussian function, to capture the center of the distribution, and a stretched exponential function, to model the tail, as[43]

$$G_s(\Delta x, \Delta t) = a_1 exp\left(-\left(\frac{\Delta x}{\delta}\right)^2\right) + a_2 exp\left(-\left|\frac{\Delta x}{\gamma(\Delta t)}\right|^s\right), \qquad 3\text{-}2$$

where $a_1$ and $a_2$ are pre-exponential factors, $\delta$ and $\gamma(\Delta t)$ are the decay lengths for the Gaussian and the stretched exponential models, respectively, and $s$ is the stretching exponent. We hypothesize that the first term captures the caged states, while the second term accounts the untrapped motions.

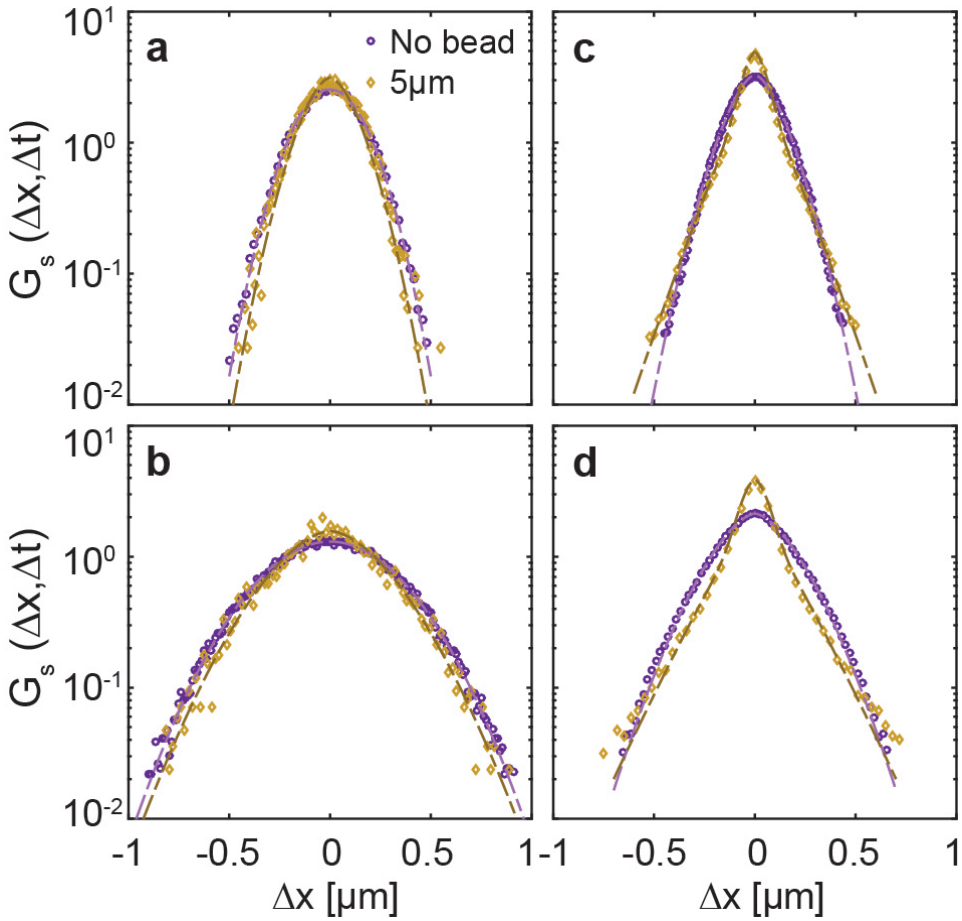


**Figure 3.6** Probability density function of particle displacements at lag times of 1 sec (top row) and 5 sec (bottom row) for nanoparticles in (a and b) glycerol/water and (c and d) HPAM solution. Symbols represent different media: free diffusion in solution (purple circle) and confined diffusion in porous media with bead diameter of 5 μm (yellow diamond).

In initial fitting, we found that the stretching exponent $s$ and the decay length of the Gaussian model $\delta$ were nearly independent of lag time for each solution and bed configuration. We therefore used the average values of $\langle s \rangle$ and $\langle \delta \rangle$ to reduce the number of fitting parameters. For nanoparticles diffusing in Newtonian solutions within confined bed $a_1 \ll a_2$, indicating absence of any long trapped state in particle displacements within the Newtonian solution. For nanoparticles diffusing in HPAM within porous

media, however, $a_1$ is not negligible ($a_1/a_2 \approx 0.1 - 2$), suggesting that a second mechanism affects the diffusion of nanoparticles in the HPAM solution through the porous medium.

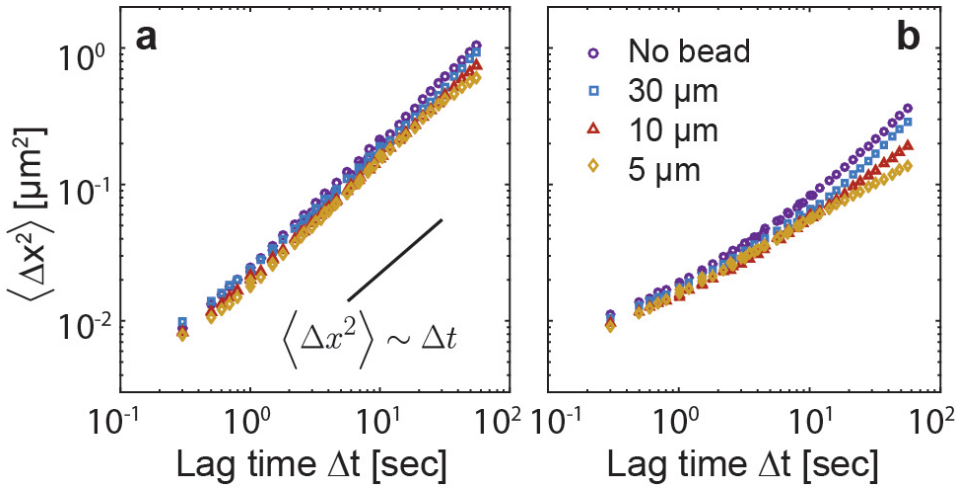


**Figure 3.7** Decay length as a function of lag time for nanoparticles in (a) glycerol/water and (b) HPAM. Symbols represent different media: free diffusion in solution (purple circle); confined diffusion in porous media with bead diameter of 30 μm (blue square), 10 μm (red triangle), or 5 μm (yellow diamond).

The decay length $\gamma$ of the stretched exponential function describes the dynamics of mobile states. For freely-diffusing particles in Newtonian solutions, the decay length increases with square root of the lag time $\gamma(\Delta t) \sim \sqrt{\Delta t}$ (Figure 3.7). Similarly, on long time scales the decay length of freely-diffusing particles in non-Newtonian solutions also grows as the square root of time, i.e. $\gamma(\Delta t) \sim \sqrt{\Delta t}$. For particles in stronger confinements, however, the decay length grows more slowly with the lag time in both Newtonian and non-Newtonian solutions. This slow growth is different from what has been observed for diffusion of particles in ordered porous media,[120] in hard sphere colloidal suspensions,[33] or in entangled F-actin networks[38]. In these examples, particles diffusing in crowded

environments exhibited non-Gaussian but still Fickian dynamical behavior, which was attributed to local Brownian dynamics within a slowly-relaxing heterogeneous medium.[33,38,39]

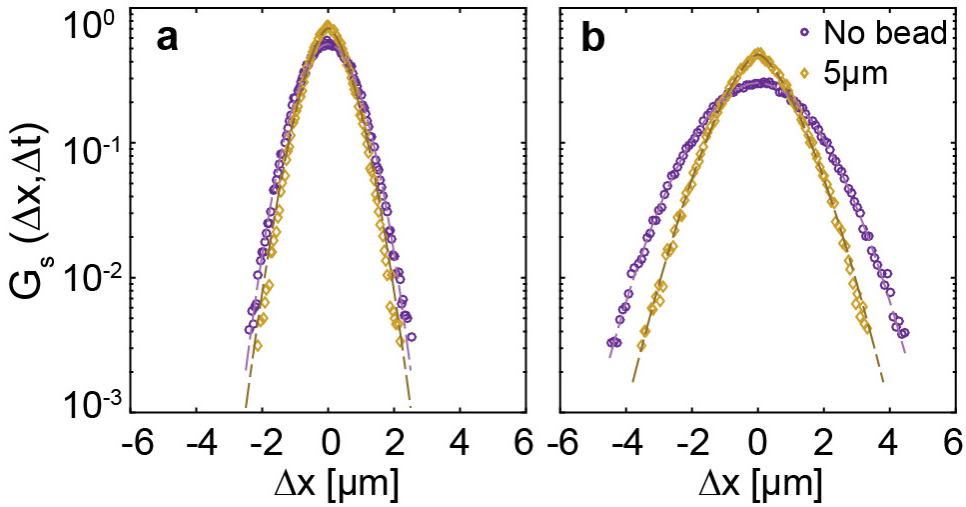


**Figure 3.8** Probability density function of particle displacements at lag times of (a) 0.25 sec and (b) 1 sec for nanoparticles in water. Symbols represent different media: free diffusion in solution (purple circle) and confined diffusion in porous media with bead diameter of 5 μm (yellow diamond).

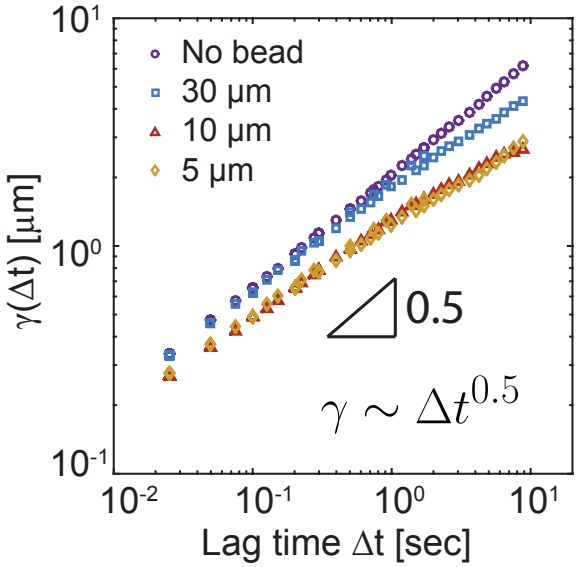


**Figure 3.9** Decay length as a function of lag time for nanoparticles in water. Symbols represent different media: free diffusion in solution (purple circle); confined diffusion in porous media with bead diameter of 30 μm (blue square), 10 μm (red triangle), or 5 μm (yellow diamond).

In our experiments, however, the diffusive dynamics depend on both the pore structure and the time scale. As one extreme example, the local diffusive dynamics of particles in water (Figure 3.4, Figure 3.8, and Figure 3.9) change as the pore size and diffusion length scale become comparable. Local diffusive dynamics is non-Fickian even in very small pores.

To gain insight into the origin of these dynamics, we examine the trajectories of particles diffusing freely and confined by porous media and/or polymers in solution. In Newtonian glycerol/water solutions, particle trajectories show random diffusion. Particles undergo larger displacements over successive time steps ($\Delta t$ = 0.5 sec) when freely diffusing than when diffusing in a highly confined porous medium (Figure 3.10 a,b). Particles in the glycerol/water solution within the porous medium are slightly hindered by geometric confinement, but remain mobile throughout (Figure 3.10b). This result is consistent with earlier measurements of confined diffusion near walls[42,200] and in pores.[31,201,202] In sharp contrast, the trajectories of unconfined and confined nanoparticles diffusing in HPAM solutions exhibit qualitatively different features (Figure 3.10c,d). Unconfined nanoparticles in HPAM exhibit diffusive trajectories, and the displacements over time do not exhibit long waiting times or jumps between frames. When highly confined by a porous medium, however, the trajectories of nanoparticles in HPAM reveal long intervals of near-zero displacements that are separated by random motions. Here the considerable dwell time between random motions apparently arises due to temporary adsorption of the particles onto the surface of the glass beads (Figure 3.10d).

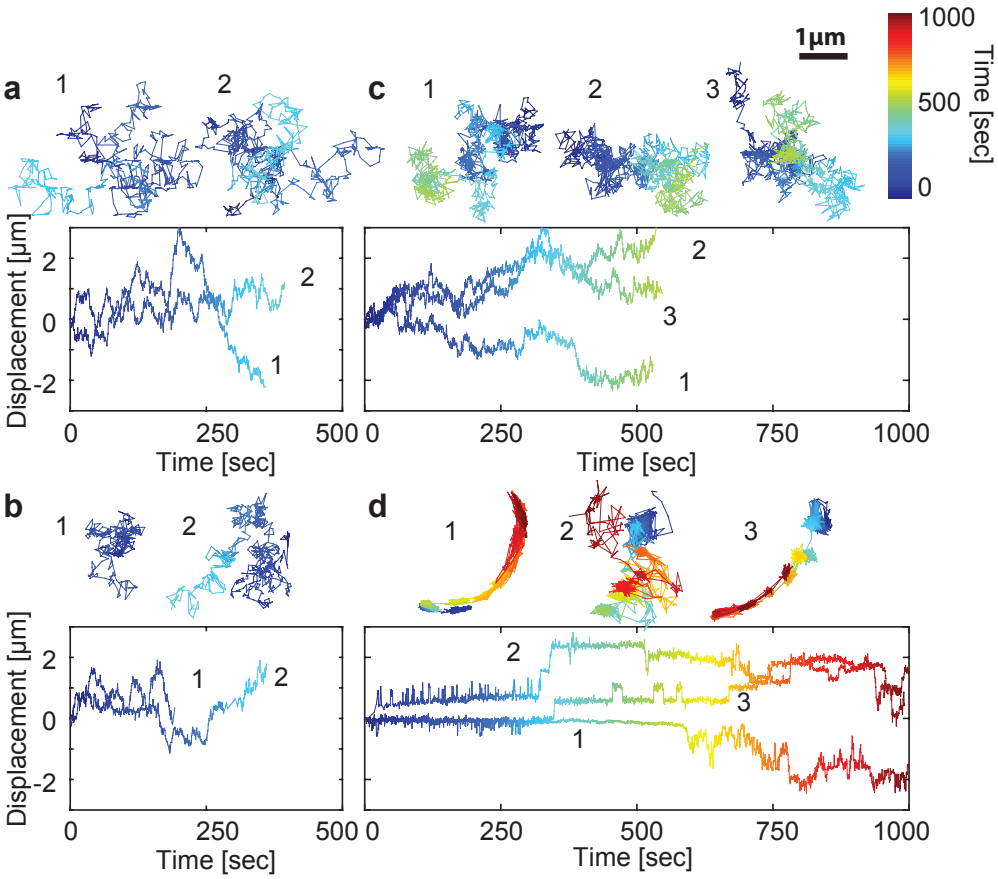


**Figure 3.10** Representative trajectories and displacement as a function of time for nanoparticles diffusing in (a and b) glycerol/water and (c and d) HPAM. The top row [(a) and (c)] show free diffusion in solution and the bottom row [(b) and (d)] shows confined diffusion in porous media with a bead diameter of 5 µm.

Similar trajectories featuring long-duration immobilizations interrupted by intermittent jumps were observed for polymer chains diffusing near a surface[47–49]. Polymer chains in these experiments could loosely bind to the surface but frequently desorbed, as indicated by a rapid jump in position. After desorbing, chains could either diffuse back to the bulk or readsorb onto the surface (either permanently or transiently). We speculate that the tendency for particles in HPAM to become temporarily immobilized when diffusing in porous media is mediated by the presence of the polymer

molecules. This idea is consistent with the increasingly pronounced peak in the distribution of particle displacements at longer lag times. These experiments reveal that the local mobility of nanoparticles in non-Newtonian solutions is significantly affected both by the presence of macromolecules and by confinement.

To understand the origins of the adsorption, we consider the total interactions between nanoparticles and glass beads as sum of electrostatic interaction $\Delta G^{EL}$, Lifshitz-van der Waals interaction $\Delta G^{LW}$, and polymer mediated deletion interaction $\Delta G^{DEP}$:

$$\Delta G^{total} = \Delta G^{EL} + \Delta G^{LW} + \Delta G^{DEP}. \qquad 3\text{-}3$$

The contribution of electrostatic and Lifshitz-van der Waals interactions is calculated using DLVO theory:[203,204]

$$\Delta G^{EL} = \pi\varepsilon\varepsilon_0 R\left[2\varphi_{NP}\varphi_{GB}\ln\left(\frac{1+\exp(-\kappa h)}{1-\exp(-\kappa h)}\right) + ({\varphi_{NP}}^2 + {\varphi_{GB}}^2)\ln(1-\exp(-2\kappa h))\right] \text{ and} \qquad 3\text{-}4$$

$$\Delta G^{LW} = 2\pi R h_0 \Delta G_{d_0}^{LW}\frac{h_0}{h}, \qquad 3\text{-}5$$

where $\varepsilon_0$ is permittivity of the free space ($8.85\times10^{-12}\mathrm{s}^4\mathrm{A}^2\mathrm{m}^{-3}\mathrm{kg}^{-1}$), $\varepsilon$ is the relative permittivity of the medium, which is $\varepsilon = 78$ for water, $R$ is nanoparticle radius, $h$ is particle-wall distance, and $h_0$ is the minimum equilibrium distance. $\varphi_{NP}$ and $\varphi_{GB}$ are the surface potential of the nanoparticles and the glass beads respectively, which are related to zeta potential. $\kappa$ is inverse of Debye length $\kappa = (4\pi l_B c z^2)^{1/2}$, where $l_B = 0.7$ nm is Bjerrum length in water, $c$ is the ion concentration of polyelectrolytes, and $z$ is ion charges.[232] $\Delta G_{d_0}^{LW}$ is calculated as:

$$\Delta G_{d_0}^{LW} = -2\left(\sqrt{\gamma_{NP}^{LW}} - \sqrt{\gamma_m^{LW}}\right)\left(\sqrt{\gamma_{GB}^{LW}} - \sqrt{\gamma_m^{LW}}\right), \quad 3\text{-}6$$

where $\gamma_{NP}^{LW}$, $\gamma_m^{LW}$, and $\gamma_{GB}^{LW}$ are surface energy of nanoparticles, medium (water) and glass beads, respectively.

When the distance between particles and a nearby confining surface (i.e. the glass beads) is less than the effective diameter of the polymer chains, the region between particles and walls is depleted from polymer molecules. Depletion of polymer molecules inside such area creates an effective osmotic pressure, resulting in depletion attraction between particles and walls.[205] Depletion interaction between a sphere and a plate induced by polymer solution in semi-dilute regime is calculated using the overlapping volume of the depletion layers:[206,207]

$$\frac{\Gamma(h)-\Gamma(\infty)}{n_p} = \begin{cases} \frac{4}{3}\pi(R+\Delta_s)^3 & h < \Delta_w - 2R - \Delta_s \\ \frac{1}{3}\pi(\Delta_s + \Delta_w - h)^2(3R + 2\Delta_s - \Delta_w + h) & \Delta_w - 2R - \Delta_s < h < \Delta_w + \Delta_s, \\ 0 & h < \Delta_w + \Delta_s \end{cases} \quad 3\text{-}7$$

where $\Delta_s$ is depletion layer thickness around the sphere, $\Delta_w$ is the depletion layer thickness near the wall. In semidilute regime the depletion thicknesses are dependent on polymer correlation length. The osmotic pressure in semidilute solution is calculated as $\frac{\Pi}{k_B T} = \frac{1}{\xi^3} = \frac{1}{71.8^3} = 2.7\times10^{-6}\text{nm}^{-3}$. The potential interaction $\Delta G^{DEP}$ between a particle and a wall is calculated as:

$$\Delta G^{DEP} = -\int_0^{n_p} dn'_p \left(\frac{\partial \Pi}{\partial n'_p}\right) \Gamma(h) - \Gamma(\infty). \qquad 3\text{-}8$$

Normalized depletion thickness around a sphere in semidilute solution is $\frac{\Delta_s}{R} = \left[1 + 3.213\frac{\xi}{R} + 2.607\left(\frac{\xi}{R}\right)^2 - 0.120\left(\frac{\xi}{R}\right)^3\right]^{1/3} - 1 \approx 0.354$, which results in $\Delta_s = 70.8\,\text{nm}$. Also the depletion thickness near the wall in semidilute solution is $\Delta_w = 1.071\xi = 76.8\,\text{nm}$. The electrostatic, Lifshitz-van der Waals, depletion, and total interactions between a nanoparticle and a glass bead are shown in Figure 3.11. Electrostatic repulsion prevents permanent adsorption of nanoparticles onto the surface of glass beads, however depletion interactions mediate particle-surface attractions at larger distances.

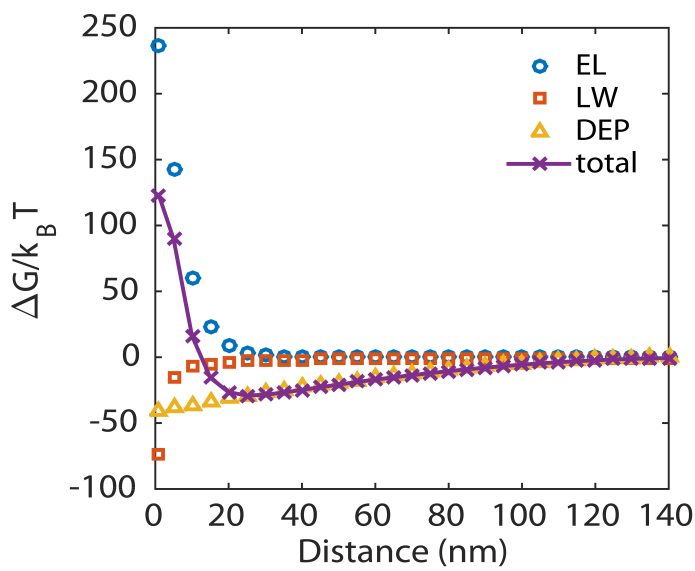


**Figure 3.11** Electrostatic (blue circle), Lifshitz-van der Waals (red square), depletion (gold triangle), and total (purple line) interactions between a nanoparticle and a glass bead.

To separate effects of confinement on particle dynamics from those induced by the polymers, we first define an absolute displacement of $r = 0.045\ \mu$m as the threshold of particle immobility, corresponding to the resolution of the tracking algorithm under these imaging conditions. Using this immobility threshold, we binarize the particle displacements over consecutive time steps: displacements greater than this threshold are labeled "1" and those less than this threshold are labeled "0." This process converts trajectories into strings of ones and zeroes. We then calculate the distribution of the immobile (consecutive zeros, $\tau_{\mathrm{im}}$) and mobile (consecutive ones, $\tau_{\mathrm{mob}}$) steps for each trajectory. For nanoparticles in glycerol/water the ensemble-aggregated distributions of mobile and immobile steps each follow an exponential decay independent of the confinement imparted by the porous structure (Figure 3.12a,b).

The distribution of mobile steps in non-Newtonian HPAM also follows an exponential decay, independent of confinement (Figure 3.12c). The distribution of immobile times, however, deviates from an exponential decay when the nanoparticles are confined within a porous medium; instead, this distribution exhibits an extended power-law tail with an exponent of ~3 (Figure 3.12d). A power law distribution was also observed in the waiting time distribution of polymer molecules diffusing near a surface, with an exponent between 1.6 and 2.5.[47,48] In this scenario the power-law distributions were attributed to very heterogeneous surface diffusion;[47,48,208] in turn, increases in the heterogeneity of surface diffusion broadened the spectrum of binding energies and hence led to a smaller power law exponent.[32] By analogy, we suggest that the temporarily

immobilized particles in our experiments may also experience a spectrum of binding energies, corresponding to different environments within our packed beds.

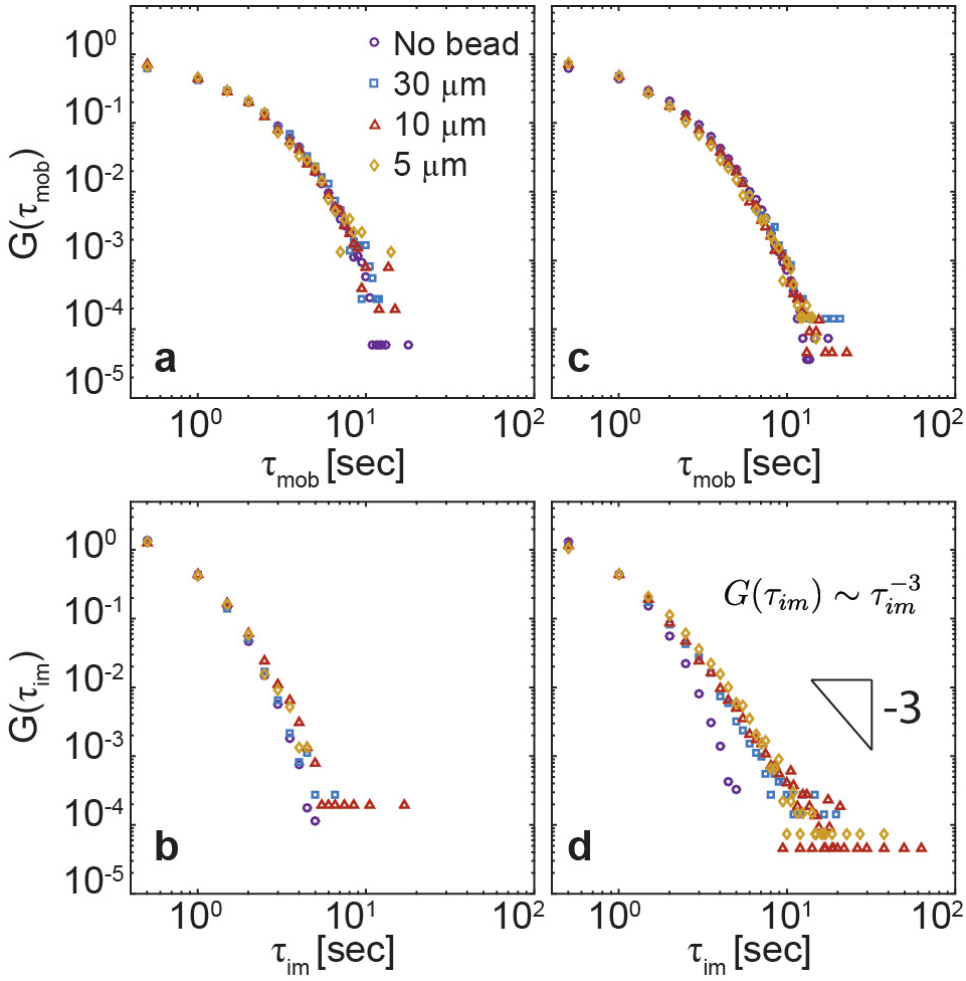


**Figure 3.12** Probability density function of mobile (top row) and immobile (bottom row) times for nanoparticles diffusing in (a, b) glycerol/water and (c,d) HPAM. Symbols represent different media: free diffusion in solution (purple circle), confined diffusion in porous media with bead diameter of 30 μm (blue square), 10 μm (red triangle), and 5 μm (yellow diamond).

The power law exponent of nanoparticles diffusing in polymer solutions through packed beds (~3) is greater than previously reported exponents, suggesting that the diffusive dynamics of particles in polymer solution within porous media are less heterogeneous

than those of the polymer molecules diffusing near a surface. Indeed, not all particles encounter the surface over the duration of an experiment and hence the diffusion of particles near a surface may be expected to be less heterogeneous than that of the polymers.

To determine the effects of hydrodynamic screening and temporary adsorption on the confined mobility of nanoparticles, we eliminate immobile steps from particle trajectories. Explicitly, we remove immobile particles if the duration of the immobile step is greater than three consecutive time steps (1.5 sec). When the immobile steps are removed, the MSD of mobile particles in confined media approaches that of free diffusion in both Newtonian and non-Newtonian solutions (Figure 3.13). Furthermore, the relative diffusion coefficient ($D/D_0$) extracted from the long-time Fickian diffusion is nearly independent of the confinement parameter (Figure 3.13, inset).

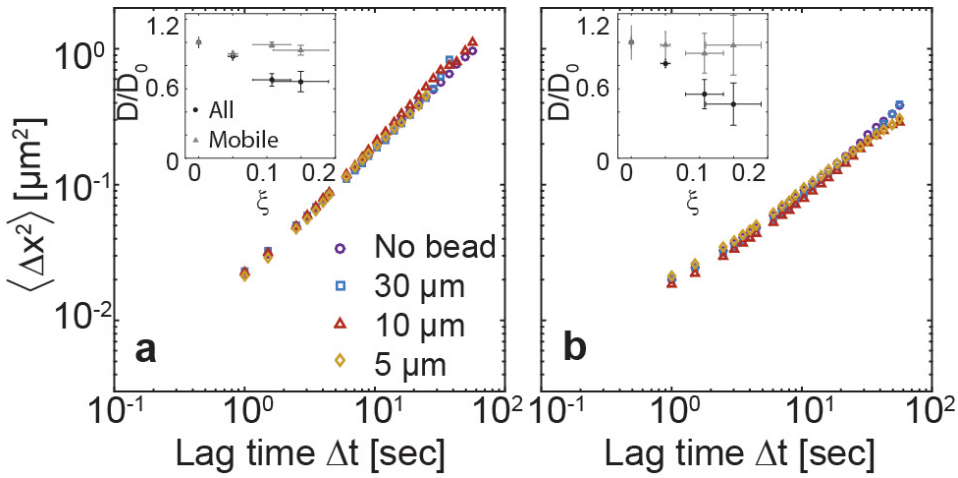


**Figure 3.13** Mean square displacement of mobile particles as a function of lag time in (a) glycerol/water mixture (90 w/w%) and (b) HPAM solution (0.1 w/w%). The inset in each panel shows long time diffusion coefficient as a function of confinement length for all time step (black circle) and mobile time steps (gray triangle).

The MSD of mobile particles in glycerol/water solution is almost identical in for the different porous media. This result suggests that hydrodynamic interactions with nearby surfaces generate the slowing of diffusion in Newtonian glycerol/water. When hydrodynamic interactions are removed, mobility is fully recovered. By contrast, in HPAM solution the diffusion of mobile particles at the smallest porous bed ($d_b = 5\mu$m) is slightly faster than free diffusion on the shortest time scales. This result is consistent with the anomalously large tails in the distribution of displacements of particles in strong confinement (Figure 3c and d). Local inhomogeneities in the concentration of HPAM, whether due to adsorption of polymer molecules onto the surface of glass beads or to hindered transport of the high-molecular-weight polymer into highly confined pores, may generate the anomalous tails and hence the faster-than-expected local diffusion of the particles.

## 3.4 Conclusion

We separate the effects of disordered spatial confinement and solution viscoelasticity on diffusive mobility of nanoparticles. Diffusive mobility decreases as particles in both Newtonian and non-Newtonian solutions are increasingly confined. In both Newtonian and non-Newtonian solutions, hydrodynamic interactions generate slowing of diffusive mobility with increasing confinement by the packed beds. The disordered and heterogeneous geometrical structure of the porous media leads to greater decreases in particle diffusivity compared to that measured in ordered structures with comparable pore size. In the non-Newtonian solution, an additional driving mechanism

related to immobilization of the particles on the bed surface also leads to slowing of diffusion; this immobilization, in turn, arises from temporary adsorption of the particles onto the surface of glass beads. This feature suggests that presence of the long-chain polymer molecules alters the pore scale mobility of the particles due to depletion interactions. Mobility of nanoparticles in HPAM solution through porous media is therefore not only controlled by the hydrodynamic interactions, but also by depletion interaction resulting adsorption-desorption process. Our methods thus allow sensitive tests of different mechanisms slowing diffusion; distinct effects arising from polymers as opposed to confinement.

# Chapter 4

Note: The material in this chapter has been submitted for publication.

## 4.0 Nanoparticle dispersion in disordered porous media through Newtonian and non-Newtonian solutions

Control over transport of nanoparticles in non-Newtonian solutions flowed through highly confined porous media is required to deliver drugs and diagnostics,[209] to safely produce hydrocarbons,[13] and to process polymer nanocomposites.[210,211] Whereas in Newtonian fluids the long-time spreading of particles flowed at high shear rates through a porous medium is controlled by mechanical mixing of the fluid stream,[104,212] the effects of viscoelasticity arising in confined flows of non-Newtonian fluids[115,117,213–217] on microscopic particle flow profiles and on macroscale particle transport remains poorly understood. Here we show across a range of flow rates and packed bed configurations that the long-time transport coefficients of nanoparticles flowed in a Newtonian fluid and in a non-Newtonian shear-thinning polymer solution collapse onto scaling curves, independent of the fluid rheology. Thus non-Newtonian fluid characteristics do not impact nanoparticle dispersion through disordered porous media.

### 4.1 Introduction

In Newtonian fluids flowed through a disordered porous medium, molecular diffusive processes control the long-time (asymptotic) dispersion of tracer particles in both the axial and transvers directions when advection is weak compared to diffusion;

similarly, advective processes due to the stochastic velocity field control dispersion in the opposite limit.[104,212] The disordered structure of the medium generates uniform mixing, enabling the tracers to sample all positions within the bed.[212] The pore-scale velocity profiles reflect the spatial heterogeneity of the medium[109] but do not affect long-time dispersion in the mechanically-mixed regime.[218] The importance of uniform mixing is emphasized through comparisons to structured porous media, in which particles can exhibit deterministic trajectories[219,220] and local coupling between diffusive and advective transport on short time and length scales alters dispersion.[120]

In non-Newtonian fluids additional mechanisms that may affect particle dispersion arise from the interplay of the fluid rheology and spatial confinement within a disordered pore network. The converging-diverging pore structure imposes deformations that typically include both shear and elongational components, thus generating complex flows.[110] When the rate of shear-imposed deformation $\dot{\gamma}$ is less than the characteristic relaxation rate $1/\lambda$ of the fluid, as quantified by the Weissenberg number $Wi = \lambda\dot{\gamma} < 1$, Darcy's law can be used with the time-dependent effective viscosity of the non-Newtonian fluid. At higher shear rates, however, the pressure gradient increases nonlinearly with the flow velocity, with contrasting effects reported for the flow characteristics of non-Newtonian fluids. On one hand, nonlinearities arising in the flow of a non-Newtonian fluid through narrow pores can manifest as elastic instabilities, e.g. around confined cylinders,[115,213] as irreversible nanogel formation,[117,214] or as elastic turbulence;[215–217] here microscale confinement couples to the non-Newtonian fluid response to enhance velocity and stress fluctuations. On the other hand, at sufficiently

high shear rates flow through a porous medium can break the non-Newtonian fluid characteristics of a yield-stress fluid;[118,119] here the deformation imposed by the pore network effectively averages out the non-Newtonian properties of the fluid. Which of these effects governs the dispersion of nanoparticles that are suspended in non-Newtonian shear-thinning fluids and flowed through disordered porous media remains unknown.

## 4.2 Materials and methods

### 4.2.1 Preparation of nanoparticles-solution dispersions

Fluoro-Max dyed red aqueous fluorescent polystyrene nanoparticles of diameter $d_{NP}$ = 400 nm at concentration of 1 wt % were purchased from Thermo Fisher Scientific. Hydrolyzed polyacrylamide (HPAM) polymer of weight- averaged molecular weight (Mw) of 8,000,000 Da (FLOPAAM 3330) was provided by SNF. The degree of hydrolysis was 25-30% as reported by the manufacturer. An aqueous solution of HPAM in deionized water with concentration of $c_{HPAM}$=0.1 wt % was prepared. We also prepared a glycerol/water mixture at concentration 90 wt % of glycerol (G90). Polystyrene nanoparticles were added to HPAM solution, G90 solution, and deionized water at concentration of $2\times10^{-3}$ wt %. The nanoparticle-solution dispersions were then tumbled on a roll mill for 6-24 hours to make homogeneous dispersions.

### 4.2.2 Fabrication and characterization of porous media

Borosilicate capillary cells with square cross-section, inner side length of 0.7 mm, wall thickness of 0.14 mm, and length of 5 cm were purchased from VitroCom. Borosilicate glass microspheres with diameter of 5.4±0.3 μm and 10.0±1.0 μm and soda lime glass microspheres with diameter of 30.1±1.1 μm were purchased from Thermo-Scientific. The square capillary was filled with mono-dispersed glass particles to fabricate a 3D porous medium with length of 5 mm. The glass particles were slightly sintered to remain stationary in the channel. The schematic of flow cell is shown in Figure 4.1.

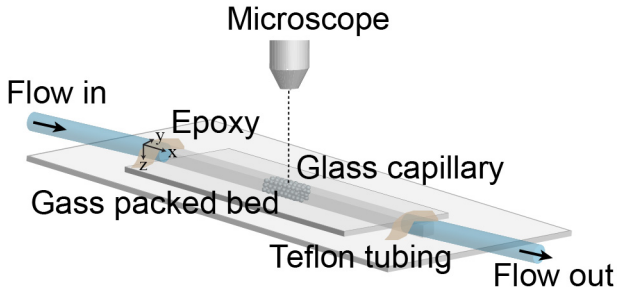


**Figure 4.1** Schematic illustration of the microchannel flow experiments:[221] the microchannel is connected to a syringe pump using PTFE (Teflon) tubing. The schematic is inverted compared to the experimental setup, which is held on an inverted microscope. The packed bed has 5 mm length and porosity of 35%.

To characterize the beds, we acquired two-dimensional images of the beds using confocal microscopy. The beds were previously filled with Rhodamine dye suspended in a matched refractive index solution. Table 4.1 shows average porosity $\varphi$, average pore size $d_{pore}$, and average confinement length $l_c$ of the beds. Both ends of the square capillary were attached to PTFE tubing with inner diameter of 1 mm. A syringe pump working at constant displacement is connected to the tubing to feed the capillary.

### 4.2.3 Characterization of pore and throat size of porous media

To visualize the bed structure, we suspended Rhodamine-B solution in a mixture of carbon disulfide (n=1.63) and ethanol (n=1.36). The amount of each mixture component is selected to match the refractive index of soda lime (n=1.52) or borosilicate (n=1.56) glass beads. Bed structure is characterized as reported in Chapter 3. Table 4.1 shows the average porosity, pore size (chord length), and confinement length (minimum chord length) of the porous media with different bead diameters.

**Table 4.1** Average porosity, pore size (chord length), and confinement length (minimum chord length) of the porous media with bead diameters of 5.4 µm, 10 µm, and 30 µm.

| **Bead diameter (µm)** | **Porosity** | $\langle l_{chord} \rangle$ **(µm)** | $\langle l_{chord,min} \rangle$ **(µm)** |
|---|---|---|---|
| 5.4 | 0.36±0.07 | 4.36±0.83 | 2.68±0.73 |
| 10 | 0.34±0.06 | 6.37±1.14 | 3.74±0.97 |
| 30 | 0.34±0.06 | 14.73±2.60 | 8.01±1.10 |

### 4.2.4 Rheology of hydrolyzed polyacrylamide solution

The viscosity of the HPAM solution was measured using an ARES rheometer equipped with a double Couette geometry (inner diameter of 32 mm and outer diameter of 34 mm). We calculated the complex viscosity $\eta^*(\omega) = [G'^2(\omega) + G''^2(\omega)]^{1/2}/\omega$ as a function of angular frequency as described in Chapter 3. Shear thinning behavior of viscosity is modeled using a power law function as

$$\eta^* = k\omega^{n-1}\,, \qquad 4\text{-}2$$

where $k$= 0.62 and $n$= 0.36 are the fitting parameters. Polymer relaxation time, $\lambda = 15\ sec$, is extracted from the bulk rheology at low frequencies when the viscosity approaches a constant.

### 4.2.5 Imaging of nanoparticles through porous media

Samples were imaged using a SP8 Leica inverted confocal microscope equipped with a 40x immersion oil lens with numerical aperture (NA) of 1.30. We acquired 6000 frames at 110 frames per second (fps) with a pixel size of 0.284 μm and size of 145.31×36.11 $\mu m^2$. We took multiple movies of each sample at nine different x-y locations, but constant z position and varying flow rates (Q= 5, 10, 15, and 20 μl/hr). The x-y locations were kept constant at different flow rates.

### 4.2.6 Tracking of nanoparticles through porous media

Single particle tracking algorithm[121] was applied to locate and track nanoparticles over time. Particle trajectories were then used to calculate the velocity of nanoparticles along and transverse the flow direction.

## 4.3 Dimensionless numbers

In this section we calculate dimensionless numbers that are important in flow through porous media. The Deborah number De, the ratio of polymer relaxation time to the residences time of the nanoparticles and the Weissenberg number Wi, the ratio of the viscous forces to the elastic forces, are specifically defined for flow of elastic fluids through porous media. The Deborah and Weissenberg numbers are calculated as

$$De = \frac{\lambda}{t_{NP}} = \frac{\lambda v_{avg}}{r_b} \; and \qquad 4\text{-}3$$

$$Wi = \lambda\dot{\gamma} = \frac{\lambda v_{avg}}{l_c}, \qquad 4\text{-}4$$

where $\lambda$ is the polymer relaxation time, $t_{NP}$ is the residence time of the nanoparticles, $v_{avg}$ is the average velocity of the nanoparticles, $r_b$ is the characteristic radius of curvature of the streamlines $(d_b/2)$, $\dot{\gamma}$ is the characteristic shear rate, and $l_c$ is the confinement length of the porous media.[115,213,222]

**Table 4.2** De numbers of nanoparticles in HPAM flowed through porous media with bead diameters of 5.4, 10, and 30 µm at flow rates of 5 – 20 µl/hr.

| **Bead size $d_b$ (µm)** | **Flow Rate Q (µm/sec)** | | | |
|---|---|---|---|---|
| | 5 | 10 | 15 | 20 |
| 5.4 | 88.54 | 117.40 | 161.91 | 228.28 |
| 10 | 42.43 | 79.89 | 118.62 | 165.61 |
| 30 | 11.44 | 16.11 | 26.10 | 34.68 |

**Table 4.3** Wi numbers of nanoparticles in HPAM flowed through porous media with bead diameters of 5.4, 10, and 30 µm at flow rates of 5 – 20 µl/hr.

| **Bead size $d_b$ (µm)** | **Flow Rate Q (µm/sec)** | | | |
|---|---|---|---|---|
| | 5 | 10 | 15 | 20 |
| 5.4 | 89.5 | 118.7 | 163.7 | 230.8 |
| 10 | 56.9 | 107.1 | 159.0 | 222.0 |
| 30 | 21.5 | 30.3 | 49.1 | 65.2 |

The Reynolds number Re is the ratio of inertial forces to viscous forces. For Newtonian solutions flowed through porous media the Reynolds number is calculated as

$$Re = \frac{\rho V_0 d_b}{\eta(1-\varphi)}, \qquad 4\text{-}5$$

where $\varphi$ is the bed porosity, $d_b$ is the diameter of glass beads, $V_0 \approx \varphi v_{\text{avg}}$ is the superficial velocity, $\rho$ is the fluid density of, and $\eta$ is the fluid viscosity. For non-

Newtonian power-law fluids flowed through porous media the Reynolds number is calculated as

$$Re = \frac{\rho {V_0}^{2-n} d_b}{\psi(1-\varphi)}, \qquad 4\text{-}6$$

where $\psi = \frac{k}{12}(9 + \frac{3}{n})^n)(150s\varphi)^{(1-n)/2}$, $n$ and $k$ are the exponent and pre-factor of the power-law that describes the shear dependence of the viscosity, and $s = \frac{{d_b}^2}{150}\frac{\varphi^3}{(1-\varphi)^2}$ is the permeability of the porous bed.[223]

**Table 4.4** Re numbers $\times 10^6$ of nanoparticles in HPAM flowed through porous media with bead diameters of 5.4, 10, and 30 µm at flow rates of 5 – 20 µl/hr.

| **Bead size $d_b$ (µm)** | **Flow Rate Q (µm/sec)** | | | |
|---|---|---|---|---|
| | 5 | 10 | 15 | 20 |
| 5.4 | 0.93 | 1.50 | 2.54 | 4.46 |
| 10 | 0.94 | 2.65 | 5.07 | 8.75 |
| 30 | 1.01 | 1.77 | 3.90 | 6.21 |

**Table 4.5** Re numbers $\times 10^6$ of nanoparticles in glycerol/water flowing through porous media with bead diameters of 5.4, 10, and 30 µm at flow rates of 5 – 20 µl/hr.

| **Bead size $d_b$ (µm)** | **Flow Rate Q (µm/sec)** | | | |
|---|---|---|---|---|
| | 5 | 10 | 15 | 20 |
| 5.4 | 0.36 | 0.46 | 0.73 | 0.98 |
| 10 | 0.65 | 1.35 | 1.80 | 2.52 |
| 30 | 2.48 | 4.00 | 5.15 | 7.03 |

**Table 4.6** Re numbers $\times 10^6$ of nanoparticles in water flowing through porous media with bead diameters of 5.4, 10, and 30 µm at flow rates of 5 – 20 µl/hr.

| **Bead size $d_b$ (µm)** | **Flow Rate Q (µm/sec)** | | | |
|---|---|---|---|---|
| | 5 | 10 | 15 | 20 |
| 5.4 | 50.90 | 74.30 | 99.72 | 125.11 |
| 10 | 93.07 | 163.50 | 196.05 | 268.71 |
| 30 | 321.42 | 542.37 | 716.59 | 848.63 |

The Péclet number Pe, the ratio of convective transport to diffusive transport, is calculated as

$$Pe = \frac{v_{\text{avg}} l_c}{D_q}, \quad 4\text{-}7$$

where $D_q$ is the quiescent diffusion coefficient of the nanoparticles in different porous media.

**Table 4.7** Pe numbers $\times 10^{-2}$ of nanoparticles in HPAM flowed through porous media with bead diameters of 5.4, 10, and 30 µm at varying flow rates of 5 – 20 µl/hr.

| **Bead size $d_b$ (µm)** | **Flow Rate Q (µm/sec)** | | | |
|---|---|---|---|---|
| | 5 | 10 | 15 | 20 |
| 5.4 | 265.96 | 352.64 | 486.33 | 685.70 |
| 10 | 277.64 | 522.79 | 776.22 | 1083.73 |
| 30 | 340.15 | 479.01 | 776.02 | 1030.87 |

**Table 4.8** Pe numbers $\times 10^{-2}$ of nanoparticles in glycerol/water flowed through porous media with bead diameters of 5.4, 10, and 30 µm at flow rates of 5 – 20 µl/hr.

| **Bead size $d_b$ (µm)** | **Flow Rate Q (µm/sec)** | | | |
|---|---|---|---|---|
| | 5 | 10 | 15 | 20 |
| 5.4 | 46.74 | 68.23 | 91.57 | 114.88 |
| 10 | 70.48 | 123.82 | 148.47 | 203.49 |
| 30 | 166.38 | 280.75 | 370.94 | 439.29 |

**Table 4.9** Pe numbers $\times 10^{-2}$ of nanoparticles in water flowed through porous media with bead diameters of 5.4, 10, and 30 µm at flow rates of 5 – 20 µl/hr.

| **Bead size $d_b$ (µm)** | **Flow Rate Q (µm/sec)** | | | |
|---|---|---|---|---|
| | 5 | 10 | 15 | 20 |
| 5.4 | 0.80 | 1.17 | 1.58 | 1.98 |
| 10 | 1.18 | 2.08 | 2.49 | 3.41 |
| 30 | 1.82 | 3.07 | 4.06 | 4.81 |

## 4.4 Results and discussion

To determine the effect of non-Newtonian flow properties on the transport of nanoparticles in highly confined media, we formulated two solutions: a non-Newtonian polymer solution, consisting of 0.1 wt% partially hydrolyzed polyacrylamide (HPAM) of

weight-averaged molecular weight $M_w$ = 8 000 000, and a Newtonian 90-10 w/w mixture of glycerol and water. The HPAM solution is strongly shear-thinning. Its viscosity at zero shear rate [2.7 Pa-s] is somewhat larger than that of the glycerol/water mixture [0.11 Pa-s]; at a shear rate of $\dot{\gamma} \approx 1.6\ s^{-1}$, however, its viscosity equals that of the glycerol/water mixture.[22] Fluorescent polystyrene nanoparticles were added to both solutions at a concentration of $2 \times 10^{-3}$ wt % and tumbled on a roll mill for up to 24 hours to ensure that the particles were uniformly dispersed. Borosilicate microcapillary cells of inner side length 0.7 mm and length of 5 cm were packed with one of three different sizes of beads: borosilicate glass microspheres of diameter 5.4 ± 0.3 μm or 10.0 ± 1.0 μm or soda lime glass microspheres of diameter 30.1 ± 1.1 μm. After sintering, the average porosity $\phi$, average pore size $d_{pore}$, and average confinement length $l_c$ of the beds were characterized using two-dimensional confocal microscopy. Particles suspended in HPAM solutions, in glycerol/water, and in deionized water were flowed through the beds, imaged with high-speed confocal microscopy at 110 frames/sec, and tracked over time using standard algorithms.[121] By varying the flow rate from 5 to 20 μL/hr (accessing in different fluids Péclet numbers of $2 \times 10^1 < Pe < 3 \times 10^5$), we accessed flows in the coupled diffusion-advection ($6 < Pe < 72$) and mechanically-mixed ($Pe > 72$) regimes.[104]

For a given fluid, the microscopic flow profiles do not depend on the bed geometry (Figure 4.2—Figure 4.5). At a fixed bulk flow rate, the longitudinal ($x$) and transverse ($y$) distributions of velocity for nanoparticles flowing through beds of varying bead size in Newtonian (Figure 4.2—Figure 4.5d,e) and non-Newtonian (Figure

4.2—Figure 4.5f,g), after normalizing by the average bulk flow velocity $v_{avg}$, collapse onto separate scaling curves. Each longitudinal velocity distribution $G(v_x/v_{\mathrm{avg}})$ has an exponentially-stretched positive tail, consistent with earlier measurements of non-Gaussian velocity distributions from simulation[97] and experiment;[109,224] each transverse velocity distribution $G(v_y/v_{\mathrm{avg}})$ is non-Gaussian yet symmetric about zero, indicating that particle mobility does not have a preferred direction perpendicular to the bulk flow.

Figure 4.2 shows dependence of normalized velocity distributions on pore size for Newtonian and for non-Newtonian solutions: (a-c) trajectories of nanoparticles transported through porous beds with bead diameter ($d_b$) of (a) 5 μm, (b) 10 μm, or (c) 30 μm at an inlet flow rate of 5 μl/hr. Colors indicate the velocity along the flow direction ($v_x$): (d-g) normalized distributions of longitudinal [$G(v_x/v_{\mathrm{avg}})$] and transverse [$G(v_y/v_{\mathrm{avg}})$] velocities for nanoparticles transported in (d, e) a glycerol/water mixture (90 w/w%) and (f, g) an HPAM solution (0.1 w/w%) at inlet flow rate of 5 μl/hr through a porous bed with bead diameter of 5 μm (gold circle), 10 μm (blue square), or 30 μm (red triangle). The bead diameter and pore size do not affect the normalized distributions of nanoparticle velocities for Newtonian or for non-Newtonian fluids.

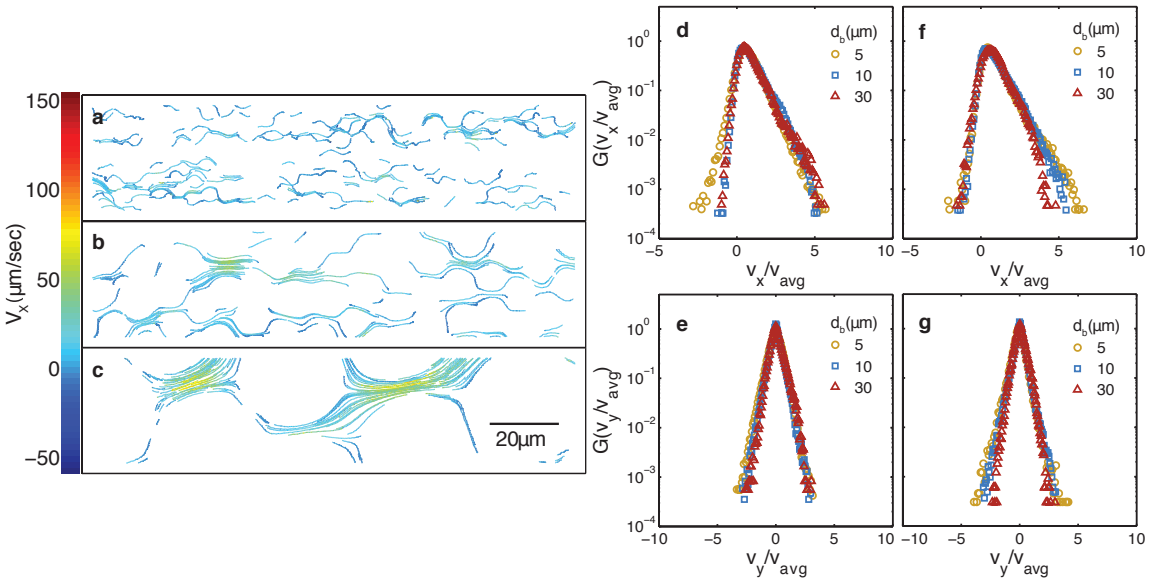


**Figure 4.2** Dependence of normalized velocity distributions on pore size for Newtonian and for non-Newtonian solutions transported through porous beds with varying bead diameters at an inlet flow rate of 5 µl/hr.

Figure 4.3 illustrates dependence of normalized velocity distributions on pore size for Newtonian and for non-Newtonian solutions: (a-c) trajectories of nanoparticles transported through porous beds with bead diameter ($d_b$) of (a) 5 µm, (b) 10 µm, or (c) 30 µm at an inlet flow rate of 10 µl/hr. Colors indicate the velocity along the flow direction ($v_x$): (d-g) normalized distributions of longitudinal [$G(v_x/v_{\text{avg}})$] and transverse [$G(v_y/v_{\text{avg}})$] velocities for nanoparticles transported in (d, e) a glycerol/water mixture (90 w/w%) and (f, g) an HPAM solution (0.1 w/w%) at inlet flow rate of 10 µl/hr through a porous bed with bead diameter of 5 µm (gold circle), 10 µm (blue square), or 30 µm (red triangle). The bead diameter and pore size do not affect the normalized distributions of nanoparticle velocities for Newtonian or for non-Newtonian fluids.

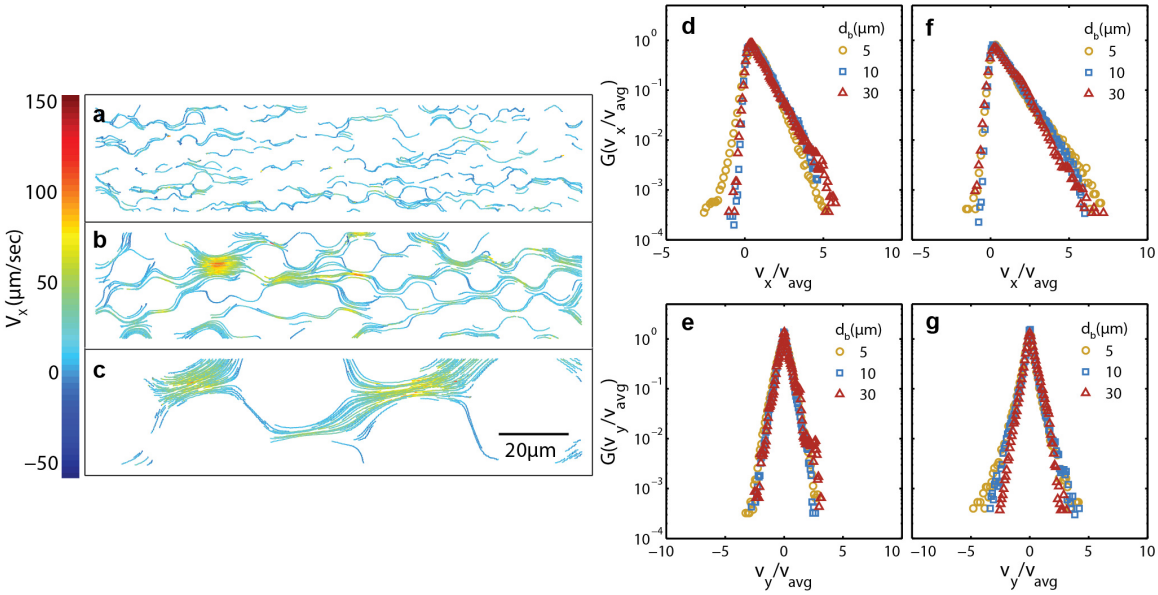


**Figure 4.3** Dependence of normalized velocity distributions on pore size for Newtonian and for non-Newtonian solutions transported through porous beds with varying bead diameters at an inlet flow rate of 10 μl/hr.

Figure 4.4 represents dependence of normalized velocity distributions on pore size for Newtonian and for non-Newtonian solutions: (a-c) trajectories of nanoparticles transported through porous beds with bead diameter ($d_b$) of (a) 5 μm, (b) 10 μm, or (c) 30 μm at an inlet flow rate of 15 μl/hr. Colors indicate the velocity along the flow direction ($v_x$): (d-g) normalized distributions of longitudinal [$G(v_x/v_{\text{avg}})$] and transverse [$G(v_y/v_{\text{avg}})$] velocities for nanoparticles transported in (d, e) a glycerol/water mixture (90 w/w%) and (f, g) an HPAM solution (0.1 w/w%) at inlet flow rate of 15 μl/hr through a porous bed with bead diameter of 5 μm (gold circle), 10 μm (blue square), or 30 μm (red triangle). The bead diameter and pore size do not affect the normalized distributions of nanoparticle velocities for Newtonian or for non-Newtonian fluids.

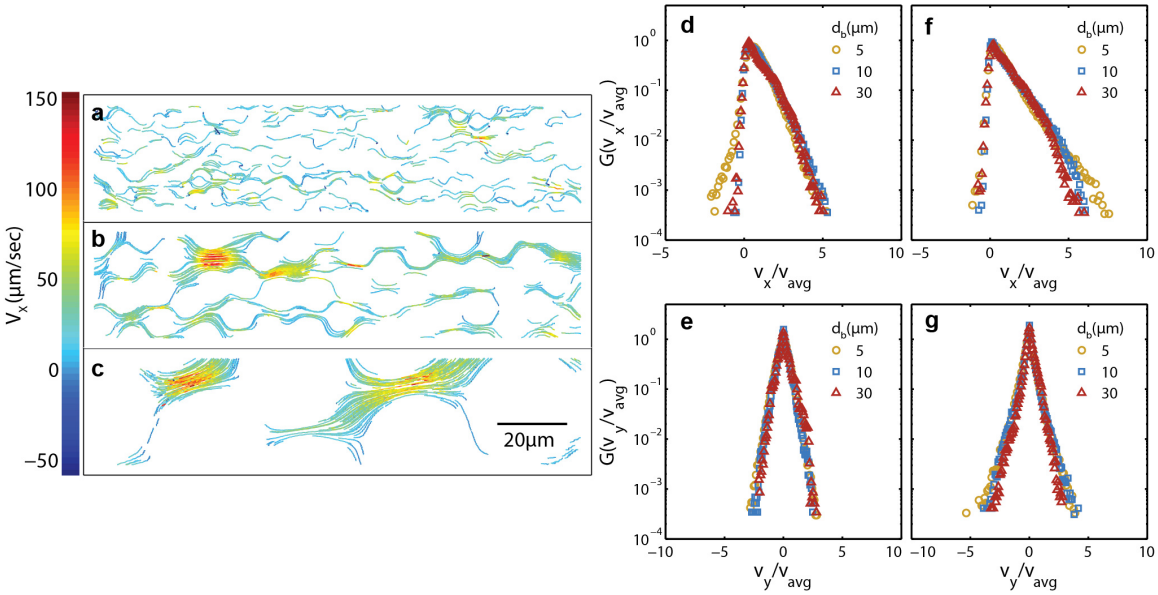


**Figure 4.4** Dependence of normalized velocity distributions on pore size for Newtonian and for non-Newtonian solutions transported through porous beds with varying bead diameters at an inlet flow rate of 15 μl/hr.

Figure 4.5 demonstrates dependence of normalized velocity distributions on pore size for Newtonian and for non-Newtonian solutions: (a-c) trajectories of nanoparticles transported through porous beds with bead diameter ($d_b$) of (a) 5 μm, (b) 10 μm, or (c) 30 μm at an inlet flow rate of 20 μl/hr. Colors indicate the velocity along the flow direction ($v_x$): (d-g) normalized distributions of longitudinal [$G(v_x/v_{\text{avg}})$] and transverse [$G(v_y/v_{\text{avg}})$] velocities for nanoparticles transported in (d, e) a glycerol/water mixture (90 w/w%) and f, g) an HPAM solution (0.1 w/w%) at inlet flow rate of 20 μl/hr through a porous bed with bead diameter of 5 μm (gold circle), 10 μm (blue square), or 30 μm (red triangle). The bead diameter and pore size do not affect the normalized distributions of nanoparticle velocities for Newtonian or for non-Newtonian fluids.

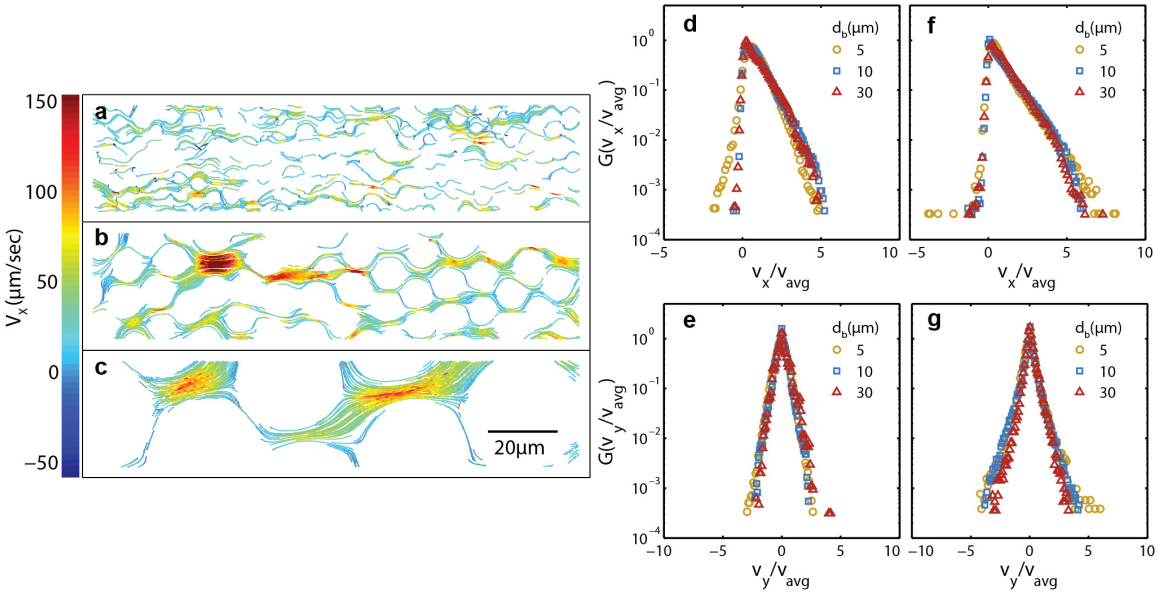


**Figure 4.5** Dependence of normalized velocity distributions on pore size for Newtonian and for non-Newtonian solutions transported through porous beds with varying bead diameters at an inlet flow rate of 20 μl/hr.

Similarly, the microscopic velocity distributions for the Newtonian and for the non-Newtonian fluid are independent of the bulk flow rate for a fixed bead size (Figure 4.6—Figure 4.8).

Figure 4.6 illustrates dependence of normalized velocity distributions on flow rate for Newtonian and for non-Newtonian solutions: (a-d) trajectories of nanoparticles transported through porous beds with bead diameter of 5 μm at bulk flow rates of (a) 5, (b) 10, (c) 15, and (d) 20 μl/hr. Colors represent velocity variation along the flow direction ($v_x$): (e-h) normalized distributions of longitudinal $[G(v_x/v_{\text{avg}})]$ and transverse $[G(v_y/v_{\text{avg}})]$ velocities for nanoparticles in (e, f) a glycerol/water mixture (90 w/w%) and (g, h) an HPAM solution (0.1 w/w%) at an inlet flow rate of 5 (purple circle), 10 (blue square), 15 (red triangle), or 20 (gold diamond) μl/hr through a porous bed with bead

diameter of 5 μm. The inlet flow rate does not affect the normalized distributions of nanoparticle velocities for Newtonian or for non-Newtonian fluids.

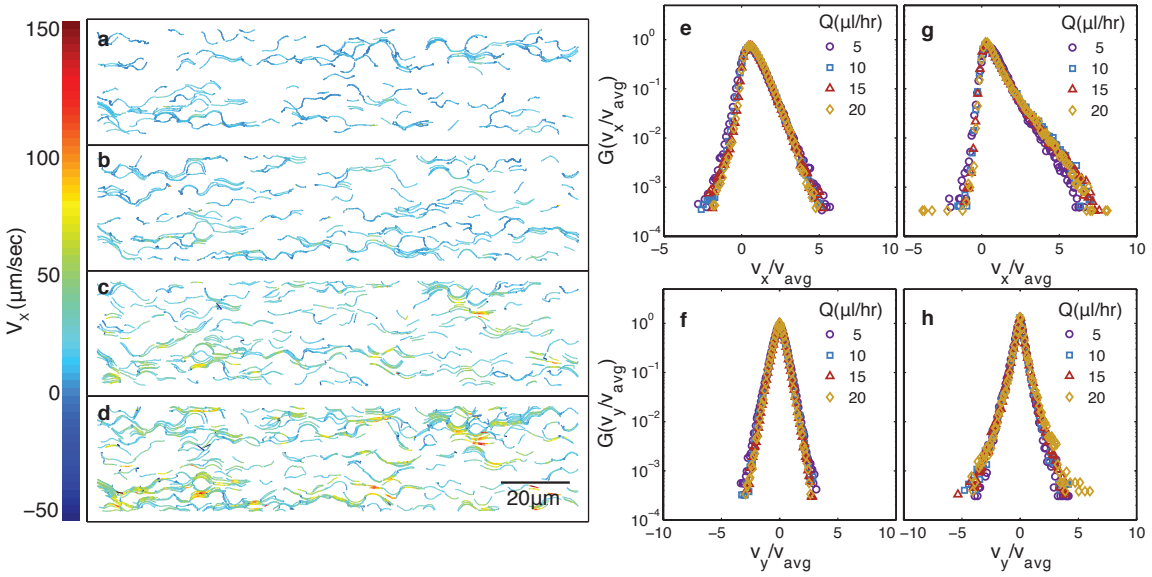


**Figure 4.6** Dependence of normalized velocity distributions on flow rate for Newtonian and for non-Newtonian solutions transported through porous beds with bead diameter of 5 μm at bulk flow rates of 5 – 20 μl/hr.

Figure 4.7 represents dependence of normalized velocity distributions on flow rate for Newtonian and for non-Newtonian solutions: (a-d) trajectories of nanoparticles transported through porous beds with bead diameter of 10 μm at bulk flow rates of (a) 5, (b) 10, (c) 15, and (d) 20 μl/hr. Colors represent velocity variation along the flow direction ($v_x$): (e-h) normalized distributions of longitudinal [$G(v_x/v_{\text{avg}})$] and transverse [$G(v_y/v_{\text{avg}})$] velocities for nanoparticles in (e, f) a glycerol/water mixture (90 w/w%) and (g, h) an HPAM solution (0.1 w/w%) at an inlet flow rate of 5 (purple circle), 10 (blue square), 15 (red triangle), or 20 (gold diamond) μl/hr through a porous bed with bead

diameter of 10 μm. The inlet flow rate does not affect the normalized distributions of nanoparticle velocities for Newtonian or for non-Newtonian fluids.

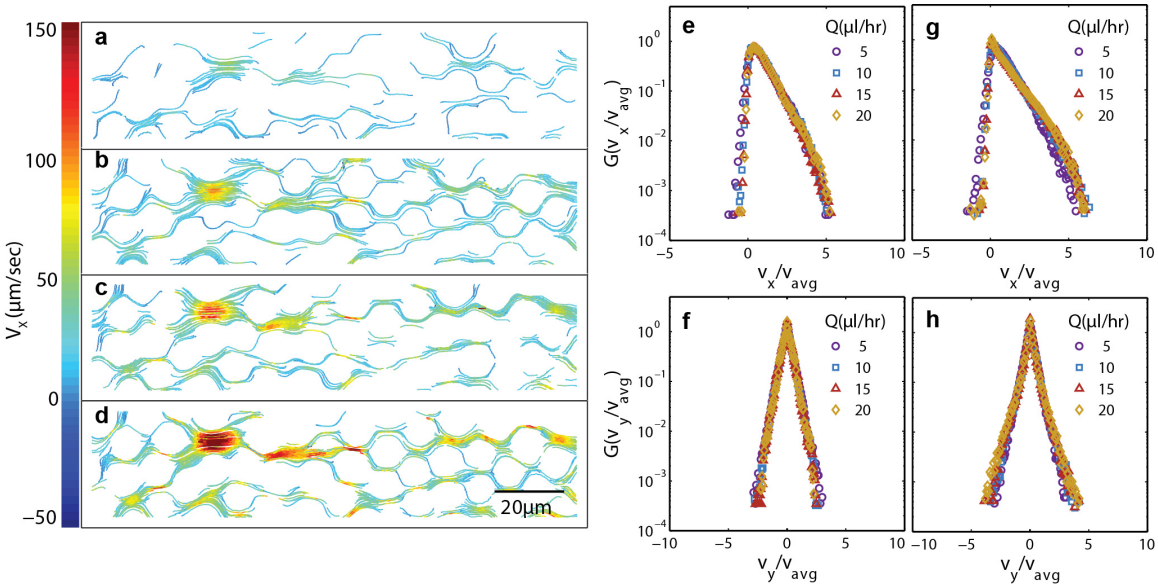


**Figure 4.7** Dependence of normalized velocity distributions on flow rate for Newtonian and for non-Newtonian solutions transported through porous beds with bead diameter of 10 μm at bulk flow rates of 5 – 20 μl/hr.

Figure 4.8 shows dependence of normalized velocity distributions on flow rate for Newtonian and for non-Newtonian solutions: (a-d) trajectories of nanoparticles transported through porous beds with bead diameter of 30 μm at bulk flow rates of (a) 5, (b) 10, (c) 15, and (d) 20 μl/hr. Colors represent velocity variation along the flow direction ($v_x$): (e-h) normalized distributions of longitudinal [$G(v_x/v_{\text{avg}})$] and transverse [$G(v_y/v_{\text{avg}})$] velocities for nanoparticles in (e, f) a glycerol/water mixture (90 w/w%) and (g, h) an HPAM solution (0.1 w/w%) at an inlet flow rate of 5 (purple circle), 10 (blue square), 15 (red triangle), or 20 (gold diamond) μl/hr through a porous bed with bead

diameter of 30 μm. The inlet flow rate does not affect the normalized distributions of nanoparticle velocities for Newtonian or for non-Newtonian fluids.

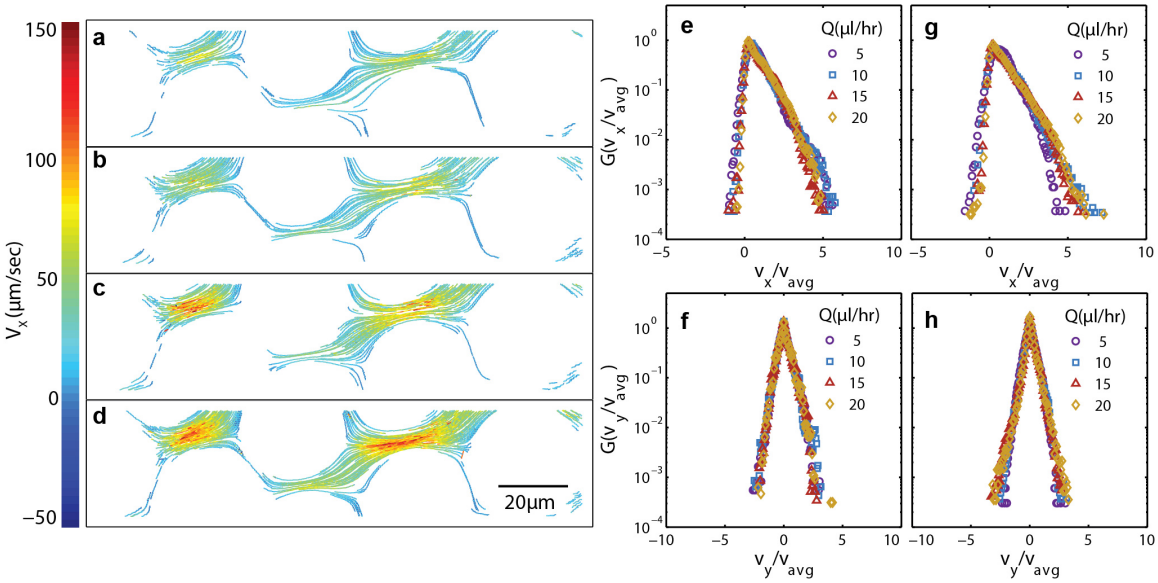


**Figure 4.8** Dependence of normalized velocity distributions on flow rate for Newtonian and for non-Newtonian solutions transported through porous beds with bead diameter of 30 μm at bulk flow rates of 5 – 20 μl/hr.

The scaling curves for Newtonian glycerol/water and non-Newtonian HPAM solutions can be superimposed for modest normalized velocities but diverge for larger velocities (Figure 4.9), where elastic instabilities can enhance fluctuations in the velocity.[217]

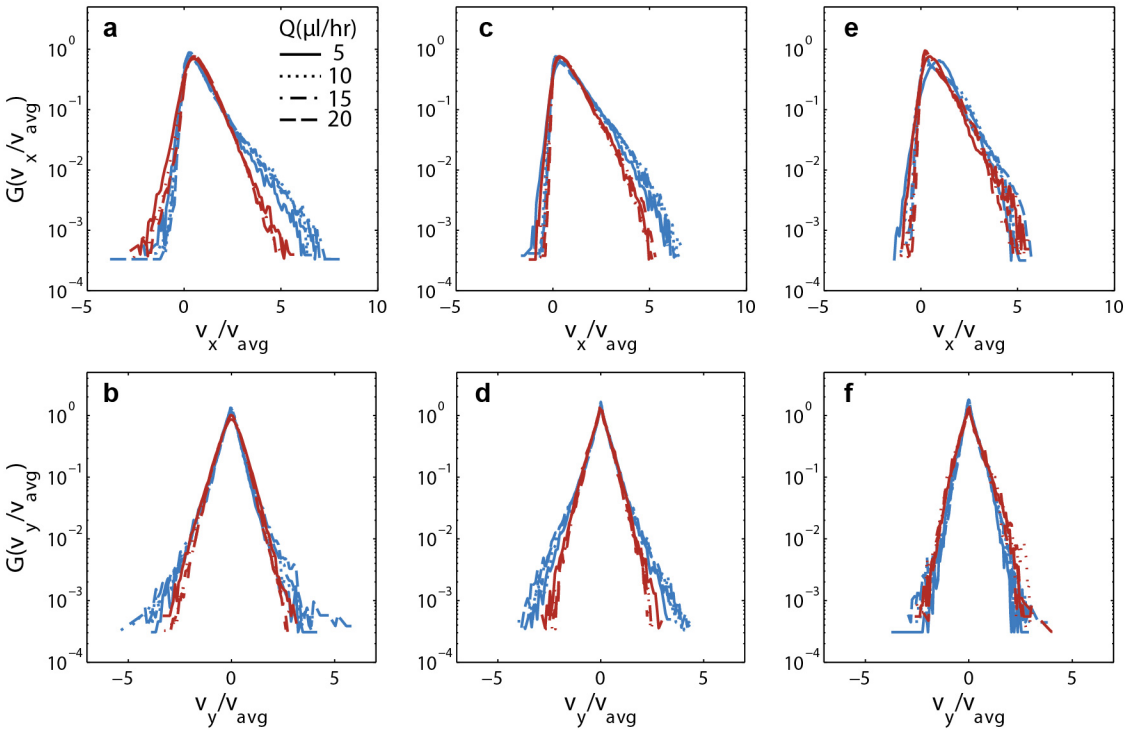


**Figure 4.9** Normalized longitudinal (top row) and transverse (bottom row) velocity distributions for nanoparticles flowed in glycerol/water (red) and in HPAM (blue) at inlet flow rates of 5 µl/hr (line), 10 µl/hr (dotted line), 15 µl/hr (dashed-dotted line), and 20 µl/hr (dashed line) through porous media with bead diameters of (a,b) 5.4 µm, (c,d) 10 µm, and (e,f) 30 µm.

To connect the microscopic velocity distributions to macroscopic dispersion, we calculate the time-dependent longitudinal dispersion coefficients[89] as $D_L(t) = \frac{1}{2}\frac{d\sigma_L^2}{dt} = \int C_L(t')dt'$, where $C_L(t)$ is the autocovariance of the nanoparticle velocity $v_x(t)$ along the flow direction ($x$), given by $C_L(t) = \sum_{i=1}^{N}\big(v_{x,i}(t) - \langle v_x \rangle\big)\big(v_{x,i}(0) - \langle v_x \rangle\big)$, and $\sigma_L^2(t)$ is the second moment of the longitudinal particle displacements; the time-dependent transverse dispersion coefficient is similarly defined. We normalize $D_L(t)$ and $D_T(t)$ by the quiescent diffusivity of the nanoparticles in the background solution, $D_q$, and the lag

time by the characteristic convective time scale, $d_b/v_{\text{avg}}$. On short time scales, both $D_L/D_q$ and $D_T/D_q$ increase with dimensionless time $\tau = tv_{\text{avg}}/d_b$ as the particles are advected and mixed by the flow in the porous medium (Figure 4.10—Figure 4.12), consistent with the idea that the fluid rheology affects the local flow behavior.[218] Both ratios initially increase as power laws with $\tau$. On long time scales, $D_L/D_q$ and $D_T/D_q$ are expected to approach an asymptotic limiting value if the time domain of the correlation is smaller than the residence time in the porous medium. For longitudinal dispersion this time scale is set by convection and is typically $5 < \tau < 10$ [refs[89,225]]. The time corresponding to maximum longitudinal dispersion decreases approximately linearly with increasing bead diameter (Figure 4.10—Figure 4.12). Transverse dispersion approaches a local maximum at a normalized time of $\tau \approx 0.4$ and decreases slightly on longer time scales, approximately independent of the flow rate and bead diameter (Figure 4.10—Figure 4.12); the slight decrease on longer times reflects contributions from the slowest particles in strong confinement.[226] The timescale is in reasonable agreement with the asymptotic prediction,[212] $\tau > \sqrt{1-\varphi} \approx 0.8$, calculated using the average bed porosity $\varphi \approx 0.35$ for different beds.

Figure 4.10 illustrates time dependent dispersion of nanoparticles in Newtonian and non-Newtonian solutions: normalized longitudinal ($D_L/D_q$, a and c) and transverse ($D_T/D_q$, b and d) dispersions of nanoparticles in (a, b) a glycerol/water mixture (90 w/w%) and (c, d) a HPAM solution (0.1 w/w%) as a function of normalized lag time ($\tau = tv_{avg}/d_b$) through a porous bed with bead diameter of 5 μm. Colors indicate

different flow rates: 5 µl/hr (purple), 10 µl/hr (blue), and 15 µl/hr (red), and 20 µl/hr (gold). Open symbols indicate Newtonian fluids (glycerol/water mixture) and closed symbols indicate non-Newtonian solutions (HPAM). The insets in each panel show the same data on linear axes.

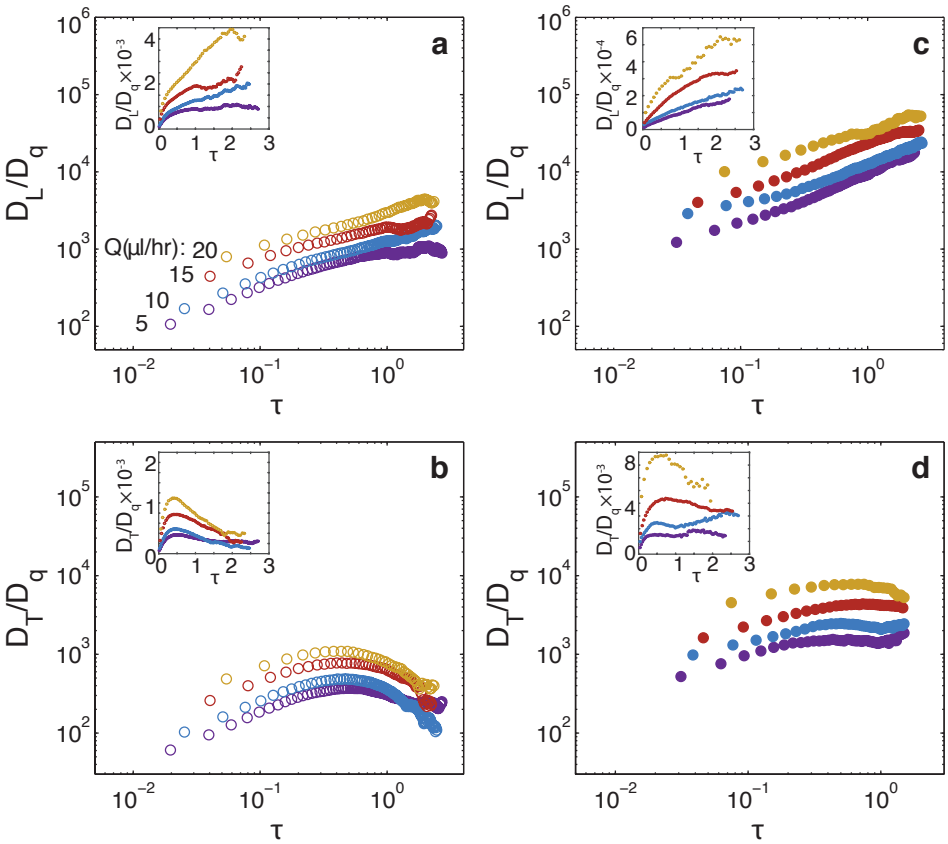


**Figure 4.10** Normalized longitudinal (a and c) and transverse (b and d) dispersions of nanoparticles in (a, b) a glycerol/water and (c, d) a HPAM as a function of normalized lag time through a porous bed with bead diameter of 5 µm.

Figure 4.11 shows time dependent dispersion of nanoparticles in Newtonian and non-Newtonian solutions: normalized longitudinal ($D_L/D_q$, a and c) and transverse ($D_T/D_q$, b and d) dispersions of nanoparticles in (a, b) a glycerol/water mixture (90

w/w%) and (c, d) a HPAM solution (0.1 w/w%) as a function of normalized lag time ($\tau = tv_{avg}/d_b$) through a porous bed with bead diameter of 10 μm. Colors indicate different flow rates: 5 μl/hr (purple), 10 μl/hr (blue), and 15 μl/hr (red), and 20 μl/hr (gold). Open symbols indicate Newtonian fluids (glycerol/water mixture) and closed symbols indicate non-Newtonian solutions (HPAM). The insets in each panel show the same data on linear axes.

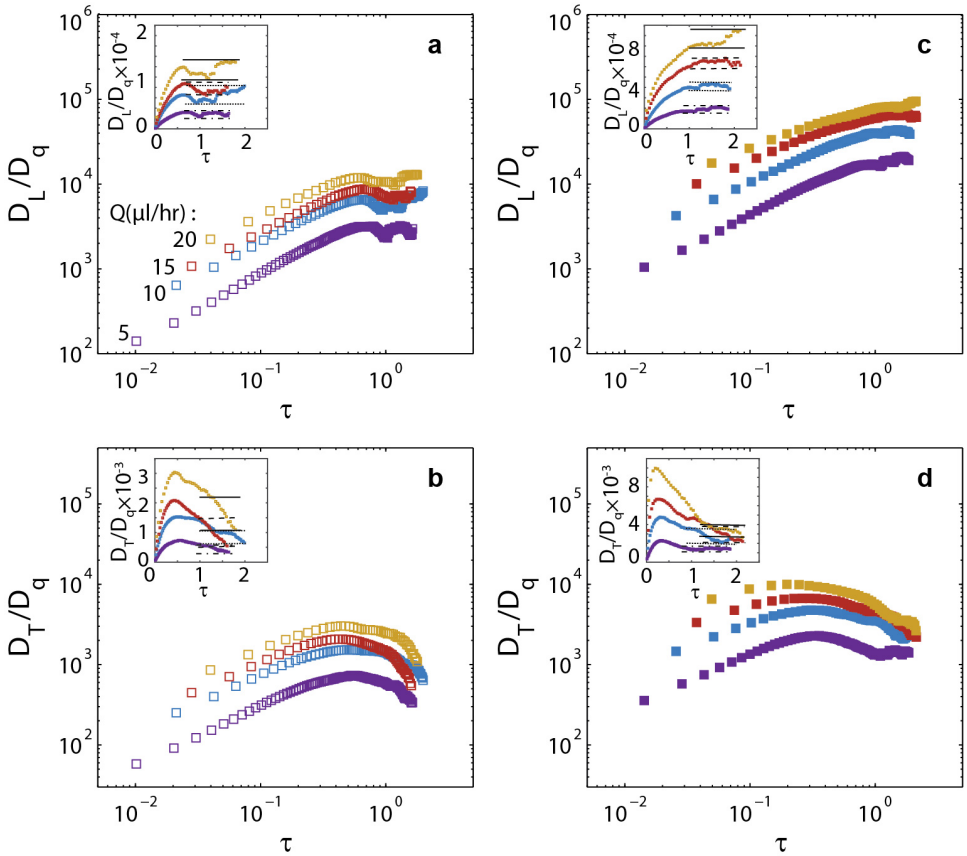


**Figure 4.11**. Normalized longitudinal (a and c) and transverse (b and d) dispersions of nanoparticles in (a, b) a glycerol/water and (c, d) a HPAM as a function of normalized lag time through a porous bed with bead diameter of 10 μm.

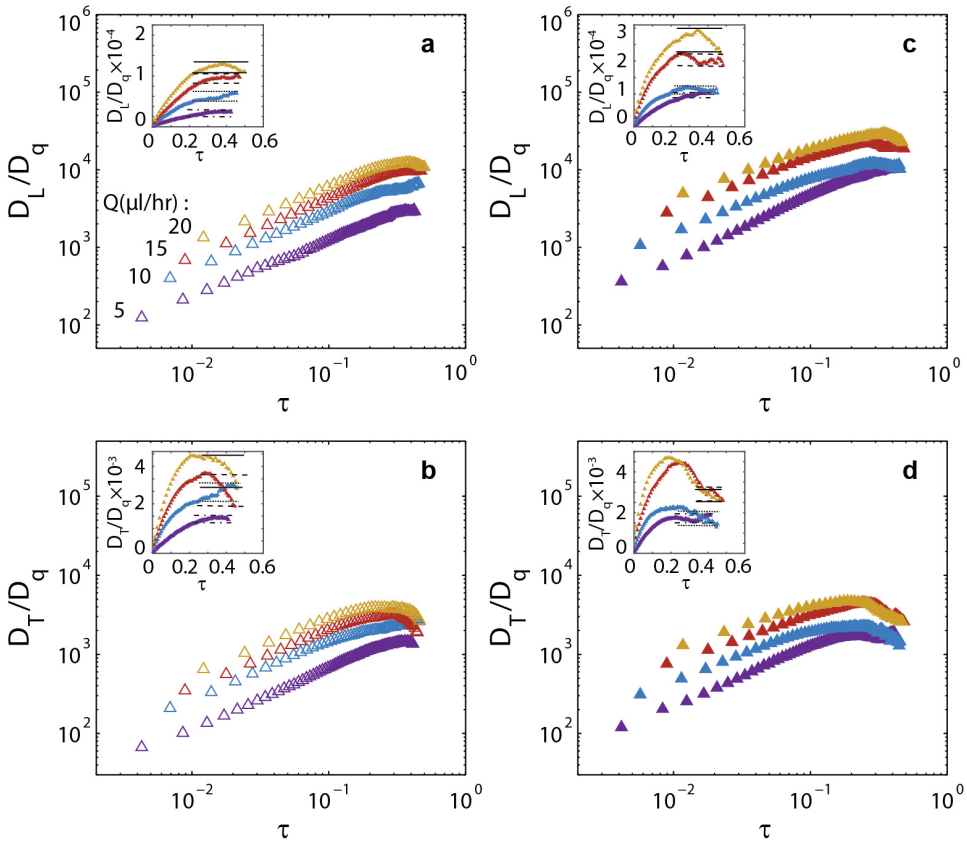


**Figure 4.12** Normalized longitudinal (a and c) and transverse (b and d) dispersions of nanoparticles in (a, b) a glycerol/water and (c, d) a HPAM as a function of normalized lag time through a porous bed with bead diameter of 30 μm.

Figure 4.12 represents time dependent dispersion of nanoparticles in Newtonian and non-Newtonian solutions: normalized longitudinal ($D_L/D_q$, a and c) and transverse ($D_T/D_q$, b and d) dispersions of nanoparticles in (a, b) a glycerol/water mixture (90 w/w%) and (c, d) a HPAM solution (0.1 w/w%) as a function of normalized lag time ($\tau = tv_{avg}/d_b$) through a porous bed with bead diameter of 30 μm. Colors indicate different flow rates: 5 μl/hr (purple), 10 μl/hr (blue), and 15 μl/hr (red), and 20 μl/hr (gold). Open symbols indicate Newtonian fluids (glycerol/water mixture) and closed

symbols indicate non-Newtonian solutions (HPAM). The insets in each panel show the same data on linear axes.

From the limiting values of the dispersion ratios, we extract the long-time asymptotic dispersion coefficients. Across the range of bed particle diameters and flow rates accessed here, the normalized longitudinal and transverse dispersion coefficients collapse onto master curves (Figure 4.13) as a function of the Péclet number $\mathrm{Pe} = v_{\mathrm{avg}} l_c / D_q$ (Table 4.7—Table 4.9). The scaling collapse across different bead diameters and flow rates for a given fluid supports the microscopic definitions of $D_L$, $D_T$, and Pe employed here. The surprising scaling collapse across different fluids indicates that the non-Newtonian characteristics of the polymer solution do not affect the dispersion of nanoparticles flowed through disordered media. $D_L/D_q$ and $D_T/D_q$ scale linearly with Pe, consistent with earlier results across a similar range of Pe in random porous media. The ratio of the longitudinal and transverse dispersion coefficients $D_L/D_T$ varies between 1 and 10. For the largest bead size ($d_b \approx 30$ μm) $D_L/D_T$ is approximately unity, showing that the particles uniformly disperse in all directions; as the bed particle diameter is decreased $D_L/D_T$ increases slightly, consistent with preferential transport along the longitudinal direction enhanced by confinement.[120]

Figure 4.13 shows (a) normalized longitudinal dispersion coefficient ($D_L/D_q$) and (b) normalized transverse dispersion coefficient ($D_T/D_q$) of nanoparticles in water, glycerol/water mixture (90 w/w%), and HPAM solution (0.1 w/w%) as a function of Péclet number $\mathrm{Pe} = v_{\mathrm{avg}} l_c / D_q$, where the characteristic length scale is taken as the

average void size $l_c$. Dashed line indicates a linear fit: (c) ratio of longitudinal and transverse dispersions ($D_L/D_T$) as a function of Pe. Colors indicate the flow rate: (purple) 5, (blue) 10, (red) 15, or (gold) 20μl/hr. Symbols indicate the bead diameter: (circle) 5 μm, (square) 10 μm, or (triangle) 30μm. Open symbols indicate Newtonian fluids (glycerol/water mixture or water) and closed symbols indicate non-Newtonian solutions (HPAM).

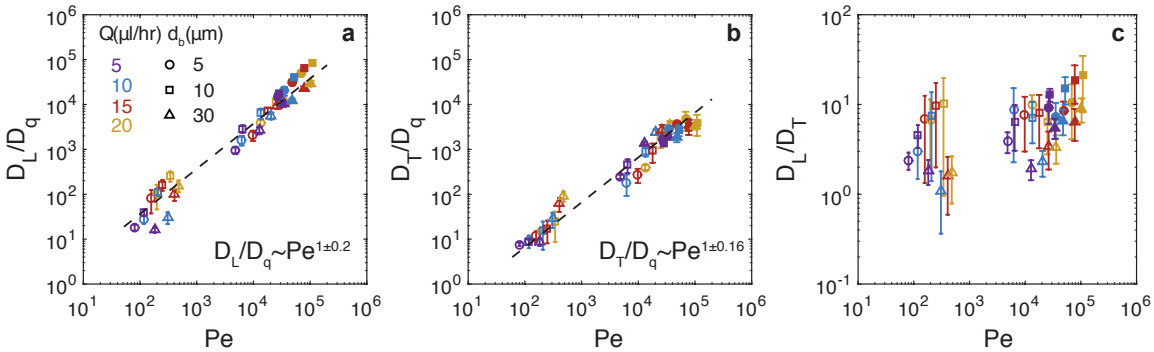


**Figure 4.13** (a) Normalized longitudinal dispersion coefficient and (b) normalized transverse dispersion coefficient of nanoparticles in water, glycerol/water, and HPAM as a function of Péclet number, (c) Ratio of longitudinal and transverse dispersions as a function of Pe.

Non-Newtonian characteristics of the fluids do not affect asymptotic dispersion in the mechanically-mixed regime. On shorter time scales, however, differences in the approach to asymptotic dispersion arise from differences in the shear-rate-dependent fluid response. We fit power-laws to the short-time limit in Figure 4.10—Figure 4.12 (i.e. $D_L \sim \tau^{\beta_L}$ and $D_T \sim \tau^{\beta_T}$) and extract the exponents $\beta_L$ and $\beta_T$ (Figure 4.14). The magnitude and flow-rate dependence of $\beta_L$ is similar for glycerol/water and HPAM solutions, consistent with the idea that the evolution of longitudinal dispersion is related

to the total distance traveled through the packed bed.[218] By contrast, the dependence of $\beta_T$ on flow rate becomes weaker as Wi is increased (e.g. as $l_c$ is decreased). The differences in the time to reach asymptotic diffusion may reflect coupling between the dynamics of the particles and polymer chains on short time scales,[35] where advection is coupled to diffusing mixing.[104] Nonetheless, random mixing in the disordered porous medium ensures that the non-Newtonian characteristics do not affect asymptotic dispersion.

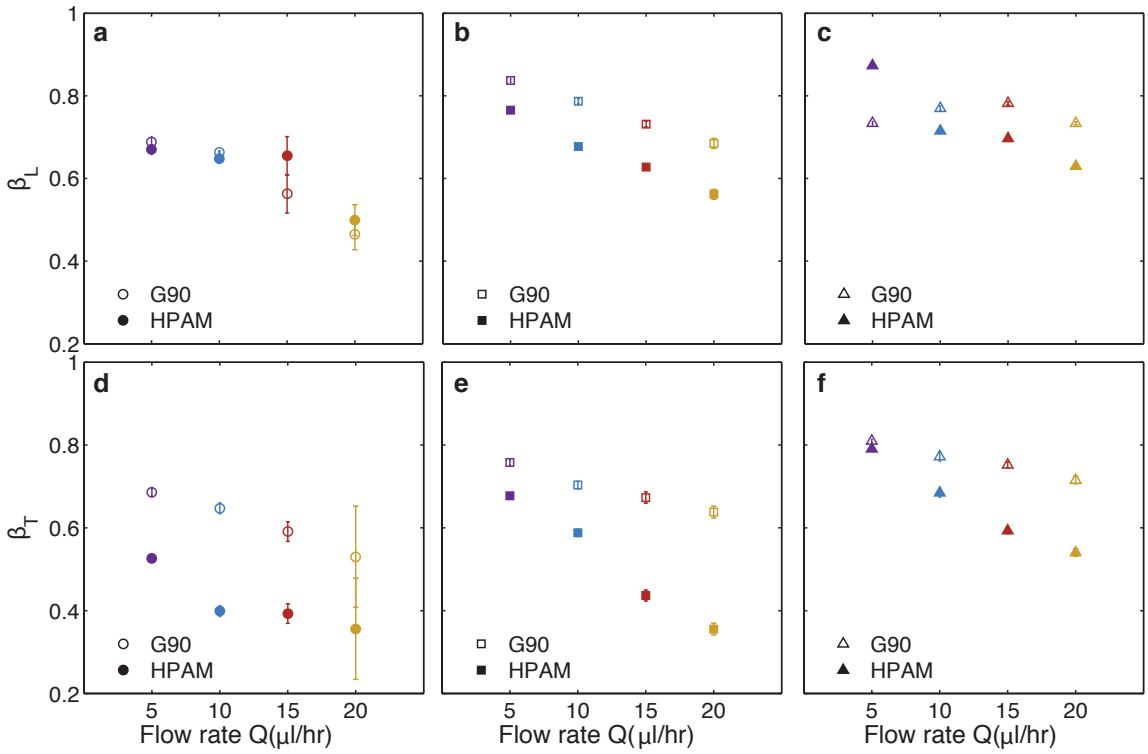


**Figure 4.14** Short-time dispersion exponents in Newtonian and non-Newtonian solutions. Power-law exponent of time-dependent longitudinal (a-c) and transverse (d-f) dispersion coefficients in porous beds with bead diameter of (a, d) 5 μm, (b, e) 10 μm, and (c, f) 30 μm. Open symbols indicate Newtonian and closed symbols indicate non-Newtonian solutions (HPAM).

## 4.5 Conclusion

Dispersion of particles suspended in non-Newtonian fluids in disordered porous media hence contrasts sharply to that observed in structured media. In non-Newtonian fluids, elastic turbulence enhances velocity fluctuations.[227] In structured media this process promotes streamline crossing and dramatically enhances transverse particle dispersion,[217] because the fluctuations are not averaged out by the geometry of the medium. This comparison highlights the critical role of the random mixing provided by disordered porous media in suppressing the non-Newtonian characteristics of the fluid. Other changes in suspension properties that enhance velocity variations, for example increasing the concentration of particles,[228] are thus expected to increase dispersion.

This striking insensitivity of particle dispersion to solution characteristics affects the choice of fluids used in applications demanding control over particle structure, dispersion, and transport. In applications involving disordered porous media, such as chromatographic separations or hydrocarbon extraction including hydraulic fracturing and enhanced oil recovery, existing models for asymptotic dispersion in Newtonian fluids can be applied as-is to predict and control particle transport; changing the fluid characteristics alone will not modify particle dispersion. Instead, fundamentally different strategies are required to increase dispersion in applications for which particles must be uniformly dispersed, as in 3-D printing of particle-laden resins or in processing of polymer nanocomposites. Here particles suspended in non-Newtonian fluids must be transported through an *ordered* pore or channel structured nozzles to ensure uniform

dispersion. Hence we expect that modulating the flow geometry, not the fluid rheology, is the most promising route to tailor dispersion.

# Chapter 5

## 5.0 Dispersion of nanoparticles in bidisperse porous media

Mobility of nanoparticles through porous media depends on flow characteristics and bed heterogeneities. In this chapter, we visualize transport of nanoparticles suspended in Newtonian and non-Newtonian solutions through porous media composed of glass beads of two different sizes (5 μm and 20 μm) using confocal microscopy. We calculate the distributions of longitudinal and transverse velocities of nanoparticles through bidisperse beds with varying fraction of the small beads and varying solution properties. We find that, for each solution, the distributions of normalized longitudinal and transverse velocities scale onto a master curve, independent of bi-dispersity ratio and flow rate. From the trajectories of the nanoparticles we also measure time-dependent dispersion of nanoparticles in both longitudinal and transverse directions. The long-time dispersion coefficients of nanoparticles in longitudinal and transverse directions in both Newtonian and non-Newtonian solutions scale similarly, independent of the solution rheology. Although the mobility of nanoparticles becomes increasingly dependent on the local pore structure, the average mobility is still controlled by the overall random structure, which breaks the non-Newtonian characteristics of a polymer fluid on large time and length scales.

## 5.1 Materials and methods

### 5.1.1 Preparation of nanoparticles-solution dispersions

An aqueous solution of HPAM in deionized water with concentration of $c_{HPAM}$ = 0.135 wt % and a mixture of glycerol/water at a concentration of 90 wt% glycerol (G90) were prepared as described in Chapter 3. Polystyrene nanoparticles were added to HPAM solution, G90 solution, and deionized water at concentration of $2\times10^{-3}$ wt % and tumbled to thoroughly homogenize the solutions as described in Chapter 3.

### 5.1.2 Fabrication and characterization of porous media

Borosilicate glass microspheres with diameters of 5.4 ± 0.3 μm and 18.2 ± 1.0 μm were purchased from Thermo-Scientific. The glass particles were mixed at volume percent of 25%, 50%, and 75% of small beads. The square capillary was filled with bidisperse glass particles to fabricate a 3D porous medium with length of 5 mm. The glass particles were lightly sintered to ensure that beads were immobilized within the channel.

### 5.1.3 Characterization of pore and throat size of porous media

To visualize the bed structure, we suspended Rhodamine-B solution in a mixture of carbon disulfide (n=1.63) and ethanol (n=1.36). The amount of each mixture component is selected to match the refractive index of borosilicate (n=1.56) glass beads. Figure 5.1 shows confocal micrographs of beds with different volume percent of two glass beads. To

characterize the beds, we acquired two-dimensional images of beds using confocal microscopy. Table 5.1 shows the average porosity $\varphi$, average pore size $d_{pore}$, and average confinement length $l_c$ of the beds calculated from the chord length method described in Chapter 3.

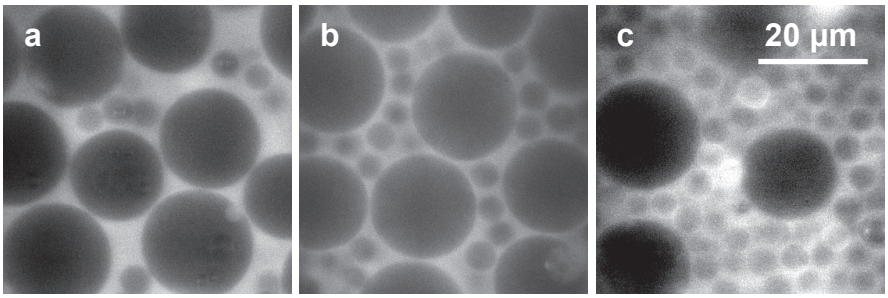


**Figure 5.1** Characterization of the porous media. Confocal images of bidisperse porous media with bead diameters of $d_{b1}$ = 5 µm and $d_{b1}$ = 20µm and volume fraction of (a) 25%, (b) 50%, and (c) 75% of small beads.

**Table 5.1** Average porosity, pore size (chord length), and confinement length (minimum chord length) of the bidisperse porous media with bead diameters of $d_{b,1}$ = 5 µm and $d_{b,2}$ = 20µm.

| Volume fraction of 5µm bead | Porosity | $l_c = \langle l_{chord} \rangle$ (µm) | $d_{pore} = \langle l_{chord,min} \rangle$ (µm) |
|---|---|---|---|
| 25% | 0.39 ± 0.05 | 9.0 ± 1.8 | 4.3 ± 0.9 |
| 50% | 0.40 ± 0.10 | 7.0 ± 2.8 | 3.2 ± 0.5 |
| 75% | 0.44 ± 0.05 | 6.5 ± 0.5 | 3.0 ± 0.3 |

### 5.1.4 Imaging of nanoparticles flowed through porous media

Nanoparticles were flowed through porous media using a syringe pump with constant displacement. Samples were imaged using a *VTeye* inverted confocal microscope (from VisiTech International) that was equipped with a 63× immersion oil lens of numerical aperture (NA) 1.40. We acquired 5000 frames at 102 frames per second

(fps) with a pixel size of 0.141 μm and an image size of 72.3 × 36.14 $\mu m^2$. We took multiple movies of each sample at ten different *x*-*y* locations, but constant *z* position, for each of four flow rates (Q= 5, 10, 15, and 20 μl/hr). The *x*-*y* locations were kept constant at different flow rates.

## 5.2 Results and discussions

To investigate the transport of nanoparticles in hydrolyzed polyacrylamide solution (0.135 w/w%) in heterogeneous porous media, we prepare bidisperse random packed beds by varying the volume fractions of glass particles with bead diameters of 5 and 20 μm. We fabricate three bidisperse beds with volume fraction of 25%, 50%, and 75% of 5 μm glass beads and at a near-constant average bed porosity of $\phi \approx 0.40$. The experimental setup is similar to that used for monodisperse beds, described in Chapter 4. We use a syringe pump with constant displacement to flow the nanoparticle dispersions through the bidisperse porous media. The inlet flow rate varies between Q = 5 – 20 μl/hr.

To quantify the micro-scale mobility of nanoparticles in different bidisperse porous beds, we first calculate the probability distributions of the nanoparticle velocities along and transverse to the flow direction using particle trajectories. Trajectories of nanoparticles at constant flow rate of Q = 5 μl/hr transported through bidisperse porous media with varying volume fraction of the small (5 μm) glass beads are show in Figure 5.2 (a—c). Normalized velocity distributions of nanoparticles at constant flow rate of Q = 5 μl/hr and different bidispersity ratio are shown for glycerol/water mixture (Figure 5.2 d and e) and in HPAM solution (Figure 5.2 f and g).

The normalized distributions of nanoparticle velocities in both the longitudinal and transverse directions are nearly independent of the bed particle composition (bidispersity), as shown in Figure 5.2(d,e,f,g). The normalized velocity distributions superimpose onto separate master curves for glycerol/water and for HPAM solutions through different bidisperse porous beds. The velocity distributions along the flow direction are asymmetric, exhibiting an exponentially stretched positive tail. By contrast, the transverse velocity distributions are symmetric and exponential; all normalized transverse velocity distributions are centered at zero, indicating that the particle mobility does not have any preferred direction perpendicular to the flow. Similar exponential distributions are observed for tracer velocities flowed through porous structures using numerical simulation[102] and confocal microscopy[229].

The exponential behavior of normalized velocity distributions in longitudinal and transverse directions is also independent of the bed bidispersity. The exponential tail seen in the longitudinal velocity distributions arising from a series of Gaussian processes with varying means and variances[38]. In turn, this behavior originates from a broad distribution of pore sizes. A single pore distribution of velocities approaches a Gaussian decay if the pore size is sufficiently small to be considered uniform. Since the structure of the pores is extremely disordered and heterogeneous in the bidisperse media, distribution of the pore size and velocities is non-Gaussian with an exponential asymmetric tail.

Figure 5.2 shows nanoparticle transport in bidisperse packed beds for Newtonian and for non-Newtonian solutions for inlet flow rate of 5 μl/hr: (a-c) trajectories of nanoparticles transported through bidisperse porous beds with bead diameters of 5 and 20

μm and small bead volume fraction of (a) 25%, (b) 50%, (c) 75%. Colors indicate the velocity along the flow direction ($v_x$): (d-g) normalized distributions of longitudinal $[G(v_x/v_{\text{avg}})]$ and transverse $[G(v_y/v_{\text{avg}})]$ velocities for nanoparticles transported in (d, e) a glycerol/water mixture (90 w/w%) and (f, g) an HPAM solution (0.135 w/w%) at inlet flow rate of 5 μl/hr through bidisperse porous beds with bead diameter of 5 and 20 μm and volume fraction of 25% (gold circle), 50% (blue triangle), 75% (red square) of small beads. The bi-dispersity ratio does not affect the normalized distributions of nanoparticle velocities for Newtonian or for non-Newtonian fluids.

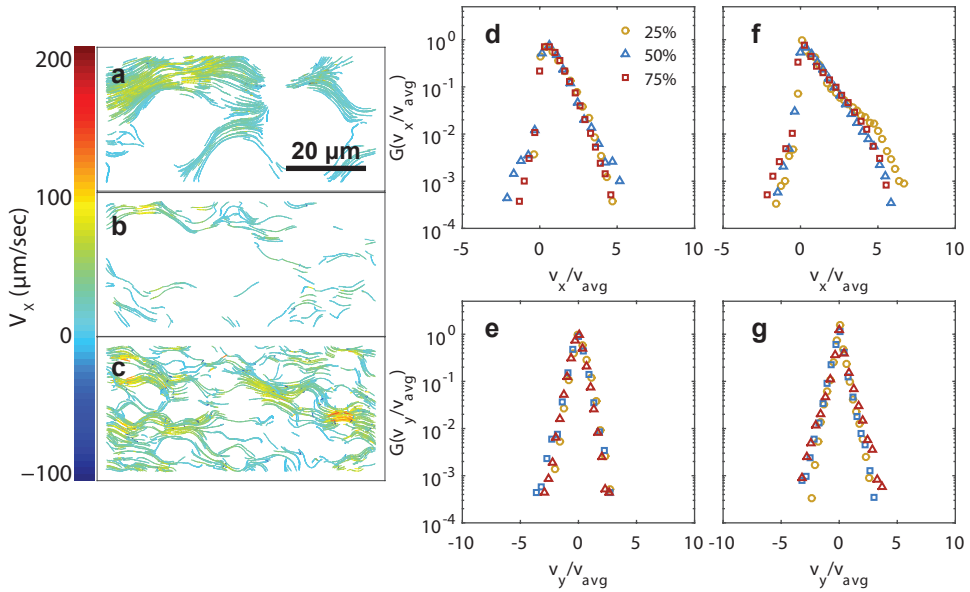


**Figure 5.2** Nanoparticle transport in bidisperse packed beds for Newtonian and for non-Newtonian solutions for inlet flow rate of 5 μl/hr transported through bidisperse porous beds with bead diameters of 5 and 20 μm.

Figure 5.3 shows nanoparticle transport in bidisperse packed beds for Newtonian and for non-Newtonian solutions for inlet flow rate of 15 μl/hr: (a-c) trajectories of

nanoparticles transported through bidisperse porous beds with bead diameters of 5 and 20 μm and small bead volume fraction of (a) 25%, (b) 50%, (c) 75%. Colors indicate the velocity along the flow direction ($v_x$): (d-g) normalized distributions of longitudinal $[G(v_x/v_{\text{avg}})]$ and transverse $[G(v_y/v_{\text{avg}})]$ velocities for nanoparticles transported in (d, e) a glycerol/water mixture (90 w/w%) and (f, g) an HPAM solution (0.135 w/w%) at inlet flow rate of 5 μl/hr through bidisperse porous beds with bead diameter of 5 and 20 μm and volume fraction of 25% (gold circle), 50% (blue triangle), 75% (red square) of small beads. The bi-dispersity ratio does not affect the normalized distributions of nanoparticle velocities for Newtonian or for non-Newtonian fluids.

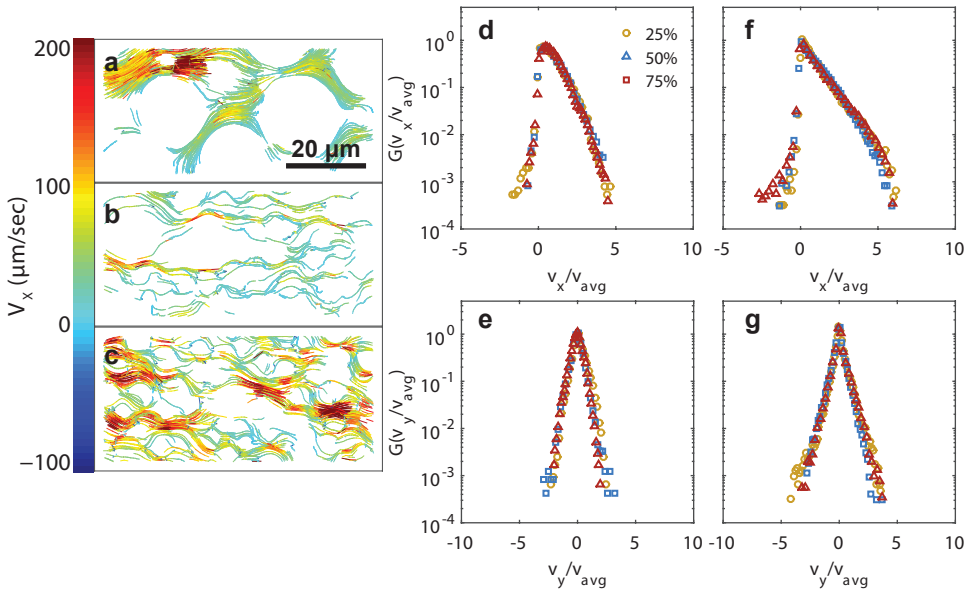


**Figure 5.3** Nanoparticle transport in bidisperse packed beds for Newtonian and for non-Newtonian solutions for inlet flow rate of 15 μl/hr transported through bidisperse porous beds with bead diameters of 5 and 20 μm.

We also quantify the role of flow rate on micro-scale transport dynamics of nanoparticles through porous media. To do so, we vary the flow rate between Q = 5—20 μl/hr. The velocity variation increases with increasing inlet flow rate, as shown in Figure 5.4—Figure 5.6 (a—d). The pore structure imposes tortuous paths for the nanoparticles, leading to a tortuosity that is greater than one. We calculate the probability distribution of nanoparticle velocities along and transverse to the flow direction. The distributions of normalized longitudinal and transverse velocities of nanoparticles in glycerol/water mixture and HPAM in different porous beds and for different inlet flow rates are shown in Figure 5.4—Figure 5.6 (e—h).

Figure 5.4 shows nanoparticle transport in bidisperse packed beds for Newtonian and for non-Newtonian solutions with bead diameters of 5 μm and 20 μm and small bead volume fraction of 25%: (a-d) trajectories of nanoparticles transported through a bidisperse porous bed at bulk flow rates of (a) 5, (b) 10, (c) 15, and (d) 20 μl/hr. Colors represent velocity variation along the flow direction ($v_x$): (e-h) normalized distributions of longitudinal [$G(v_x/v_{\mathrm{avg}})$] and transverse [$G(v_y/v_{\mathrm{avg}})$] velocities for nanoparticles in (e, f) a glycerol/water mixture (90 w/w%) and (g, h) an HPAM solution (0.135 w/w%) at an inlet flow rate of 5 (purple circle), 10 (blue square), 15 (red triangle), or 20 (gold diamond) μl/hr through the bidisperse bed. The inlet flow rate does not affect the normalized distributions of nanoparticle velocities for Newtonian or for non-Newtonian fluids.

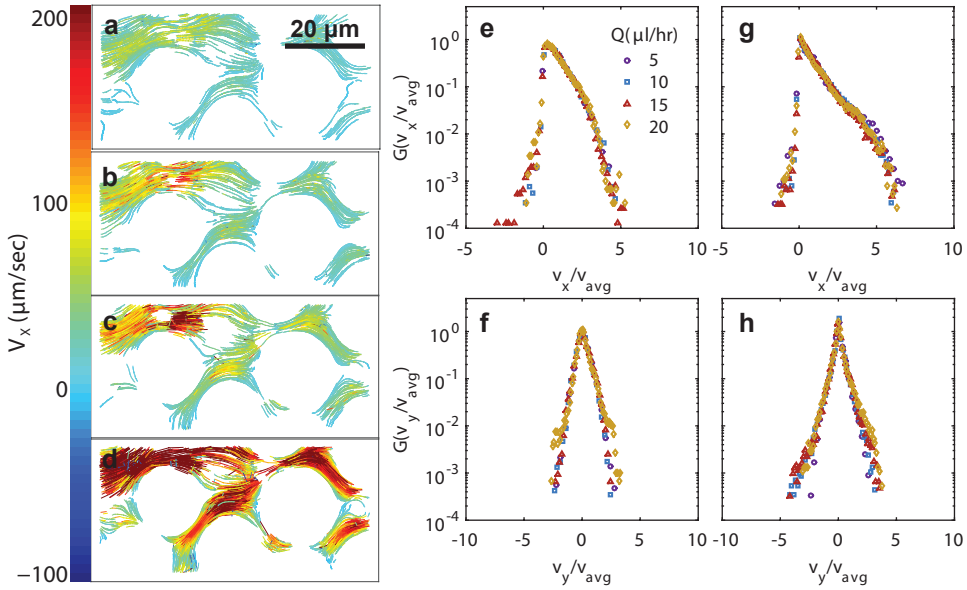


**Figure 5.4** Nanoparticle transport in bidisperse packed beds for Newtonian and for non-Newtonian solutions with bead diameters of 5 µm and 20 µm and small bead volume fraction of 25% transported through a bidisperse porous bed at bulk flow rates of 5 – 20 µl/hr.

Figure 5.5 shows nanoparticle transport in bidisperse packed beds for Newtonian and for non-Newtonian solutions with bead diameters of 5 µm and 20 µm and small bead volume fraction of 50%: (a-d) trajectories of nanoparticles transported through a bidisperse porous bed at bulk flow rates of (a) 5, (b) 10, (c) 15, and (d) 20 µl/hr. Colors represent velocity variation along the flow direction ($v_x$): (e-h) normalized distributions of longitudinal $[G(v_x/v_{\text{avg}})]$ and transverse $[G(v_y/v_{\text{avg}})]$ velocities for nanoparticles in (e, f) a glycerol/water mixture (90 w/w%) and (g, h) an HPAM solution (0.135 w/w%) at an inlet flow rate of 5 (purple circle), 10 (blue square), 15 (red triangle), or 20 (gold diamond) µl/hr through the bidisperse bed. The inlet flow rate does not affect the normalized distributions of nanoparticle velocities for Newtonian or for non-Newtonian fluids.

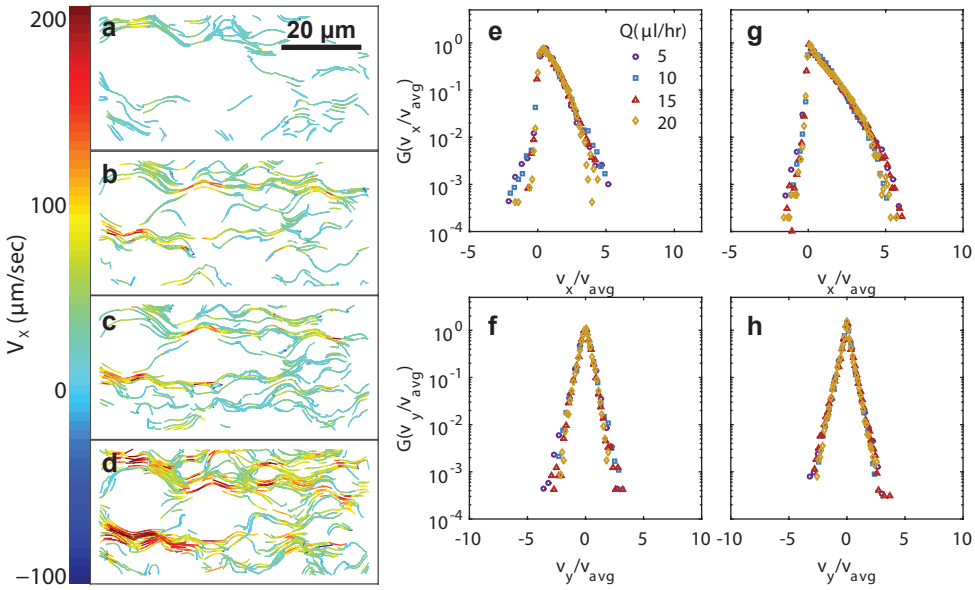


**Figure 5.5** Nanoparticle transport in bidisperse packed beds for Newtonian and for non-Newtonian solutions with bead diameters of 5 µm and 20 µm and small bead volume fraction of 50% transported through a bidisperse porous bed at bulk flow rates of 5 – 20 µl/hr.

Figure 5.6 represents nanoparticle transport in bidisperse packed beds for Newtonian and for non-Newtonian solutions with bead diameters of 5 µm and 20 µm and small bead volume fraction of 75%: (a-d) trajectories of nanoparticles transported through a bidisperse porous bed at bulk flow rates of (a) 5, (b) 10, (c) 15, and (d) 20 µl/hr. Colors represent velocity variation along the flow direction ($v_x$): (e-h) normalized distributions of longitudinal $[G(v_x/v_{\text{avg}})]$ and transverse $[G(v_y/v_{\text{avg}})]$ velocities for nanoparticles in (e, f) a glycerol/water mixture (90 w/w%) and (g, h) an HPAM solution (0.135 w/w%) at an inlet flow rate of 5 (purple circle), 10 (blue square), 15 (red triangle), or 20 (gold diamond) µl/hr through the bidisperse bed. The inlet flow rate does not affect the

normalized distributions of nanoparticle velocities for Newtonian or for non-Newtonian fluids.

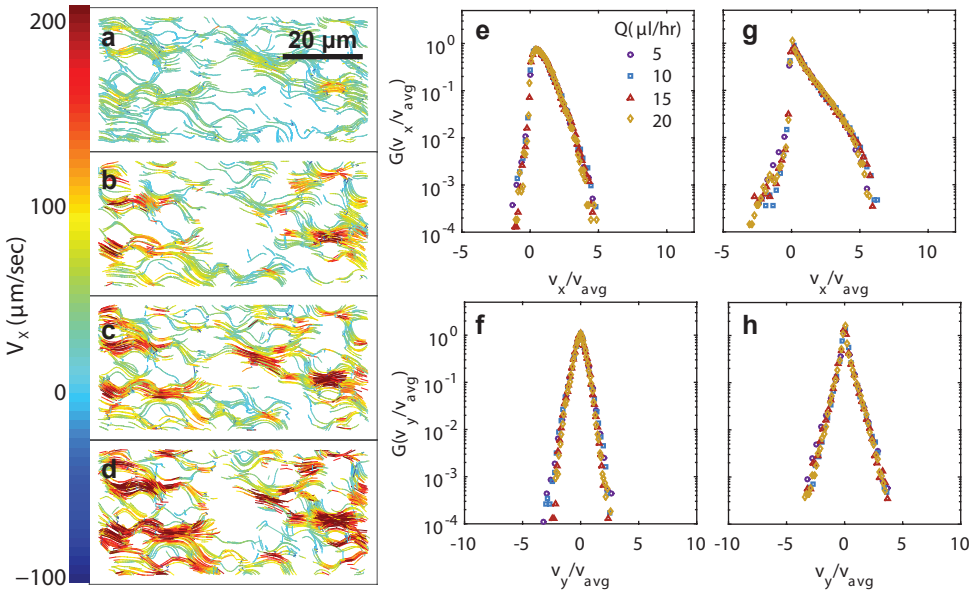


**Figure 5.6** Nanoparticle transport in bidisperse packed beds for Newtonian and for non-Newtonian solutions with bead diameters of 5 µm and 20 µm and small bead volume fraction of 75% transported through a bidisperse porous bed at bulk flow rates of 5 – 20 µl/hr.

The pore structure in the bidisperse beds is more heterogeneous than that of the monodisperse beds. Both the pore size and void accessibility depend the arrangement of glass beads as well as their volume fraction. Nonetheless, despite the heterogeneous pore structure the normalized velocity distributions behave similar to velocity distributions in monodisperse beds. The normalized velocity distributions at different flow rates collapse onto separate master curves for Newtonian and for non-Newtonian solutions. This behavior reveals pore-scale transport of nanoparticles is still linearly dependent on the average flow velocity in Newtonian and non-Newtonian solutions. Transport of nanoparticles in both solutions is mainly dominated by convection. We conclude that the

viscoelastic properties do not affect the long-time transport of nanoparticles through bidisperse porous beds.

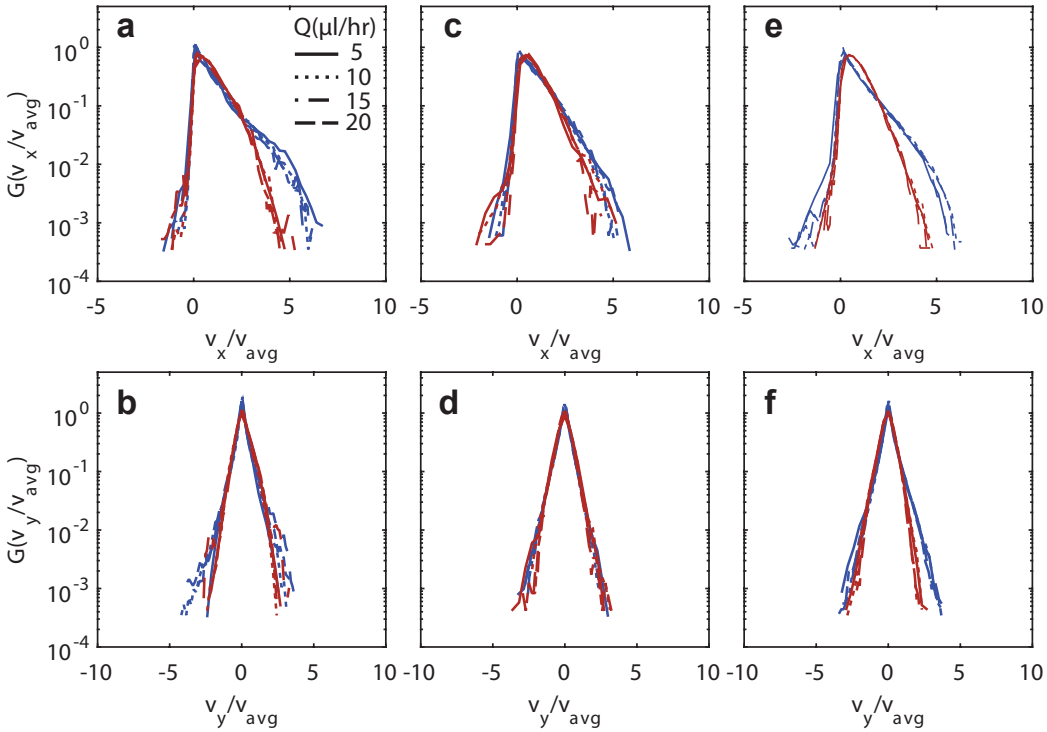


**Figure 5.7** Normalized longitudinal (top row) and transverse (bottom row) velocity distributions for nanoparticles flowed in glycerol/water mixture (red) and in HPAM solution (blue) at inlet flow rates of 5 μl/hr (line), 10 μl/hr (dotted line), 15 μl/hr (dashed-dotted line), and 20 μl/hr (dashed line) through bidisperse porous media with bead diameters of 5 μm and 20 μm and small bead volume fraction of (a,b) 25%, (c,d) 50%, and (e,f) 75%.

Although the normalized velocity distributions scale onto the master curves in Newtonian and non-Newtonian solutions separately, the superposition of distributions in both solutions shows deviation specifically at higher flow velocities corresponding to higher De (or Wi) number resulting from elastic instability.[113] The observed behavior is similar to what we showed in mono-dispersed media. The effect of bi-dispersity, which

also alters the average pore size and therefore the De number, however, is not distinguishable from the normalized distributions (Figure 5.7).

The analysis of velocity distributions reported in Figures X-Y highlights the transport of the nanoparticles at short time and length scales. To connect the short time- and length-scale velocities to the large length- and time-scale transport of particles through the packed beds, we calculate the time-dependent longitudinal and transverse dispersions using nanoparticles displacements as[89]

$$D_L(t) = \frac{1}{2}\frac{d{\sigma_L}^2}{dt} = \int C_L(t')dt',\ C_L(t) = \sum_{i=1}^{N}(v_{xi}(t) - \langle v_x \rangle)(v_{xi}(0) - \langle v_x \rangle), \qquad (5\text{-}1)$$

where $D_L(t)$ is the time-dependent longitudinal dispersion, ${\sigma_L}^2(t)$ is the second moment of longitudinal particle displacements, $C_L(t)$ is the auto-covariance of nanoparticle velocity, $v_{xi}(t)$ is the longitudinal particle velocity, and $\langle v_x \rangle$ is the average of longitudinal velocities. Transverse dispersion $D_T(t)$ is calculated similarly using the displacements of particles perpendicular to the flow direction. Simulations of the transport of small solutes in porous media indicate that dispersion coefficients approach asymptotic value if the time domain of correlation is smaller than the residence time in the porous media[89,230].

The longitudinal and transverse dispersion of nanoparticles through bidisperse beds increases with the normalized lag time $\tau = \frac{t v_{\mathrm{avg}}}{d_{\mathrm{be}}}$ and with the inlet flow rate in glycerol/water mixture (a and b) and HPAM (c and d), as shown in Figure 5.8—Figure 5.10 for different volume fractions of small beads. Here t is the lag time, $v_{\mathrm{avg}}$ is the average magnitude of the velocity; $d_{\mathrm{be}}$ is the effective bead diameter in bidisperse bed,

defined as $d_{\mathrm{be}} = \omega d_{b1} + (1-\omega) d_{b2}$, where $\omega$ is the volume (mass) fraction of small bead with bead diameter of $d_{b1} = 5$ µm and $d_{b2} = 20$ µm. The normalized longitudinal dispersion increases with normalized time in both Newtonian and non-Newtonian solutions due to advection and mixing effects until approaching an asymptotic maximum on long time scales. The normalized time corresponding to the maximum longitudinal dispersion is independent of flow velocity, but changes as the bidispersity ratio changes. This observation indicates that advection mainly controls longitudinal dispersion. The normalized transverse dispersion approaches a maximum at a normalized time of $\tau \approx 0.3 - 0.4$. Diffusion and mechanical mixing arising from advection mainly control transverse dispersion of nanoparticles through porous media[104]. The normalized time at which the asymptotic limit is reached, is nearly independent of average flow velocity and bidispersity ratio (Figure 5.8—Figure 5.10), which is in good agreement with that obtained for transport through monodisperse media (Chapter 4, $\tau \approx -0.4$).

Figure 5.8 shows time dependent dispersion of nanoparticles in Newtonian and non-Newtonian solutions: longitudinal ($D_L$, a and c) and transverse ($D_T$, b and d) dispersions of nanoparticles in (a, b) a glycerol/water mixture (90 w/w%) and (c, d) a HPAM solution (0.135 w/w%) as a function of normalized lag time ($\tau = t v_{avg}/d_{be}$) through a porous bidisperse bed with bead diameters of 5 µm and 20 µm and small bead volume fraction of 25%. Colors indicate different flow rates: 5 µl/hr (purple), 10 µl/hr (blue), and 15 µl/hr (red), and 20 µl/hr (gold). Open symbols indicate Newtonian fluids (glycerol/water mixture) and closed symbols indicate non-Newtonian solutions (HPAM).

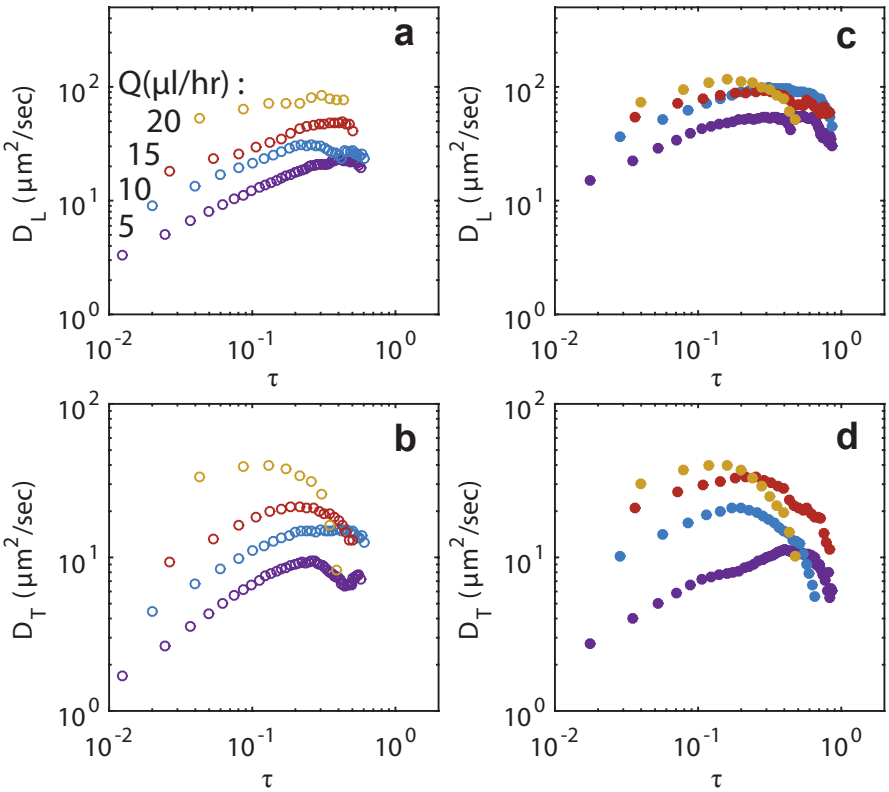


**Figure 5.8** Longitudinal (a and c) and transverse (b and d) dispersions of nanoparticles in (a, b) a glycerol/water and (c, d) a HPAM as a function of normalized lag time through a porous bidisperse bed with bead diameters of 5 and 20 µm and small bead volume fraction of 25%.

Figure 5.9 shows time dependent dispersion of nanoparticles in Newtonian and non-Newtonian solutions: longitudinal ($D_L$, a and c) and transverse ($D_T$, b and d) dispersions of nanoparticles in (a, b) a glycerol/water mixture (90 w/w%) and (c, d) a HPAM solution (0.135 w/w%) as a function of normalized lag time ($\tau = tv_{\text{avg}}/d_{\text{be}}$) through a porous bidisperse bed with bead diameters of 5 µm and 20 µm and small bead volume fraction of 50%. Colors indicate different flow rates: 5 µl/hr (purple), 10 µl/hr (blue), and 15 µl/hr (red), and 20 µl/hr (gold). Open symbols indicate Newtonian fluids (glycerol/water mixture) and closed symbols indicate non-Newtonian solutions (HPAM).

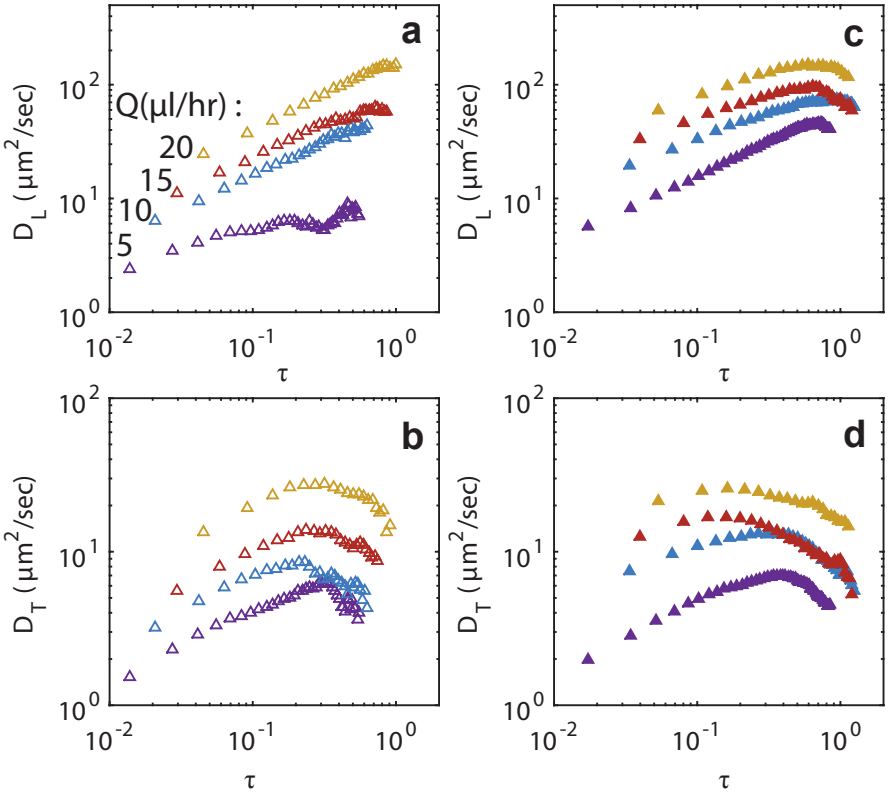


**Figure 5.9** Longitudinal (a and c) and transverse (b and d) dispersions of nanoparticles in (a, b) a glycerol/water and (c, d) a HPAM as a function of normalized lag time through a porous bidisperse bed with bead diameters of 5 and 20 µm and small bead volume fraction of 50%.

Figure 5.10 shows time dependent dispersion of nanoparticles in Newtonian and non-Newtonian solutions: longitudinal ($D_L$, a and c) and transverse ($D_T$, b and d) dispersions of nanoparticles in (a, b) a glycerol/water mixture (90 w/w%) and (c, d) a HPAM solution (0.135 w/w%) as a function of normalized lag time ($\tau = tv_{avg}/d_{be}$) through a porous bidisperse bed with bead diameters of 5 µm and 20 µm and small bead volume fraction of 75%. Colors indicate different flow rates: 5 µl/hr (purple), 10 µl/hr

(blue), and 15 µl/hr (red), and 20 µl/hr (gold). Open symbols indicate Newtonian fluids (glycerol/water mixture) and closed symbols indicate non-Newtonian solutions (HPAM).

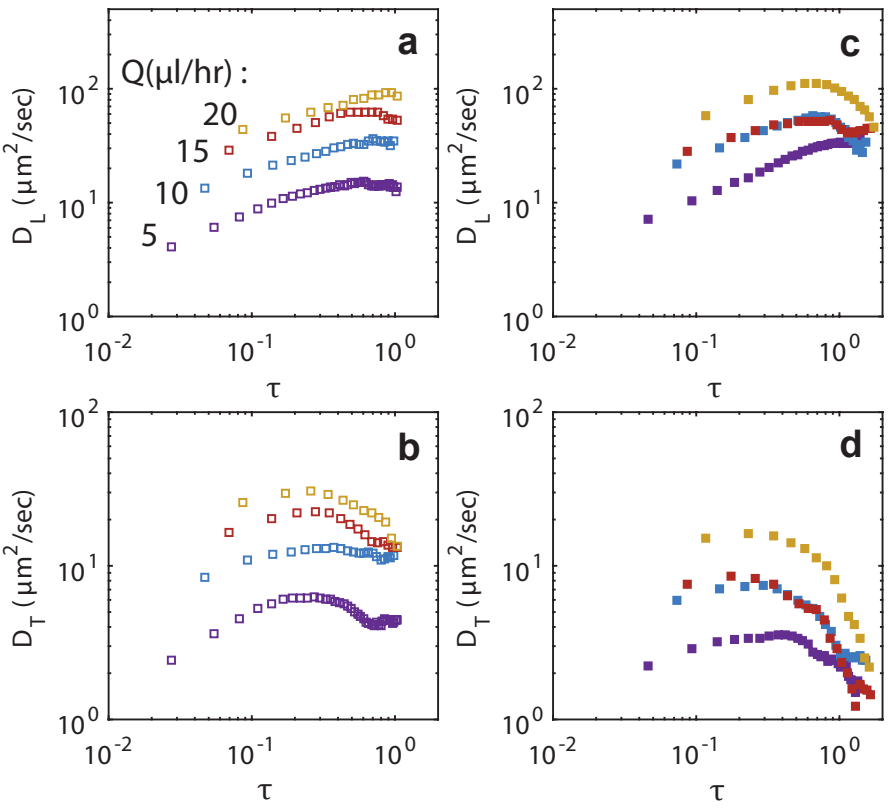


**Figure 5.10** Longitudinal (a and c) and transverse (b and d) dispersions of nanoparticles in (a, b) a glycerol/water and (c, d) a HPAM as a function of normalized lag time through a porous bidisperse bed with bead diameters of 5 and 20 µm and small bead volume fraction of 75%.

## 5.3 Conclusion

We quantify mobility of nanoparticles through bidisperse porous media in Newtonian and non-Newtonian solutions. The normalized distributions of nanoparticle velocity along and transverse to the flow direction are non-Gaussian and exponential, respectively, in both Newtonian and non-Newtonian solutions. The normalized velocity distributions collapse onto separate master curves for glycerol/water and for HPAM through porous media with varying bidispersity and flow rates. Moreover, the long time mobility of nanoparticles in non-Newtonian solution does not exhibit enhanced dispersion even at high velocities. These results indicate that the extent of pore structure heterogeneity does not strongly affect the long time mobility of particles through disordered porous media.

# Chapter 6

# 6.0 Conclusions and Future Research

## 6.1 Summary

This dissertation explores mobility of nanoparticles in complex and disordered media. The objective of this work is to understand dependence of diffusive and transport properties of nanoparticles in non-Newtonian and disordered media on the physical characteristics of media.

### 6.1.1 Diffusive mobility of nanoparticle in polymer solution is coupled to polymer dynamics

Diffusive mobility of polystyrene nanoparticle of diameter of 400 nm is measured as a function of the concentration of shear thinning hydrolyzed polyacrylamide (HPAM) solution of molecular weight of 8,000,000 Da. Diffusive mobility exhibits subdiffusive behavior at short time scales for polymer concentrations greater than the overlap concentration. At longer time scales, dynamics are Fickian diffusive at all concentrations. The crossover time scale between diffusive and subdiffusive dynamics increases with increasing polymer concentration and is intermediate between the relaxation times for polymer blobs and for self-diffusion. Moreover, the asymptotic long-time diffusivity of nanoparticles in HPAM solution is faster than zero-shear-rate self-diffusivity of polymer molecules itself. Our experiments reveal that particle dynamics are coupled to the

dynamics of the polymers on short time scales. At the length scale comparable to particle size, polymer-particle dynamics decouple. Dynamics grow linearly with time with effective diffusivity arising from segmental diffusion of polymer chains as well as the shear-thinning nature of the polymer solution.

### 6.1.2 Diffusive mobility of nanoparticle in porous media is hindered by hydrodynamic interactions and surface adsorption

The role of confinement mediated by macromolecules and by geometric obstacles on diffusive mobility of nanoparticles within porous media is investigated via measurements of the diffusion of nanoparticles in Newtonian (glycerol/water) and non-Newtonian (HPAM) solutions through porous media. Our observation reveals that diffusive mobility of nanoparticles decreases in both Newtonian and non-Newtonian solutions as nanoparticles are increasingly hindered by spatial confinement. Hydrodynamic interactions of nanoparticles with geometric obstacles reduce diffusive motion of nanoparticles in Newtonian and non-Newtonian solutions within porous media. Diffusive mobility depends on the relative length scale of particles to confinement length as well as diffusion time scale. As the particles encounter the surfaces of the glass beads that compose the bed, the dynamics become subdiffusive and the distributions of particle displacements become non-Gaussian. The results also highlight the stronger role of heterogeneities of disordered structures on dynamics of particles compared to that of ordered structures with comparable pore size[43]. The distribution of immobile times in Newtonian solution exhibits an exponential decay consistent with Poisson process.[231] By

contrast, in non-Newtonian solutions the distribution of immobile times exhibits a power-law decay, consistent with a higher probability of long dwell times near the surface. This observation suggests that an additional mechanism influences on diffusive mobility of particles in non-Newtonian solutions, arising from temporary adsorption of particles onto the surface of glass beads. Hence the presence of the long-chain polymer molecules alters the pore scale mobility of the particles. Mobility of nanoparticles in HPAM solution through porous media is controlled both by hydrodynamic interactions with the confining medium and by a polymer-mediated adsorption-desorption process arising from depletion interactions.

### 6.1.3 Nanoparticle dispersion in disordered porous media is insensitive to non-Newtonian fluid characteristics

The transport of nanoparticles suspended in Newtonian and non-Newtonian solutions through packed beds is studied to understand the effect of flow properties, non-Newtonian fluid characteristics, and geometric confinement on micro- and macro-scale dispersion of particles through porous media. The distributions of normalized longitudinal and transverse velocities collapse onto separate scaling curves at different flow rates and pore sizes in Newtonian (glycerol/water) and non-Newtonian (HPAM) solutions. Although the short time mobility of particles varies with the solution viscoelasticity, the long-time dispersion coefficients of nanoparticles in longitudinal and transverse direction scale linearly with Pe number, independent of the fluid rheology. This observation is in sharp contrast to the enhanced dispersion of particles in structured

media, where elastic turbulences enhance velocity fluctuations.[227] In structured media the fluctuations are not averaged out by the geometry of the medium, resulting in enhanced dispersion in transverse direction.[217] In disordered porous media, by contrast, random mixing effectively averages out the velocity fluctuation and ensures that the non-Newtonian characteristics do not affect long-time asymptotic dispersion. This feature suggests an intriguing connection between random mixing provided by disordered porous media and suppressing the non-Newtonian characteristics of the fluid even at high Pe numbers.

### 6.1.4 Nanoparticle dispersion in bidisperse porous media is independent of fluid characteristics

Dispersion of nanoparticles through bidisperse porous media in Newtonian and non-Newtonian solutions is quantified to investigate the role of bidispersity on transport of particles. Distributions of normalized velocity of particles are non-Gaussian and exponential in longitudinal and transverse directions. In both glycerol/water and HPAM, normalized longitudinal and transverse velocity distributions are independent of bidispersity and flow rates. Furthermore, long time dispersion of nanoparticles does not show any correlation to polymer elasticity. Mobility of particles through disordered porous media is therefore not affected significantly by the extent of pore heterogeneity. By relating the microscopic mobility to macroscopic transport, our approach enables the design of optimal systems in drug delivery, hydrocarbon productions, and polymer nanocomposite processing.

## 6.2 Future Research

Overall, the research in this dissertation can be extended in the following directions:

i. We studied diffusive mobility of nanoparticles at several concentrations of HPAM solution. However, at all concentrations, the polymer chains were unentangled. This study can be extended to mobility of nanoparticles in higher molecular weights and concentration of HPAM solution. The role of entanglements can be investigated on short and long time diffusive dynamics of particles with the size comparable to polymer mesh size.

ii. The polystyrene nanoparticles contained subtle amount of surfactant, which were considered neutral. Using charged nanoparticles in HPAM solution with ionic properties can be tested to investigate the effect of electrostatic and depletion interactions on diffusive mobility of nanoparticles.

iii. Diffusive mobility of nanoparticles at concentrations above the overlap concentration exhibits sub-diffusive dynamics even at the shortest accessible time scale of the experiments. Smaller nanoparticles (1-10 nm) and high resolution techniques can be used to study mobility of particles at time scales much smaller than the relaxation time of the polymer blobs. The integration of current results and such experiments will complete the physical picture and help to improve the current theoretical models.

iv. We used spherical nanoparticles to study diffusive mobility of nanoparticles in complex media, which did not have any preferred orientational diffusion

within the bulk solution. Diffusive dynamics of nanoparticles with different geometries, such as nanosheets (graphene oxide nanosheets) or nanorods (gold nanorods) can be examined within complex media to investigate the effect of asymmetry. Also, we used HPAM solution with flexible polymer chains as the non-Newtonian media. The research can be extended to diffusion of nanoparticles within polymer solutions with semi-flexible and rigid chains to understand effect of polymer flexibility on orientational diffusion.

v. The result of our model system can be used to design the *in-vivo* experiments in biological environments for drug delivery application. Using functionalized nanoparticles, which are applied in cancer treatment, diffusive mobility can be studied in cellular media. These experiments can be used to extract characteristic length scales and sizes present in biological materials.

vi. We also used a random packing of glass spheres as a model system to investigate dispersion of nanoparticles in confined media. Porous structure can be modified using nanofabrication techniques to be closer to natural porous media. Moreover, the average porosity was nearly constant in the porous media with different pore sizes and bi-dispersity ratio. The effect of porosity at fixed characteristic pore size can be investigated on diffusion and transport of nanoparticle through porous media.

vii. Glass microspheres can be treated to have hydrophilic/hydrophobic groups on the surface. The role of surface chemistry of porous structure on diffusive and transport dynamics of nanoparticles can be studied.

viii. We studied transport of nanoparticles through porous media at constant polymer concentration above the overlap concentration. Viscoelastic characteristics of HPAM solution highly depend on polymer concentration and molecular weights. Effects of higher concentrations and molecular weight of HPAM solution is suggested to be explored on dispersion of nanoparticles through porous media.

ix. Retention of polymer molecules on the surface of glass particle can change the local porosity of the bed over long time. Moreover flow might induce irreversible formation of nanogels through porous media[116]. Effect of polymer retention and gelation over time on porosity of the bed and therefore micro-scale velocity of nanoparticles through porous media is recommended to be studied.

x. We were not able to directly observe dynamics of polymer molecules within disordered media. Future studies can focus on diffusive and transport of fluorescently labeled polymer chains through such media. Effect of chemistry and roughness of the porous structure as well as flexibility and functional groups of polymer chains can be investigated on dynamics of polymer molecules.

## References


1. Jain, R. K. Delivery of Molecular Medicine to Solid Tumors: Lessons from in Vivo Imaging of Gene Expression and Function. *J. Control. Release* **2001**, *74*, 7–25.

2. Greish, K. Enhanced Permeability and Retention of Macromolecular Drugs in Solid Tumors: A Royal Gate for Targeted Anticancer Nanomedicines. *J. Drug Target.* **2007**, *15*, 457–464.

3. Baban, D. F.; Seymour, L. W. Control of Tumour Vascular Permeability. *Adv. Drug Deliv. Rev.* **1998**, *34*, 109–119.

4. Maeda, H.; Wu, J.; Sawa, T.; Matsumura, Y.; Hori, K. Tumor Vascular Permeability and the EPR Effect in Macromolecular Therapeutics: A Review. *J. Control. Release* **2000**, *65*, 271–284.

5. Cho, K.; Wang, X.; Nie, S.; Chen, Z.; Shin, D. M. Therapeutic Nanoparticles for Drug Delivery in Cancer. *Clin. Cancer Res.* **2008**, *14*, 1310–1316.

6. Jones, T.; Saba, N. Nanotechnology and Drug Delivery: An Update in Oncology. *Pharmaceutics* **2011**, *3*, 171–185.

7. Kanwar, J. R.; Kanwar, R. K.; Mahidhara, G.; Cheung, C. H. A. Cancer Targeted Nanoparticles Specifically Induce Apoptosis in Cancer Cells and Spare Normal Cells. *Aust. J. Chem.* **2012**, *65*, 5–14.

8. Park, J. H.; Lee, S.; Kim, J. H.; Park, K.; Kim, K.; Kwon, I. C. Polymeric

Nanomedicine for Cancer Therapy. *Prog. Polym. Sci.* **2008**, *33*, 113–137.

9. Moghimi, S. M. Nanomedicine: Current Status and Future Prospects. *FASEB J.* **2005**, *19*, 311–330.

10. Ryoo, S.; Rahmani, A. R.; Yoon, K. Y.; Prodanović, M.; Kotsmar, C.; Milner, T. E.; Johnston, K. P.; Bryant, S. L.; Huh, C. Theoretical and Experimental Investigation of the Motion of Multiphase Fluids Containing Paramagnetic Nanoparticles in Porous Media. *J. Pet. Sci. Eng.* **2012**, *81*, 129–144.

11. Dicarlo, D. A.; Aminzadeh, B.; Roberts, M.; Chung, D. H.; Bryant, S. L.; Huh, C. Mobility Control through Spontaneous Formation of Nanoparticle Stabilized Emulsions. *Geophys. Res. Lett.* **2011**, *38*, 1–5.

12. Nazari Moghaddam, R.; Bahramian, A.; Fakhroueian, Z.; Karimi, A.; Arya, S. Comparative Study of Using Nanoparticles for Enhanced Oil Recovery: Wettability Alteration of Carbonate Rocks. *Energy & Fuels* **2015**, *29*, 2111–2119.

13. Ehtesabi, H.; Ahadian, M. M.; Taghikhani, V. Enhanced Heavy Oil Recovery Using TiO 2 Nanoparticles : Investigation of Deposition during Transport in Core Plug. *Energy & Fuels* **2015**, *29*, 1–8.

14. Goel, G.; Krekelberg, W. P.; Errington, J. R.; Truskett, T. M. Tuning Density Profiles and Mobility of Inhomogeneous Fluids. *Phys. Rev. Lett.* **2008**, *100*, 106001.

15. Yu, H.; He, Y.; Li, P.; Li, S.; Zhang, T.; Rodriguez-pin, E.; Du, S. Flow

Enhancement of Water-Based Nanoparticle Dispersion through Microscale Sedimentary Rocks. *Sci. Rep.* **2015**, *5*, 1–8.

16. Yu, H.; Yoon, K. Y.; Neilson, B. M.; Bagaria, H. G.; Worthen, A. J.; Lee, J. H.; Cheng, V.; Bielawski, C. W.; Johnston, K. P.; Bryant, S. L.; *et al.* Transport and Retention of Aqueous Dispersions of Superparamagnetic Nanoparticles in Sandstone. *J. Pet. Sci. Eng.* **2014**, *116*, 15–123.

17. Tiraferri, A.; Sethi, R. Enhanced Transport of Zerovalent Iron Nanoparticles in Saturated Porous Media by Guar Gum. *J. Nanoparticle Res.* **2009**, *11*, 635–645.

18. Tiraferri, A.; Chen, K. L.; Sethi, R.; Elimelech, M. Reduced Aggregation and Sedimentation of Zero-Valent Iron Nanoparticles in the Presence of Guar Gum. *J. Colloid Interface Sci.* **2008**, *324*, 71–79.

19. Dalla Vecchia, E.; Luna, M.; Sethi, R. Transport in Porous Media of Highly Concentrated Iron Micro- and Nanoparticles in the Presence of Xanthan Gum. *Environ. Sci. Technol.* **2009**, *43*, 8942–8947.

20. Tosco, T.; Petrangeli Papini, M.; Cruz Viggi, C.; Sethi, R. Nanoscale Zerovalent Iron Particles for Groundwater Remediation: A Review. *J. Clean. Prod.* **2014**, *77*, 10–21.

21. Kanel, S. R.; Goswami, R. R.; Clement, T. P.; Barnett, M. O.; Zhao, D. Two Dimensional Transport Characteristics of Surface Stabilized Zero-Valent Iron Nanoparticles in Porous Media. *Environ. Sci. Technol.* **2008**, *42*, 896–900.

22. Johnson, R. L.; O'brien Johnson, G.; Nurmi, J. T.; Tratnyek, P. G. Natural Organic Matter Enhanced Mobility of Nano Zero- Valent Iron. *Environ. Sci. Technol.* **2009**, *43*, 5455–5460.

23. Gam, S.; Meth, J. S.; Zane, S. G.; Chi, C.; Wood, B. A.; Winey, K. I.; Clarke, N.; Composto, R. J. Polymer Diffusion in a Polymer Nanocomposite: Effect of Nanoparticle Size and Polydispersity. *Soft Matter* **2012**, *8*, 6512.

24. Kim, D.; Srivastava, S.; Narayanan, S.; Archer, L. A. Polymer Nanocomposites: Polymer and Particle Dynamics. *Soft Matter* **2012**, *8*, 10813.

25. Kumar, S. K.; Krishnamoorti, R. Nanocomposites: Structure, Phase Behavior, and Properties. *Annu. Rev. Chem. Biomol. Eng.* **2010**, *1*, 37–58.

26. Mohammad, M.; Winey, K. I. Polymer Nanocomposites Containing Carbon Nanotubes. *Macromolecules* **2006**, *39*, 5194–5205.

27. Schadler, L. S.; Kumar, S. K.; Benicewicz, B. C.; Lewis, S. L.; Harton, S. E. Designed Interfaces in Polymer Nanocomposites: A Fundamental Viewpoint. *MRS Bull.* **2007**, *32*, 335–340.

28. Oberdisse, J. Aggregation of Colloidal Nanoparticles in Polymer Matrices. **2005**, 29–36.

29. Hänggi, P.; Marchesoni, F. Artificial Brownian Motors: Controlling Transport on the Nanoscale. *Rev. Mod. Phys.* **2009**, *81*, 387–442.

30. Kirstein, J.; Platschek, B.; Jung, C.; Brown, R.; Bein, T.; Bräuchle, C. Exploration

of Nanostructured Channel Systems with Single-Molecule Probes. *Nat. Mater.* **2007**, *6*, 303–310.

31. Burada, P. S.; Hänggi, P.; Marchesoni, F.; Schmid, G.; Talkner, P. Diffusion in Confined Geometries. *ChemPhysChem* **2009**, *10*, 45–54.

32. Babu, S.; Gimel, J. C.; Nicolai, T. Tracer Diffusion in Colloidal Gels. *J. Phys. Chem.* **2008**, *112*, 743–748.

33. Guan, J.; Wang, B.; Granick, S. Even Hard-Sphere Colloidal Suspensions Display Fickian Yet Non-Gaussian Diffusion. *ACS Nano* **2014**, 3331–3336.

34. Cai, L.; Panyukov, S.; Rubinstein, M. Mobility of Nonsticky Nanoparticles in Polymer Liquids. *Macromolecules* **2011**, *44*, 7853–7863.

35. Babaye Khorasani, F.; Poling-Skutvik, R.; Krishnamoorti, R.; Conrad, J. C. Mobility of Nanoparticles in Semidilute Polyelectrolyte Solutions. *Macromolecules* **2014**, *47*, 5328–5333.

36. Cai, L. H.; Panyukov, S.; Rubinstein, M. Hopping Diffusion of Nanoparticles in Polymer Matrices. *Macromolecules* **2015**, *48*, 847–862.

37. Barkai, E.; Klafter, J. Subdiffusion and Anomalous Local Viscoelasticity in Actin Networks". *Phys. Rev. Lett.* **1998**, *81*, 1134–1134.

38. Wang, B.; Anthony, S. M.; Bae, S. C.; Granick, S. Anomalous yet Brownian. *Proc. Natl. Acad. Sci. U. S. A.* **2009**, *106*, 15160–15164.

39. Wang, B.; Kuo, J.; Bae, S. C.; Granick, S. When Brownian Diffusion Is Not Gaussian. *Nat. Mater.* **2012**, *11*, 481–485.

40. Fakhri, N.; MacKintosh, F. C.; Lounis, B.; Cognet, L.; Pasquali, M. Brownian Motion of Stiff Filaments in a Crowded Environment. *Science* **2010**, *330*, 1804–1808.

41. Raccis, R.; Nikoubashman, A.; Retsch, M.; Jonas, U.; Koynov, K.; Likos, C. N.; Fytas, G. Confined Diffusion in Periodic Porous Nanostructures. *ACS Nano* **2011**, *5*, 4607–4616.

42. Ghosh, P. K.; Hänggi, P.; Marchesoni, F.; Martens, S.; Nori, F.; Schimansky-Geier, L.; Schmid, G. Driven Brownian Transport through Arrays of Symmetric Obstacles. *Phys. Rev. E* **2012**, *85*, 011101.

43. He, K.; Babaye Khorasani, F.; Retterer, S. T.; Thomas, D. K.; Conrad, J. C.; Krishnamoorti, R. Diffusive Dynamics of Nanoparticles in Arrays of Nanoposts. *ACS Nano* **2013**, *7*, 5122–5130.

44. Aarão Reis, F. D. A.; Di Caprio, D. Crossover from Anomalous to Normal Diffusion in Porous Media. *Phys. Rev. E* **2014**, *89*, 062126.

45. Skaug, M. J.; Wang, L.; Ding, Y.; Schwartz, D. K. Hindered Nanoparticle Diffusion and Void Accessibility in a Three- Dimensional Porous Medium. *ACS Nano* **2015**, *9*, 2148–2156.

46. Skaug, M. J.; Schwartz, D. K. Tracking Nanoparticle Diffusion in Porous

Filtration Media. *Ind. Eng. Chem. Res.* **2015**, 150112152237002.

47. Yu, C.; Guan, J.; Chen, K.; Bae, S. C.; Granick, S. Single-Molecule Observation of Long Jumps in Polymer Adsorption. *ACS Nano* **2013**, *7*, 9735–9742.

48. Skaug, M. J.; Mabry, J.; Schwartz, D. K. Intermittent Molecular Hopping at the Solid-Liquid Interface. *Phys. Rev. Lett.* **2013**, *110*, 256101.

49. Wang, D.; He, C.; Stoykovich, M. P.; Schwartz, D. K. Nanoscale Topography Influences Polymer Surface Diffusion. *ACS Nano* **2015**, 1656–1664.

50. Kusumi, A.; Sako, Y.; Yamamoto, M. Confined Lateral Diffusion of Membrane Receptors as Studied by Single Particle Tracking (nanovid Microscopy). Effects of Calcium-Induced Differentiation in Cultured Epithelial Cells. *Biophys. J.* **1993**, *65*, 2021–2040.

51. Lubelski, A.; Sokolov, I.; Klafter, J. Nonergodicity Mimics Inhomogeneity in Single Particle Tracking. *Phys. Rev. Lett.* **2008**, *100*, 250602.

52. Magdziarz, M.; Weron, A. Anomalous Diffusion: Testing Ergodicity Breaking in Experimental Data. *Phys. Rev. E* **2011**, *84*, 051138.

53. Condamin, S.; Tejedor, V.; Voituriez, R.; Bénichou, O.; Klafter, J. Probing Microscopic Origins of Confined Subdiffusion by First-Passage Observables. *Proc. Natl. Acad. Sci. U. S. A.* **2008**, *105*, 5675–5680.

54. He, Y.; Burov, S.; Metzler, R.; Barkai, E. Random Time-Scale Invariant Diffusion and Transport Coefficients. *Phys. Rev. Lett.* **2008**, *101*, 058101.

55. Yuste, S.; Lindenberg, K. Subdiffusive Target Problem: Survival Probability. *Phys. Rev. E* **2007**, *76*, 051114.

56. Guo, H.; Bourret, G.; Corbierre, M.; Rucareanu, S.; Lennox, R.; Laaziri, K.; Piche, L.; Sutton, M.; Harden, J.; Leheny, R. Nanoparticle Motion within Glassy Polymer Melts. *Phys. Rev. Lett.* **2009**, *102*, 075702.

57. Dieterich, P.; Klages, R.; Preuss, R.; Schwab, A. Anomalous Dynamics of Cell Migration. *Proc. Natl. Acad. Sci. U. S. A.* **2008**, *105*, 459–463.

58. Banks, D. S. Anomalous Diffusion of Proteins Due to Molecular Crowding. **2005**, *89*, 2960–2971.

59. Golding, I.; Cox, E. Physical Nature of Bacterial Cytoplasm. *Phys. Rev. Lett.* **2006**, *96*, 098102.

60. Cukier, R. I. Diffusion of Brownian Spheres in Semidilute Polymer Solutions. *Macromolecules* **1984**, *17*, 252–255.

61. Brochard Wyart, F.; de Gennes, P. G. Viscosity at Small Scales in Polymer Melts. *Eur. Phys. J. E* **2000**, *1*, 93–97.

62. Odijk, T. Depletion Theory of Protein Transport in Semi-Dilute Polymer Solutions. *Biophys. J.* **2000**, *79*, 2314–2321.

63. De Gennes, P. G. Hydrodynamic Dispersion in Unsaturated Porous Media. *J. Fluid Mech.* **2006**, *136*, 189.

64. Tuinier, R.; Fan, T.-H. Scaling of Nanoparticle Retardation in Semi-Dilute Polymer Solutions. *Soft Matter* **2008**, *4*, 254.

65. Egorov, S. A. Anomalous Nanoparticle Diffusion in Polymer Solutions and Melts : A Mode-Coupling Theory Study. **2011**, *084903*, 1–7.

66. Langevin, D.; Rondelez, F. Sedimentation of Large Colloidal Particles through Semidilute Polymer Solutions. **1978**, *19*, 875–882.

67. Lin, T. H.; Phillies, G. D. J. Translational Diffusion Coefficient of a Macropartlculate Probe Species in Salt-Free Poly(acrylic Acid)-Water. *J. Phys. Chem.* **1982**, *86*, 4073–4077.

68. Cheng, Y.; Prud'homme, R. K.; Thomas, J. L. Diffusion of Mesoscopic Probes in Aqueous Polymer Solutions Measured by Fluorescence Recovery after Photobleaching. *Macromolecules* **2002**, *35*, 8111–8121.

69. Omari, R. A.; Aneese, A. M.; Grabowski, C. A.; Mukhopadhyay, A. Diffusion of Nanoparticles in Semidilute and Entangled Polymer Solutions. **2009**, 8449–8452.

70. Michelman-Ribeiro, A.; Horkay, F.; Nossal, R.; Boukari, H. Probe Diffusion in Aqueous Poly(vinyl Alcohol) Solutions Studied by Fluorescence Correlation Spectroscopy. *Biomacromolecules* **2007**, *8*, 1595–1600.

71. Phillies, G. D. J.; Clomenil, D. Probe Diffusion in Polymer Solutions under 0 and Good Conditions. *Macromolecules* **1993**, *26*, 167–170.

72. Kohli, I.; Mukhopadhyay, A. Diffusion of Nanoparticles in Semidilute Polymer

Solutions: Effect of Different Length Scales. **2012**.

73. Krüger, M.; Rauscher, M. Diffusion of a Sphere in a Dilute Solution of Polymer Coils. *J. Chem. Phys.* **2009**, *131*, 094902.

74. Phillies, G. D. J.; Richardson, C.; Quinlan, C. A. Transport in Intermediate and High Molecular Weight Hydroxypropylcellulose/Water Solutions. *Macromolecules* **1993**, *26*, 6849–6858.

75. Kasper, A.; Bartsch, E.; Sillescu, H. Self-Diffusion in Concentrated Colloid Suspensions Studied by Digital Video Microscopy of Core-Shell Tracer Particles. **1998**, *7463*, 5004–5010.

76. Weeks, E. R. Three-Dimensional Direct Imaging of Structural Relaxation Near the Colloidal Glass Transition. *Science* **2000**, *287*, 627–631.

77. Kegel, W. K.; van Blaaderen, A. Direct Observation of Dynamical Heterogeneities in Colloidal Hard-Sphere Suspensions. *Science* **2000**, *287*.

78. Weeks, E. R.; Weitz, D. . Subdiffusion and the Cage Effect Studied near the Colloidal Glass Transition. *Chem. Phys.* **2002**, *284*, 361–367.

79. Saltzman, E.; Schweizer, K. Non-Gaussian Effects, Space-Time Decoupling, and Mobility Bifurcation in Glassy Hard-Sphere Fluids and Suspensions. *Phys. Rev. E* **2006**, *74*, 061501.

80. Stariolo, D. A.; Fabricius, G. Fickian Crossover and Length Scales from Two Point Functions in Supercooled Liquids. *J. Chem. Phys.* **2006**, *125*, 64505.

81. Chaudhuri, P.; Berthier, L.; Kob, W. Universal Nature of Particle Displacements close to Glass and Jamming Transitions. *Phys. Rev. Lett.* **2007**, *99*, 060604.

82. Saltzman, E. J.; Schweizer, K. S. Large-Amplitude Jumps and Non-Gaussian Dynamics in Highly Concentrated Hard Sphere Fluids. *Phys. Rev. E* **2008**, *77*, 051504.

83. Van Hove, L. Correlations in Space and Time and Born Approximation Scattering in Systems of Interacting Particles. *Phys. Rev.* **1954**, *95*, 249–262.

84. Bénichou, O.; Chevalier, C.; Klafter, J.; Meyer, B.; Voituriez, R. Geometry-Controlled Kinetics. *Nat. Chem.* **2010**, *2*, 472–477.

85. Li, R.; Fowler, J. A.; Todd, B. A. Calculated Rates of Diffusion-Limited Reactions in a Three-Dimensional Network of Connected Compartments: Application to Porous Catalysts and Biological Systems. *Phys. Rev. Lett.* **2014**, *113*, 028303.

86. Collins, R. E.; Wilke, C. R. *Flow of Fluids through Porous Materials*; Reinhold: New York, 1961.

87. Bejan, A. *Convection Heat Transfer*; Wiley: New York, 1984.

88. Maier, R. S.; Kroll, D. M.; Kutsovsky, Y. E.; Davis, H. T.; Bernard, R. S. Simulation of Flow through Bead Packs Using the Lattice Boltzmann Method. *Phys. Fluids* **1998**, *10*, 60.

89. Maier, R. S.; Kroll, D. M.; Bernard, R. S.; Howington, S. E.; Peters, J. F.; Davis, H. T. Pore Scale Simulation of Dispersion.pdf. *Phys. Fluids* **2000**, *12*, 2068.

90. Bijeljic, B.; Muggeridge, A. H.; Blunt, M. J. Pore-Scale Modeling of Longitudinal Dispersion. *Water Resour. Res.* **2004**, *40*, 1–9.

91. Araújo, A. D.; Bastos, W. B.; Andrade, J. S.; Herrmann, H. J. Distribution of Local Fluxes in Diluted Porous Media. *Phys. Rev. E* **2006**, *74*, 010401.

92. Le Borgne, T.; Dentz, M.; Carrera, J. Lagrangian Statistical Model for Transport in Highly Heterogeneous Velocity Fields. *Phys. Rev. Lett.* **2008**, *101*, 090601.

93. Duda, A.; Koza, Z.; Matyka, M. Hydraulic Tortuosity in Arbitrary Porous Media Flow. *Phys. Rev. E* **2011**, *84*, 036319.

94. Yazdchi, K.; Srivastava, S.; Luding, S. Microstructural Effects on the Permeability of Periodic Fibrous Porous Media. *Int. J. Multiph. Flow* **2011**, *37*, 956–966.

95. Hyman, J. D.; Smolarkiewicz, P. K.; Winter, C. L. Heterogeneities of Flow in Stochastically Generated Porous Media. *Phys. Rev. E* **2012**, *86*, 056701.

96. de Anna, P.; Le Borgne, T.; Dentz, M.; Tartakovsky, A. M.; Bolster, D.; Davy, P. Flow Intermittency, Dispersion, and Correlated Continuous Time Random Walks in Porous Media. *Phys. Rev. Lett.* **2013**, *110*, 184502.

97. Bijeljic, B.; Raeini, A.; Mostaghimi, P.; Blunt, M. Predictions of Non-Fickian Solute Transport in Different Classes of Porous Media Using Direct Simulation on Pore-Scale Images. *Phys. Rev. E* **2013**, *87*, 013011.

98. Blunt, M. J.; Bijeljic, B.; Dong, H.; Gharbi, O.; Iglauer, S.; Mostaghimi, P.; Paluszny, A.; Pentland, C. Pore-Scale Imaging and Modelling. *Adv. Water Resour.*

**2013**, *51*, 197–216.

99. Yang, J.; Crawshaw, J.; Boek, E. S. Quantitative Determination of Molecular Propagator Distributions for Solute Transport in Homogeneous and Heterogeneous Porous Media Using Lattice Boltzmann Simulations. *Water Resour. Res.* **2013**, *49*, 8531–8538.

100. Icardi, M.; Boccardo, G.; Marchisio, D. L.; Tosco, T.; Sethi, R. Pore-Scale Simulation of Fluid Flow and Solute Dispersion in Three-Dimensional Porous Media. *Phys. Rev. E* **2014**, *90*, 013032.

101. Kang, P. K.; de Anna, P.; Nunes, J. P.; Bijeljic, B.; Blunt, M. J.; Juanes, R. Pore-Scale Intermittent Velocity Structure Underpinning Anomalous Transport through 3-D Porous Media. *Geophys. Res. Lett.* **2014**, *41*, 6184–6190.

102. Siena, M.; Riva, M.; Hyman, J. D.; Winter, C. L.; Guadagnini, A. Relationship between Pore Size and Velocity Probability Distributions in Stochastically Generated Porous Media. *Phys. Rev. E* **2014**, *89*, 013018.

103. Scheven, U. M.; Verganelakis, D.; Harris, R.; Johns, M. L.; Gladden, L. F. Quantitative Nuclear Magnetic Resonance Measurements of Preasymptotic Dispersion in Flow through Porous Media. *Phys. Fluids* **2005**, *17*, 117107.

104. Scheven, U. M. Pore-Scale Mixing and Transverse Dispersivity of Randomly Packed Monodisperse Spheres. *Phys. Rev. Lett.* **2013**, *110*, 214504.

105. Scheven, U. M.; Khirevich, S.; Daneyko, A.; Tallarek, U. Longitudinal and

Transverse Dispersion in Flow through Random Packings of Spheres: A Quantitative Comparison of Experiments, Simulations, and Models. *Phys. Rev. E* **2014**, *89*, 053023.

106. Huang, A. Y. L.; Huang, M. Y. F.; Capart, H.; Chen, R. H. Optical Measurements of Pore Geometry and Fluid Velocity in a Bed of Irregularly Packed Spheres. *Exp. Fluids* **2008**, *45*, 309–321.

107. Hassan, Y. A.; Dominguez-Ontiveros, E. E. Flow Visualization in a Pebble Bed Reactor Experiment Using PIV and Refractive Index Matching Techniques. *Nucl. Eng. Des.* **2008**, *238*, 3080–3085.

108. Sen, D.; Nobes, D. S.; Mitra, S. K. Optical Measurement of Pore Scale Velocity Field inside Microporous Media. *Microfluid. Nanofluidics* **2012**, *12*, 189–200.

109. Datta, S. S.; Chiang, H.; Ramakrishnan, T. S.; Weitz, D. A. Spatial Fluctuations of Fluid Velocities in Flow through a Three-Dimensional Porous Medium. *Phys. Rev. Lett.* **2013**, *111*, 064501.

110. Sochi, T. Non-Newtonian Flow in Porous Media. *Polymer.* **2010**, *51*, 5007–5023.

111. Gillissen, J. Viscoelastic Flow Simulations through an Array of Cylinders. *Phys. Rev. E* **2013**, *87*, 023003.

112. Moss, G. R.; Rothstein, J. P. Flow of Wormlike Micelle Solutions Past a Confined Circular Cylinder. *J. Nonnewton. Fluid Mech.* **2010**, *165*, 1505–1515.

113. Yip, R.; James, D. F.; Currie, I. G. PIV Measurements of Slow Flow of a

Viscoelastic Fluid within a Porous Medium. *Exp. Fluids* **2011**, *51*, 801–809.

114. Galindo-Rosales, F. J.; Campo-Deaño, L.; Pinho, F. T.; van Bokhorst, E.; Hamersma, P. J.; Oliveira, M. S. N.; Alves, M. A. Microfluidic Systems for the Analysis of Viscoelastic Fluid Flow Phenomena in Porous Media. *Microfluid. Nanofluidics* **2011**, *12*, 485–498.

115. Kenney, S.; Poper, K.; Chapagain, G.; Christopher, G. F. Large Deborah Number Flows around Confined Microfluidic Cylinders. *Rheol. Acta* **2013**, *52*, 485–497.

116. Vasudevan, M.; Buse, E.; Lu, D.; Krishna, H.; Kalyanaraman, R.; Shen, A. Q.; Khomami, B.; Sureshkumar, R. Irreversible Nanogel Formation in Surfactant Solutions by Microporous Flow. *Nat. Mater.* **2010**, *9*, 436–441.

117. Campo-Deaño, L.; Galindo-Rosales, F. J.; Pinho, F. T.; Alves, M. A.; Oliveira, M. S. N. Nanogel Formation of Polymer Solutions Flowing through Porous Media. *Soft Matter* **2012**, *8*, 6445.

118. Bleyer, J.; Coussot, P. Breakage of Non-Newtonian Character in Flow through a Porous Medium: Evidence from Numerical Simulation. *Phys. Rev. E* **2014**, *89*, 063018.

119. Chevalier, T.; Rodts, S.; Chateau, X.; Chevalier, C.; Coussot, P. Breaking of Non-Newtonian Character in Flows through a Porous Medium. *Phys. Rev. E* **2014**, *89*, 023002.

120. He, K.; Retterer, S. T.; Srijanto, B. R.; Conrad, J. C.; Krishnamoorti, R. Transport

and Dispersion of Nanoparticles in Periodic Nanopost Arrays. *ACS Nano* **2014**, *8*, 4221–4227.

121. Crocker, J.; Crocker, J.; Grier, D. Methods of Digital Video Microscopy for Colloidal Studies. *J. Colloid Interface Sci.* **1996**, *179*, 298–310.

122. Sahimi, M. Flow Phenomena in Rocks - from Continuum Models to Fractals, Percolation, Cellular-Automata, and Simulated Annealing. *Rev. Mod. Phys.* **1993**, *65*, 1393–1534.

123. Ponnapati, R.; Karazincir, O.; Dao, E.; Ng, R.; Mohanty, K. K.; Krishnamoorti, R. Polymer-Functionalized Nanoparticles for Improving Waterflood Sweep Efficiency: Characterization and Transport Properties. *Ind. Eng. Chem. Res.* **2011**, *50*, 13030–13036.

124. Metin, C.; Bonnecaze, R. T.; Nguyen, Q. P. The Viscosity of Silica Nanoparticle Dispersions in Permeable Media. *SPE Int. Oilf. Nanotechnol. Conf.* **2012**, 327–332.

125. Njuguna, B. J.; Pielichowski, K.; Alcock, J. R. Epoxy-Based Fibre Reinforced Nanocomposites. **2007**, 835–847.

126. Toohey, K. S.; Sottos, N. R.; Lewis, J. A.; Moore, J. S.; White, S. R. Self-Healing Materials with Microvascular Networks. *Nat. Mater.* **2007**, *6*, 581–585.

127. Toohey, K. S.; Hansen, C. J.; Lewis, J. A.; White, S. R.; Sottos, N. R. Delivery of Two-Part Self-Healing Chemistry via Microvascular Networks. *Adv. Funct. Mater.*

**2009**, *19*, 1399–1405.

128. Hansen, C. J.; Wu, W.; Toohey, K. S.; Sottos, N. R.; White, S. R.; Lewis, J. A. Self-Healing Materials with Interpenetrating Microvascular Networks. *Adv. Mater.* **2009**, *21*, 4143–4147.

129. Kolmakov, G. V; Revanur, R.; Tangirala, R.; Emrick, T.; Russell, T. P.; Crosby, A. J.; Balazs, A. C. Using Nanoparticle-Filled Microcapsules for Site-Specific Healing of Damaged Substrates: Creating a "Repair-and-Go" System. *ACS Nano* **2010**, *4*, 1115–1123.

130. Kratz, K.; Narasimhan, A.; Tangirala, R.; Moon, S.; Revanur, R.; Kundu, S.; Kim, H. S.; Crosby, A. J.; Russell, T. P.; Emrick, T.; Kolmakov, G.; Balazs, A. C.; Probing and Repairing Damaged Surfaces with Nanoparticle-Containing Microcapsules. *Nat. Nanotechnol.* **2012**, *7*, 87–90.

131. Squires, T. M.; Mason, T. G. Fluid Mechanics of Microrheology. *Annu. Rev. Fluid Mech.* **2010**, *42*, 413–438.

132. Crocker, J. C.; Valentine, M. T.; Weeks, E. R.; Gisler, T.; Kaplan, P. D.; Yodh, A. G.; Weitz, D. A. Two-Point Microrheology of Inhomogeneous Soft Materials. *Phys. Rev. Lett.* **2000**, *85*, 888–891.

133. Dasgupta, B.; Tee, S.-Y.; Crocker, J.; Frisken, B.; Weitz, D. Microrheology of Polyethylene Oxide Using Diffusing Wave Spectroscopy and Single Scattering. *Phys. Rev. E* **2002**, *65*, 051505.

134. Lu, Q.; Solomon, M. J. Probe Size Effects on the Microrheology of Associating Polymer Solutions. *Phys. Rev. E* **2002**, *66*, 061504.

135. Chen, D. T.; Weeks, E. R.; Crocker, J. C.; Islam, M. F.; Verma, R.; Gruber, J.; Levine, A. J.; Lubensky, T. C.; Yodh, A. G. Rheological Microscopy: Local Mechanical Properties from Microrheology. *Phys. Rev. Lett.* **2003**, *90*, 108301.

136. Gardel, M. L.; Valentine, M. T.; Crocker, J. C.; Bausch, A. R.; Weitz, D. A. Microrheology of Entangled F-Actin Solutions. *Phys. Rev. Lett.* **2003**, *91*, 158302.

137. Dasgupta, B.; Weitz, D. Microrheology of Cross-Linked Polyacrylamide Networks. *Phys. Rev. E* **2005**, *71*, 021504.

138. Liu, J.; Gardel, M. L.; Kroy, K.; Frey, E.; Hoffman, B. D.; Crocker, J. C.; Bausch, A. R.; Weitz, D. A. Microrheology Probes Length Scale Dependent Rheology. *Phys. Rev. Lett.* **2006**, *96*, 118104.

139. Oppong, F. K.; Rubatat, L.; Frisken, B. J.; Bailey, A. E.; De Bruyn, J. R. Microrheology and Structure of a Yield-Stress Polymer Gel. *Phys. Rev. E - Stat. Nonlinear, Soft Matter Phys.* **2006**, *73*, 1–9.

140. Jan, J. S.; Breedveld, V. Microrheological Study of Polyelectrolyte Collapse and Reexpansion in the Presence of Multivalent Counterions. *Macromolecules* **2008**, *41*, 6517–6522.

141. Larsen, T. H.; Furst, E. M. Microrheology of the Liquid-Solid Transition during Gelation. *Phys. Rev. Lett.* **2008**, *100*, 146001.

142. Zhu, X.; Kundukad, B.; Van Der Maarel, J. R. C. Viscoelasticity of Entangled λ-Phage DNA Solutions. *J. Chem. Phys.* **2008**, *129*, 185103.

143. Dunstan, D. E.; Stokes, J. Diffusing Probe Measurements of Polystyrene Latex Particles in Polyelectrolyte Solutions : Deviations from Stokes - Einstein Behavior. *Macromolecules* **2000**, 33, 193–198.

144. Mackay, M. E.; Dao, T. T.; Tuteja, A.; Ho, D. L.; Horn, B. V. A. N.; Kim, H.; Hawker, C. J. Nanoscale Effects Leading to Non-Einstein-like Decrease in Viscosity. *Nat. Mater.* **2003**, *2*, 762–766.

145. Tuteja, A.; Mackay, M. E.; Narayanan, S.; Asokan, S.; Wong, M. S. Breakdown of the Continuum Stokes-Einstein Relation for Nanoparticle Diffusion. *Nano Lett.* **2007**, *7*, 1276–1281.

146. Guo, H.; Bourret, G.; Lennox, R. B.; Sutton, M.; Harden, J. L.; Leheny, R. L. Entanglement-Controlled Subdiffusion of Nanoparticles within Concentrated Polymer Solutions. *Phys. Rev. Lett.* **2012**, *109*, 055901.

147. Kohli, I.; Alam, S.; Patel, B.; Mukhopadhyay, A. Interaction and Diffusion of Gold Nanoparticles in Bovine Serum Albumin Solutions. *Appl. Phys. Lett.* **2013**, *102*, 203705.

148. Yamamoto, U.; Schweizer, K. S. Theory of Nanoparticle Diffusion in Unentangled and Entangled Polymer Melts. *J. Chem. Phys.* **2011**, *135*, 0–16.

149. Kalathi, J. T.; Yamamoto, U.; Schweizer, K. S.; Grest, G. S.; Kumar, S. K.

Nanoparticle Diffusion in Polymer Nanocomposites. *Phys. Rev. Lett.* **2014**, *112*, 108301.

150. Berry, H.; Chaté, H. Anomalous Diffusion due to Hindering by Mobile Obstacles Undergoing Brownian Motion or Orstein-Ulhenbeck Processes. *Phys. Rev. E* **2014**, *89*, 022708.

151. Lu, B.; Denton, A. R. Crowding of Polymer Coils and Demixing in Nanoparticle-Polymer Mixtures. *J. Phys. Condens. Matter* **2011**, *23*, 285102.

152. Dix, J. A.; Verkman, A. S. Crowding Effects on Diffusion in Solutions and Cells. *Annu. Rev. Biophys.* **2008**, *37*, 247–263.

153. Wong, I.; Gardel, M.; Reichman, D.; Weeks, E.; Valentine, M.; Bausch, A.; Weitz, D. Anomalous Diffusion Probes Microstructure Dynamics of Entangled F-Actin Networks. *Phys. Rev. Lett.* **2004**, *92*, 178101.

154. Banks, D. S.; Fradin, C. Anomalous Diffusion of Proteins due to Molecular Crowding. *Biophys. J.* **2005**, *89*, 2960–2971.

155. Szymanski, J.; Weiss, M. Elucidating the Origin of Anomalous Diffusion in Crowded Fluids. *Phys. Rev. Lett.* **2009**, *103*, 038102.

156. Yu, Y.; Anthony, S. M.; Bae, S. C.; Granick, S. How Liposomes Diffuse in Concentrated Liposome Suspensions. *J Phys Chem B* **2011**, *115*, 2748–2753.

157. Zustiak, S. P.; Nossal, R.; Sackett, D. L. Hindered Diffusion in Polymeric Solutions Studied by Fluorescence Correlation Spectroscopy. *Biophys. J.* **2011**,

*101*, 255–264.

158. Sokolov, I. M. Models of Anomalous Diffusion in Crowded Environments. *Soft Matter* **2012**, *8*, 9043.

159. Thiel, F.; Flegel, F.; Sokolov, I. M. Disentangling Sources of Anomalous Diffusion. *Phys. Rev. Lett.* **2013**, *111*, 010601.

160. Zhao, F.; Du, Y. K.; Liu, S. F.; Xu, J. K.; Tang, J. A. Characterization of the Conformational Changes of Partially Hydrolyzed Polyacrylamide Chains in Solution Using Stress Recovery Experiment. *J. Appl. Polym. Sci.* **2006**, *101*, 2709–2713.

161. Muller, G.; Laine, J. P.; Fenyo, J. C. High-Molecular-Weight Hydrolyzed Polyacrylamides. I. Characterization. Effect of Salts on the Conformational Properties. *J. Polym. Sci. Polym. Chem. Ed.* **1979**, *17*, 659–672.

162. Flory, P. J.; Fox, T. G. Treatment of Intrinsic Viscosities. *J. Am. Chem. Soc.* **1951**, *73*, 1904–1908.

163. Wolff, C. Molecular Weight Dependence of the Relative Viscosity of Solutions of Polymers at the Critical Concentration. *Eur. Polym. J.* **1977**, *13*, 739–741.

164. Dobrynin, A. V.; Colby, R. H.; Rubinstein, M. Scaling Theory of Polyelectrolyte Solutions. *Macromolecules* **1995**, *28*, 1859–1871.

165. Crocker, J.; Crocker, J.; Grier, D. Methods of Digital Video Microscopy for Colloidal Studies. *J. Colloid Interface Sci.* **1996**, *179*, 298–310.

166. Boris, D. C.; Colby, R. H. Rheology of Sulfonated Polystyrene Solutions. *Macromolecules* **1998**, *31*, 5746–5755.

167. Sprakel, J.; van der Gucht, J.; Cohen Stuart, M.; Besseling, N. Rouse Dynamics of Colloids Bound to Polymer Networks. *Phys. Rev. Lett.* **2007**, *99*, 208301.

168. Sprakel, J.; van Der Gucht, J.; Cohen Stuart, M. A.; Besseling, N. a M. Brownian Particles in Transient Polymer Networks. *Phys. Rev. E* **2008**, *77*, 061502.

169. Li, J.; Li, W.; Huo, H.; Luo, S.; Wu, C. Reexamination of the Slow Mode in Semidilute Polymer Solutions: The Effect of Solvent Quality. *Macromolecules* **2008**, *41*, 901–911.

170. Dieteren, C. E. J.; Gielen, S. C. A. M.; Nijtmans, L. G. J.; Smeitink, J. A. M.; Swarts, H. G.; Brock, R.; Willems, P. H. G. M.; Koopman, W. J. H. Solute Diffusion Is Hindered in the Mitochondrial Matrix. *Proc. Natl. Acad. Sci. U. S. A.* **2011**, *108*, 8657–8662.

171. Höfling, F.; Franosch, T. Anomalous Transport in the Crowded World of Biological Cells. *Reports Prog. Phys.* **2013**, *76*, 046602.

172. Tabei, S. M. A.; Burov, S.; Kim, H. Y.; Kuznetsov, A.; Huynh, T.; Jureller, J.; Philipson, L. H.; Dinner, A. R.; Scherer, N. F. Intracellular Transport of Insulin Granules Is a Subordinated Random Walk. *Proc. Natl. Acad. Sci. U. S. A.* **2013**, *110*, 4911–4916.

173. Eggeling, C.; Ringemann, C.; Medda, R.; Schwarzmann, G.; Sandhoff, K.;

Polyakova, S.; Belov, V. N.; Hein, B.; von Middendorff, C.; Schönle, A.; *et al.* Direct Observation of the Nanoscale Dynamics of Membrane Lipids in a Living Cell. *Nature* **2009**, *457*, 1159–1162.

174. Jin, G. Z.; Eltohamy, M.; Kim, H. W. Nanocomposite Scaffolds Incorporated with Hydrophobically-Functionalized Mesoporous Nanocarriers for the Effective Loading and Long-Term Delivery of Osteogenic Drugs. *RSC Adv.* **2015**, *5*, 26832–26842.

175. Hahn, K.; Kärger, J.; Kukla, V. Single-File Diffusion Observation. *Phys. Rev. Lett.* **1996**, *76*, 2762.

176. De Vos, D. E.; Dams, M.; Sels, B. F.; Jacobs, P. A. Ordered Mesoporous and Microporous Molecular Sieves Functionalized with Transition Metal Complexes as Catalysts for Selective Organic Transformations. *Chem. Rev.* **2002**, *102*, 3615–3640.

177. Corma, A.; Garcia, H. Supported Gold Nanoparticles as Catalysts for Organic Reactions. *Chem. Soc. Rev.* **2008**, *37*, 2096–2126.

178. Rebbin, V.; Schmidt, R.; Fröba, M. Spherical Particles of Phenylene-Bridged Periodic Mesoporous Organosilica for High-Performance Liquid Chromatography. *Angew. Chemie - Int. Ed.* **2006**, *45*, 5210–5214.

179. Novikov, D. S.; Fieremans, E.; Jensen, J. H.; Helpern, J. A. Random Walk with Barriers. *Nat. Phys.* **2011**, *7*, 508–514.

180. Won, J.; Onyenemezu, C.; Miller, W. G.; Lodge, T. P. Diffusion of Spheres in Entangled Polymer Solutions: A Return to Stokes-Einstein Behavior. *Macromolecules* **1994**, *27*, 7389–7396.

181. Choi, J.; Cargnello, M.; Murray, C. B.; Clarke, N.; Winey, K. I.; Composto, R. J. Fast Nanorod Diffusion through Entangled Polymer Melts. *ACS Macro Lett.* **2015**, 952–956.

182. Gong, Z.; Maarel, J. R. C. Van Der. Translational and Reorientational Dynamics of Entangled DNA. **2014**.

183. Stoeckel, D.; Kübel, C.; Hormann, K.; Höltzel, A.; Smarsly, B. M.; Tallarek, U. Morphological Analysis of Disordered Macroporous-Mesoporous Solids Based on Physical Reconstruction by Nanoscale Tomography. *Langmuir* **2014**, *30*, 9022–9027.

184. Poling-Skutvik, R.; Krishnamoorti, R.; Conrad, J. C. Size-Dependent Dynamics of Nanoparticles in Unentangled Polyelectrolyte Solutions. *ACS Macro Lett.* **2015**, *4*, 1169–1173.

185. Liasneuski, H.; Hlushkou, D.; Khirevich, S.; Höltzel, A.; Tallarek, U.; Torquato, S. Impact of Microstructure on the Effective Diffusivity in Random Packings of Hard Spheres. *J. Appl. Phys.* **2014**, *116*, 034904.

186. Torquato, S. Effective Electrical Conductivity of Two-phase Disordered Composite Media. *J. Appl. Phys.* **1985**, *7910*, 3790–3797.

187. Dechadilok, P.; Deen, W. M. Hindrance Factors for Diffusion and Convection in Pores. *Ind. Eng. Chem. Res.* **2006**, *45*, 6953–6959.

188. Kluijtmans, S. G. J. M.; Dhont, J. K. G.; Philipse, A. P. Dynamics of Uncharged Colloidal Silica Spheres Confined in Bicontinuous Porous Glass Media. *Langmuir* **1997**, *13*, 4982–4987.

189. Davidson, M.; Deen, W. Hindered Diffusion of Water-Soluble Macromolecules in Membranes. *Macromolecules* **1988**, 3474–3481.

190. Pawar, Y.; Anderson, J. L. Hindered Diffusion in Slit Pores: An Analytical Result. *Ind. Eng. Chem. Res.* **1993**, *32*, 743–746.

191. Happel, J.; Brenner., H. *Low Reynolds Number Hydrodynamics: With Special Applications to Particulate Media.*; Springer Science & Business Media, 2012.

192. Ganatos, P.; Pfeffer, R.; Weinbaum, S. A Strong Interaction Theory for the Creeping Motion of a Sphere between Plane Parallel Boundaries. Part 2. Parallel Motion. *J. Fluid Mech.* **1980**, *99*, 755–783.

193. Pappenheimer, J. R.; Renkin, E. M.; Borrero, L. M. Filtration, Diffusion and Molecular Sieving through Peripheral Capillary Membranes. *Am. J. Physiol* **1951**, *167*.

194. Renkin, E. M. Filtration, Diffusion, and Molecular Sieving through Porous Cellulose Membrane. *J. Gen. Physiol* **1954**.

195. Brenner, H.; Gaydos, L. J. The Constrained Brownian Movement of Spherical

Particles in Cylindrical Pores of Comparable Radius. *J. Colloid Interface Sci.* **1977**, *58*, 312–356.

196. Nitsche, J. M.; Balgi, G. Hindered Brownian Diffusion of Spherical Solutes within Circular Cylindrical Pores. *Ind. Eng. Chem. Res.* **1994**, *33*, 2242–2247.

197. Mavrovouniotis, G. M.; Brenner, H. Hindered Sedimentation, Diffusion, and Dispersion Coefficients for Brownian Spheres in Circular Cylindrical Pores. *J. Colloid Interface Sci.* **1988**, *124*, 269–283.

198. Higdon, J. J. L.; Muldowney, G. P. Resistance Functions for Spherical Particles, Droplets and Bubbles in Cylindrical Tubes. *J. Fluid Mech.* **1995**, *298*, 193–210.

199. Pawar, Y.; Anderson, J. L. Hindered Diffusion in Slit Pores: An Analytical Result. *Ind. Eng. Chem. Res.* **1993**, *32*, 743–746.

200. Bevan, M. A.; Prieve, D. C. Hindered Diffusion of Colloidal Particles Very near to a Wall: Revisited. *J. Chem. Phys.* **2000**, *113*, 1228.

201. Imperio, A.; Padding, J. T.; Briels, W. J. Diffusion of Spherical Particles in Microcavities. *J. Chem. Phys.* **2011**, *134*, 1–9.

202. Eichmann, S. L.; Smith, B.; Meric, G.; Fairbrother, D. H.; Bevan, M. A. Imaging Carbon Nanotube Interactions , Diffusion , and Stability in Nanopores. *ACS Nano* **2011**, *5*, 5909–5919.

203. Van Oss, C. .; Good, R. .; Chaudhury, M. . The Role of van Der Waals Forces and Hydrogen Bonds in “hydrophobic Interactions” between Biopolymers and Low

Energy Surfaces. *J. Colloid Interface Sci.* **1986**, *111*, 378–390.

204. Wang, H.; Sodagari, M.; Chen, Y.; He, X.; Newby, B. Z.; Ju, L.-K. Initial Bacterial Attachment in Slow Flowing Systems: Effects of Cell and Substrate Surface Properties. *Colloids Surfaces B Biointerfaces* **2011**, *87*, 415–422.

205. Rudhardt, D.; Bechinger, C.; Leiderer, P. Direct Measurement of Depletion Potentials in Mixtures of Colloids and Nonionic Polymers. *Phys. Rev. Lett.* **1998**, *81*, 1330–1333.

206. Kleshchanok, D.; Tuinier, R.; Lang, P. R. Direct Measurements of Polymer-Induced Forces. **2008**, *20*.

207. Tuinier, R.; Aarts, D. G. A. L.; Wensink, H. H.; Lekkerkerker, H. N. W. Pair Interaction and Phase Separation in Mixtures of Colloids and Excluded Volume Polymers. *Phys. Chem. Chem. Phys.* **2003**, *5*, 3707.

208. Skaug, M. J.; Mabry, J. N.; Schwartz, D. K. Single-Molecule Tracking of Polymer Surface Diffusion. *J. Am. Chem. Soc.* **2014**, *136*, 1327–1332.

209. Tang, R.; Kim, C. S.; Solfiell, D. J.; Rana, S.; Mout, R.; Velázquez-Delgado, E. M.; Chompoosor, A.; Jeong, Y.; Yan, B.; Zhu, Z.-J.; *et al.* Direct Delivery of Functional Proteins and Enzymes to the Cytosol Using Nanoparticle-Stabilized Nanocapsules. *ACS Nano* **2013**, *7*, 6667–6673.

210. Kharchenko, S. B.; Douglas, J. F.; Obrzut, J.; Grulke, E. A.; Migler, K. B. Flow-Induced Properties of Nanotube-Filled Polymer Materials. *Nat. Mater.* **2004**, *3*,

564–568.

211. Chandran, S.; Begam, N.; Padmanabhan, V.; Basu, J. K. Confinement Enhances Dispersion in Nanoparticle-Polymer Blend Films. *Nat. Commun.* **2014**, *5*, 3697.

212. Koch, D. L.; Brady, J. F. Dispersion in Fixed Beds. *J. Fluid Mech.* **1985**, *145*.

213. Moss, G. R.; Rothstein, J. P. Flow of Wormlike Micelle Solutions Past a Confined Circular Cylinder. *J. Nonnewton. Fluid Mech.* **2010**, *165*, 1505–1515.

214. Vasudevan, M.; Buse, E.; Lu, D.; Krishna, H.; Kalyanaraman, R.; Shen, A. Q.; Khomami, B.; Sureshkumar, R. Irreversible Nanogel Formation in Surfactant Solutions by Microporous Flow. *Nat. Mater.* **2010**, *9*, 436–441.

215. Burghelea, T.; Segre, E.; Bar-Joseph, I.; Groisman, A.; Steinberg, V. Chaotic Flow and Efficient Mixing in a Microchannel with a Polymer Solution. *Phys. Rev. E* **2004**, *69*, 066305.

216. Groisman, A.; Enzelberger, M.; Quake, S. R. Microfluidic Memory and Control Devices. *Science* **2003**, *300*, 955–958.

217. Scholz, C.; Wirner, F.; Gomez-Solano, J. R.; Bechinger, C. Enhanced Dispersion by Elastic Turbulence in Porous Media. *EPL* **2014**, *107*, 54003.

218. Scheven, U. M.; Harris, R.; Johns, M. L. Intrinsic Dispersivity of Randomly Packed Monodisperse Spheres. *Phys. Rev. Lett.* **2007**, *99*, 054502.

219. Frechette, J.; Drazer, G. Directional Locking and Deterministic Separation in

Periodic Arrays. *J. Fluid Mech.* **2009**, *627*, 379–401.

220. Huang, L. R.; Cox, E. C.; Austin, R. H.; Sturm, J. C. Continuous Particle Separation through Deterministic Lateral Displacement. *Science* **2004**, *304*, 987–990.

221. Pandey, R.; Conrad, J. C. Effects of Attraction Strength on Microchannel Flow of Colloid–polymer Depletion Mixtures. *Soft Matter* **2012**, *8*, 10695.

222. Pakdel, P.; McKinley, G. Elastic Instability and Curved Streamlines. *Phys. Rev. Lett.* **1996**, *77*, 2459–2462.

223. Kemblowski, Z.; Michniewicz, M. A New Look at the Laminar Flow of Power Law Fluids through Granular Beds. *Rheol. Acta* **1979**, *18*, 730–739.

224. Bijeljic, B.; Mostaghimi, P.; Blunt, M. J. Signature of Non-Fickian Solute Transport in Complex Heterogeneous Porous Media. *Phys. Rev. Lett.* **2011**, *107*, 204502.

225. Kandhai, D.; Hlushkou, D.; Hoekstra, A. G.; Sloot, P. M. A.; Van As, H.; Tallarek, U. Influence of Stagnant Zones on Transient and Asymptotic Dispersion in Macroscopically Homogeneous Porous Media - Art. No. 234501. *Phys. Rev. Lett.* **2002**, *88*, 234501.

226. Bijeljic, B.; Blunt, M. J. Pore-Scale Modeling of Transverse Dispersion in Porous Media. *Water Resour. Res.* **2007**, *43*, 1–8.

227. Bodiguel, H.; Beaumont, J.; Machado, A.; Martinie, L.; Kellay, H.; Colin, A. Flow

Enhancement due to Elastic Turbulence in Channel Flows of Shear Thinning Fluids. *Phys. Rev. Lett.* **2015**, *114*, 028302.

228. Medina, R.; Elkhoury, J. E.; Morris, J. P.; Prioul, R.; Desroches, J.; Detwiler, R. L. Flow of Concentrated Suspensions through Fractures: Small Variations in Solid Concentration Cause Significant in-Plane Velocity Variations. *Geofluids* **2015**, *15*, 24–36.

229. Datta, S. S.; Chiang, H.; Ramakrishnan, T. S.; Weitz, D. A. Spatial Fluctuations of Fluid Velocities in Flow through a Three-Dimensional Porous Medium. *Phys. Rev. Lett.* **2013**, *111*, 064501.

230. Maier, R. S.; Kroll, D. M.; Bernard, R. S.; Howington, S. E.; Peters, J. F.; Davis, H. T. Hydrodynamic Dispersion in Confined Packed Beds. *Phys. Fluids* **2003**, *15*, 3795–3815.

231. Sánchez, R.; Newman, D. E.; Carreras, B. A. Waiting-Time Statistics of Self-Organized-Criticality Systems. *Phys. Rev. Lett.* **2002**, *88*, 068302.

232. Dobrynin, A. V.; Colby, R. H.; Rubinstein, M. Scaling Theory of Polyelectrolyte Solutions *Macromolecules* **1995**, 28, 1859-1871.